SYNTHESIS OF NICOMNX (X = IN, AL) HEUSLER-TYPE MAGNETIC SHAPE MEMORY ALLOY THIN FILMS

A Dissertation

by

STEVEN ELI RIOS

Submitted to the Office of Graduate and Professional Studies of
Texas A&M University
in partial fulfillment of the requirements for the degree of

DOCTOR OF PHILOSOPHY

Chair of Committee,	Xinghang Zhang
Committee Members,	Raymundo Arroyave
	Ibrahim Karaman
	Haiyan Wang
Head of Department,	Ibrahim Karaman

August 2014

Major Subject: Materials Science and Engineering

ABSTRACT

Magnetic shape memory alloys are a class of shape memory alloys, and therefore exhibit a thermoelastic martensite phase transformation between symmetric and asymmetric crystalline states induced by appropriate temperature and/or stress changes. Shape memory alloys are able to recover strain when stress is applied, which can generate higher actuation forces and displacements compared to piezoelectrics and magnetostrictive materials when the material is constrained. While shape memory alloys have found applications in biomedical and aerospace industries, actuator applications are limited to relatively low frequencies compared to piezoelectric materials. The slow response of shape memory alloys is associated with heating or cooling the material from an external source. Compared to traditional shape memory alloys, the coupling of structural and magnetic ordering result in magnetic and structural transformations that increase the functional properties in magnetic shape memory alloys, such as magnetic field-induced rapid martensite transformation (forward and reversed), giant magnetoresistance, and the magnetocaloric effect.

While bulk MSMAs can be used for structural components, in many cases MSMA thin films are preferred for device applications, such as miniaturized actuators, small scale propulsion devices, and micro-electro-mechanical systems (MEMS). This thesis focuses on the synthesis of NiCoMnX (X=In, Al) Heusler-type magnetic shape memory alloy thin films via physical vapor deposition, and details the challenges associated with controlling film composition, precipitation, microstructure, residual stress, and mechanical properties.

As-deposited films were found to contain a mixture of amorphous and nanocrystalline microstructure, and thus, did not exhibit a martensitic transformation. Appropriate post-deposition heat treatments were required to crystallize the films, tailor the grain size, and reduce the formation of precipitates. Crystallized films exhibited martensitic transformations that showed a grain size dependence. An analytical model that uses a thermodynamic framework was developed to explain the suppression of the martensitic transformations for films with submicron-sized grains.

Hence, in addition to chemical composition, sub-micron grain size can be used to tailor the martensitic transformation temperature of NiCoMnX (X=In, Al) thin films for device applications. Additionally, the analytical model may reduce the uncertainty associated with a direct scale-up of thin film compositions used for combinatorial investigations of magnetic shape memory alloys.

DEDICATION

This dissertation is dedicated to:
The memory of my mother, Virginia,
my father, Eli,
my sister, Stephanie,
and to Megan,
for your enduring love and support.

ACKNOWLEDGEMENTS

First, I sincerely thank and extend my deepest gratitude to my committee chair, Dr. Zhang, for his support, guidance, and endless encouragement during my time at Texas A&M University in pursuit of becoming a better person, scientist, and engineer. I express sincere appreciation to my committee members, Dr. Arroyave, Dr. Karaman, and Dr. Wang for their guidance and support throughout the course of this research. Their doors were always open; when I needed help, their advice proved invaluable.

Thanks also go to the Mechanical Engineering department staff for making my time at Texas A&M University a great experience. Additional thanks goes to Jan Gerston, the Materials Science and Engineering (MSEN) graduate program director. She guided me through my graduate studies, and always goes beyond the call of duty to ensure all MSEN students enjoy their time at Texas A&M University while pursuing a graduate degree.

I want to thank Mark Hollander for teaching me the practical aspects of mechanical design for building new equipment, and the art of modifying existing equipment to perform experiments. I want to thank my collaborators from the Wang group, Dr. Chen Fong, Clement Jacob, and Wenrui Zhang for their direct support to this work. I also want to thank my friends and coworkers, David Foley, Shreyas Balachandran, Dr. Daniel Bufford, Dr. Kaiyuan Yu, Dr. Yue Liu, Dr. Michael Martin, Youxing Chen, Dr. Byoungsoo Ham, Dr. Cheng Sun, Dr. Engang Fu, Dr. Nan Li, and Dr. Osman Anderoglu for contributions during formal meetings and informal discussions in the hallway. I appreciate their support while taking classes together and working late evenings to build and repair laboratory equipment. Most of all, I am grateful for their friendship.

I also want to extend my gratitude to the National Science Foundation’s Division of Materials Research (NSF-DMR) grant program, whose support made this work possible.

Finally, thanks to my mother and father for their encouragement and to Megan for her patience and love.

NOMENCLATURE

A	Austenite phase
Al	Aluminum
H	Applied magnetic field
A_f	Austenite finish temperature
A_s	Austenite start temperature
Co	Cobalt
ΔS	Entropy difference between A and M phases
T_0	Equilibrium temperature
ΔQ	Heat of transformation
HTSMA	High temperature shape memory alloy
In	Indium
ΔM	Magnetization difference between A and M phases
MSMA	Magnetic shape memory alloy
Mn	Manganese
M	Martensite phase
M_f	Martensite finish temperature
M_s	Martensite start temperature

MT	Martensitic transformation
Ni	Nickel
SAD	Selected area diffraction
SMA	Shape memory alloy
T	Temperature
TEM	Transmission electron microscope
XRD	X-ray diffraction

TABLE OF CONTENTS

LIST OF FIGURES

Page

Page

Page

1. INTRODUCTION AND LITERATURE REVIEW

1.1 Motivation

This dissertation seeks to answer two questions. First, can we develop magnetic shape memory alloy (MSMAs) nanonostructures for actuation, sensing, and power generation? Such materials can reduce the number and size of components in micro-electro-mechanical systems (MEMS). Second, in parallel can we extrapolate the multifunctional properties of sub-micron systems from bulk MSMAs?

To answer these questions, this dissertation focuses on the synthesis of NiCoMnX (X=In, Al) Heusler-type magnetic shape memory alloy thin films via physical vapor deposition, and details the challenges associated with controlling film composition, precipitation, microstructure, residual stress, and mechanical properties. Understanding these issues is crucial for the application of NiCoMnX (X=In, Al) thin films for device applications.

1.2 Functional materials

Magnetic shape memory alloys are a class shape memory alloys, and shape memory alloys provide useful behaviors like the shape memory effect where a residual strain is recovered by heating, and pseudoelasticity where large strains are recovered from unloading [1]. These characteristic behaviors make SMAs useful for actuator applications.

An actuator converts energy into motion. Hydraulic, pneumatic, and electrical motors are examples of conventional actuators. The source of power for the first two motors use fluid or pneumatic pressure while the electric motor utilizes electric pressure (voltage) to convert energy into motion. Functional materials represent a class of actuator materials that possess one or more physical properties that vary in a controlled manner when an external stimulus is applied such as temperature, stress, magnetic or electric fields.

Actuator materials such as piezoceramics and magnetostrictive alloys have advantages for use as conventional actuators or transducers, since they operate at high frequencies [2, 3], but these materials can only produce small strains, normally on the order of 10^{-3}. Lead zirconate titanate, commonly called PZT, is a piezoceramic, that generates a strain of about 0.1% in an electric field of several hundred V/cm [4]. Meanwhile, the oxide is brittle. Magnetostrictive materials such as Terfenol-D thin films [5-10] give a strain of about 0.2% in a moderate magnetic field, but their constituents consisting of rare earth metals, Tb and Dy, are expensive.

There are numerous types of shape memory alloys (SMAs), including conventional SMAs, magnetic SMAs (MSMAs), or high temperature SMAs (HTSMAs). Conventional shape memory alloys (SMAs), such as NiTi operate at temperatures below 373 K, and consequently have been integrated into MEMS devices for biomedical applications such as micropumps used for drug delivery[11, 12].

Magnetic shape memory alloys (MSMAs) have become an interesting extension to the class of actuator materials [13-17]. Since the discovery of a large magnetic field induced strain (MFIS) in Ni_2MnGa [18], MSMAs are able to sustain large actuation strains up to 10% under a magnetic field [4, 19, 20]. MSMAs show all the characteristics of conventional SMAs, but additionally an alternating magnetic field can be used to induce large strains with rapid response times [21-23]. MSMAs may experience martensitic phase transformation under an applied magnetic field. If a large difference in saturation magnetization between austenite and martensite exists, the application of a magnetic field can effectively vary the martensitic phase transformation temperature. The advantage of such magnetic field induced phase transformation is to provide large actuation strain (comparable to conventional SMAs), and meanwhile enable high frequency phase transformations compared with slow response of conventional SMAs to temperature limited by a slow heat transfer mechanism [24].

There are two major mechanisms through which applied magnetic field can induce strain in MSMAs. The first method involves the field-induced reorientation of martensite twins. This mechanism typically operates when there is high magnetocrystalline anisotropy energy (MAE) and low energy of twin boundary motion. Since the MAE is limited by the saturation magnetization of the martensite phase, the output stress that can be obtained from an applied magnetic field is often limited to a few MPa. The second mechanism utilizes the difference between the saturation magnetizations of austenite and martensite phases as a driving force for phase transformation.

If a large difference in saturation magnetization between austenite and martensite exists, the application of a magnetic field can effectively vary the martensitic phase transformation temperature. Thus, the existence of a large Zeeman energy leads to substantial field-induced phase transformation (FIPT). The advantage of such magnetic field induced phase transformation is to provide large actuation strain (comparable to conventional SMAs), and enable high frequency phase transformations compared with the slow response of conventional SMAs, which are limited by a slow heat transfer mechanism [24]. A family of MSMAs called metamagnetic shape memory alloys based on NiCoMnX (X = Al, In, Sb, and Sn) exhibit FIPT [25-33]. In the NiCoMnIn system, thermomagnetization studies show that phase transformation temperature can decrease by as much as 30 K ($Ni_{45}Co_5Mn_{36.6}In_{13.4}$) while in a magnetic field up to 7 T [34]. Furthermore, near pseudo elasticity and 3% MFIS of field-induced strain were achieved in $Ni_{45}Co_5Mn_{36.5}In_{13.5}$ system under stress levels as high as 125 MPa [32]. MSMAs that recover from prestrain by FIPT are said to exhibit a metamagnetic shape memory effect. The metamagnetic shape memory effect has been reported for NiCoMnIn [28-31, 34-45], CoNiAl [46], NiCoMnSn [25, 47-51], NiCoMnAl [26, 31, 52-56], NiCoMnSb [57-60] alloys. Since FIPT does not depend on orientation and is proportional to the Zeeman energy, a larger work output is generated compared to work associated with martensite variant rearrangement [33]. Therefore, MSMAs that exhibit a metamagnetic shape memory effect are candidate materials for high performance multifunctional actuators. Moreover, MSMA thin films have potential use as MEMS sensors for active and passive damage detection.

HTSMAs can operate at temperatures above 373 K, and thus may enable applications at elevated temperature as reliable, compact actuators for automotive and aerospace applications [24, 61]. While conventional SMAs operate near room temperature, HTSMAs operate in a temperature regime where the martensitic transformation, a diffusionless process, may be influenced by diffusion based processes such as recrystallization, decomposition, and recovery [62]. In thin films, recrystallization leads to a change in residual stresses [63], and the formation of precipitates create chemical and stress gradients that affect the transformation behavior of SMA thin films [64, 65].

Figure 1.1 compares the magnetic work output levels for different active materials, such as piezoelectrics (polymers and ceramics), magnetostrictive, shape memory alloys and magnetic shape memory alloys. It is worth noting that NiCoMnIn alloys, represented by the black ellipse, fill the gap between conventional shape memory alloys and MSMAs that actuate using a field induced variant reorientation. Additionally, NiCoMnIn offers faster actuation frequency compared to shape memory alloys [33].

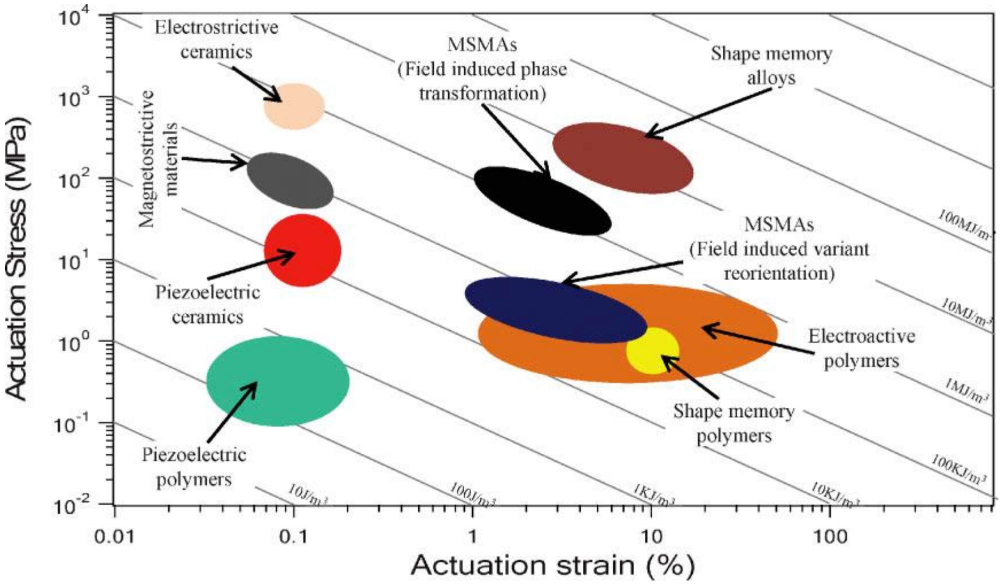

Figure 1.1 Comparison of actuation stress, actuation strain, and actuation work output levels for different active materials [33].

1.3 Thin film applications

As discussed earlier, the magnetic properties of MSMAs offer additional functionality compared to a conventional SMA, which only responds to thermal and stress fields. Therefore, thin film applications can be grouped into two classes related to the thermal hysteresis: (1) a small thermal hysteresis is required for actuators, and (2) a large thermal hysteresis is required for thermal indicators.

1.3.1 Small thermal hysteresis applications

Magnetic actuators require a small thermal hysteresis. In principle, MSMA actuators work by transforming from the martensite phase below M_f to the austenite phase above A_f by applying a magnetic field. Because the magnetostructural transition is a first-order transformation, the magnetic field must be large enough to transform martensite to a fully austenite state. Anything less will result in a partially reversible transition that reduces the efficiency of the actuator.

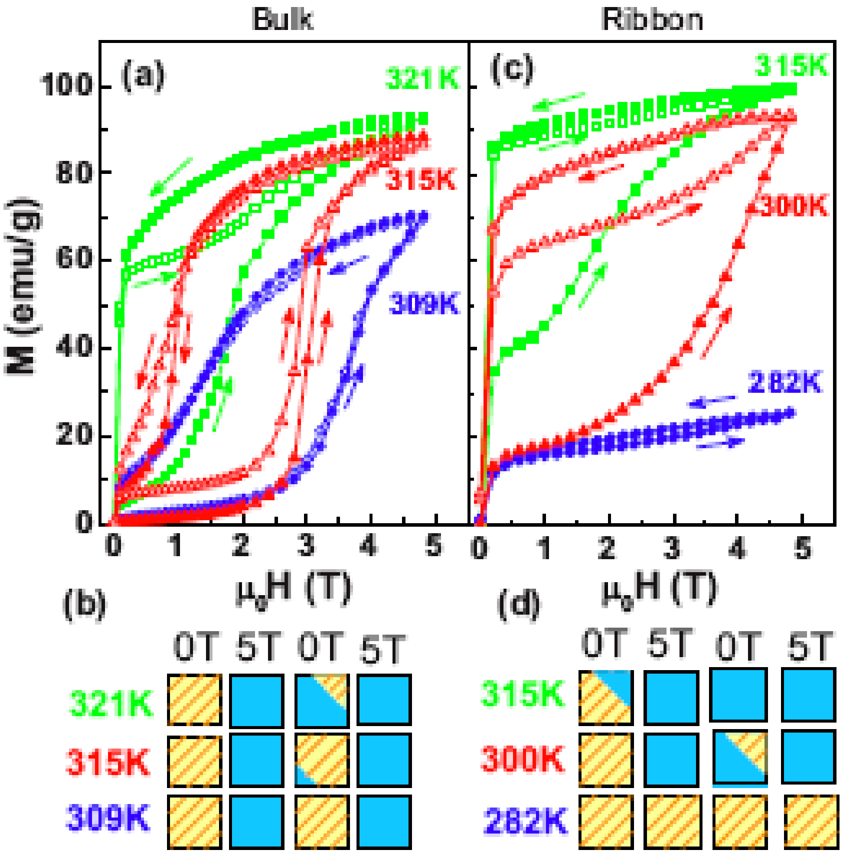

Figure 1.2 Magnetization curves at different temperatures for (a) bulk and (b) ribbon NiCoMnIn samples. The schematic represents the amount of austenite and martensite that exists in the sample at a specific temperature and magnetic field. The yellow hatched area represents martensite while solid blue corresponds to the austenite phase [38].

Figure 1.2 is an example of a how the thermal hysteresis of a MSMA affects the reversibility of a magnetostructural transition. Liu *et al.* investigated the reversibility of the magnetostructural transition in $Ni_{45}Co_5Mn_{37}In_{13}$ alloy by comparing the magnetothermal properties of a bulk sample and melt-spun ribbon made from the same alloy composition [38]. The bulk sample had a narrow hysteresis ~ 8 K, while the melt-spun ribbon had a wider hysteresis, ~ 18 K. Both samples showed a large magnetic-field induced shift of the martensite transformation temperatures -4.8 K/T for the bulk sample and -5.4 K/T for the ribbon. The bulk alloy was able to transform reversibly, while the melt-spun ribbon was only able to partially transform reversibly.

Figure 1.3 represents an ideal phase diagram for a MSMA that assumes the magnetic-field induced shift in transformation temperatures, dT/dH, is constant in the region of interest. This is a reasonable assumption for samples in moderate magnetic fields under 5T [26, 28]. Figure 1.3 is used to derive an expression to approximate the minimum applied magnetic field required to reversibly transform martensite to austenite, $H_{min} = T_{hys}/(dT/dH)$ here H_{min} is the minimum required magnetic field and $T_{hys} = (A_f - M_f)$ is the thermal hysteresis . Ideally, the applied magnetic field should be small, on the order of tens of mT, so that the magnetic field can be generated by a small excitation coil. Realistically, the magnetic field must be smaller than 2 T, as anything larger than this value requires either a superconducting magnet or pulsed magnet – both are impractical for device applications. Therefore, room temperature (RT) applications of MSMA FIPT actuators require the following:

(1) M_f is greater than RT,

(2) H_{min} is less than 2 T,

(3) small T_{hys}, and

(4) large dT/dH

While Karaca *et al.* reported a change in A_s approximately -12.6 K/T for a $Ni_{45}Mn_{36.5}Co_5In_{13.5}$ single crystal, the average value for the majority of NiCoMnIn alloys have *dT/dH* values is ~ -7 K/T [33, 34, 37, 39, 66]. This implies that thermal hysteresis needs to be less than ~ 14 K for reversible actuation in NiCoMnIn alloys.

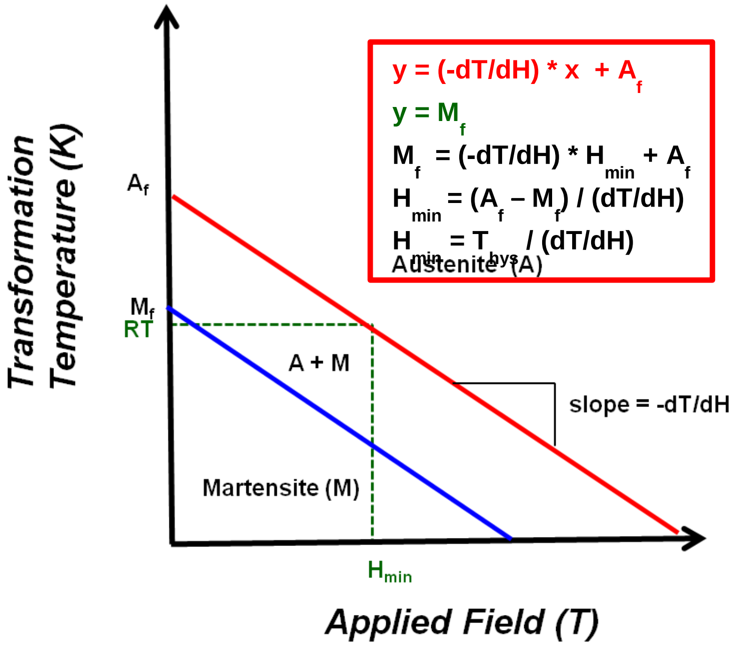

Figure 1.3 A schematic that illustrates how to graphically approximate the minimum applied magnetic field required for potential thin film application that utilizes a reversible magnetic field induced phase transformation.

1.3.2 Large thermal hysteresis applications

The first-order transition character of martensitic transformations makes the small thermal hysteresis requirement difficult to achieve for the majority of MSMAs. While thermal hysteresis is a hindrance for actuator applications, it provides an advantage for switch or fail-safe device applications.

Figure 1.4 illustrates a working concept for a passive temperature indicator that utilizes the large thermal hysteresis of a MSMA as a "switch" to monitor the supply chain of frozen food and indicate any transgression of the temperature threshold [67].

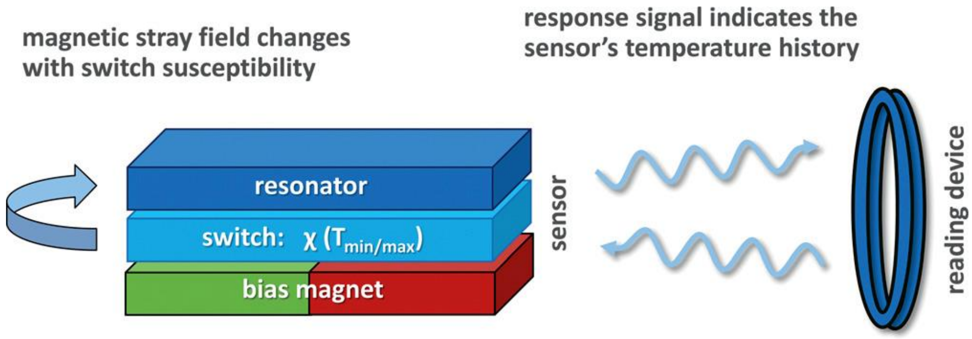

Figure 1.4 A schematic of a magnetoelastic resonance temperature indicator built consisting of a magnetostrictive amorphous alloy (resonator), a MSMA element (switch), and a permanent magnet (bias magnet) for monitoring either upper or lower temperature thresholds [67].

Nakamura *et al.* constructed a similar device using a low Curie temperature material in place of the MSMA switch to measure temperature remotely [67, 68]. Since the second order phase transformation occurs at the Curie temperature, the magnetic susceptibility is highly reversible. Therefore, a material with low Curie temperature is unable indicate a transgression of a temperature threshold.

1.3.3 Combinatorial alloy design

The relationships between a material's microstructure and physical properties are at the center of materials science. Traditionally, the microstructure and physical properties relationship as a function of chemical composition is accomplished with singular compositions prepared individually one at a time. This process is laborious and time intensive. Recently, combinatorial investigations have been used to construct functional mapping for MSMAs using high-throughput thin-film based detection techniques [69-74].

Magnetron sputtering was used to prepare a composition spread of the Ni-Ti-Cu ternary alloy, and electrical resistance measurements were used to determine the thermal hysteresis. Mapping a range of compositions of the Ni-Ti-Cu alloy led to the discovery of a $Ni_{33}Ti_{55}Cu_{12}$ with an extremely small thermal hysteresis ~ 20 °C [75]. Previous investigations for bulk compositions ranged from 47 to 52 at.% and 0 to 25 at.% Cu. Recently, Zarnetta *et al.* identified a quaternary SMA, Ni-Ti-Cu-Pd alloy, with near-zero thermal hysteresis using a thin-film composition spread technique. James and Zhang predicted that the addition of Pd to the Ni-Ti-Cu alloy would improve the coherency between the austenite and martensite interface leading to a reduced thermal hysteresis [74].

Although magnetron sputtering has been used to fabricate NiTi and NiMnGa alloys, little work has been reported in literature regarding the preparation of NiCoMnX (X = Al, In) thin films by magnetron sputtering. Compared to rapid solidification, magnetron sputtering has the advantages of precise control of film thickness with sub-nanometer precision, low surface roughness, and integration of films for device applications.

1.4 Martensitic phase transformations

Martensite is a term used to describe any diffusionless transformation product. The martensite transformation is a first-order transformation where the high and low temperature phases are called austenite and martensite, respectively. The martensite transformation is a technologically important process and associated with certain stainless steels, and quenched and tempered steels. In theory, many metals and alloys can be made to undergo diffusionless transformations provided that the cooling rate is fast enough to prevent transformation by another method involving the diffusion of atoms [76]. Martensite transformations are mainly observed in the heat treatment of alloys (e.g. steel and titanium) and in shape memory alloys, and the transformation is characterized by the appearance of martensite plates and a macroscopic shape change [77].

1.4.1 General features of thermoelastic martensite

The transformation results in transformation strains composed of shear and dilation components that are responsible for the shape and volume changes, respectively. Accommodation of these transformation strains leads to a strain energy that produces a stress field in the austenite (martensite) phase for the forward (reverse) transformations. A thermoelastic balance exists for the transformation until the stress reaches the yield stress of the austenite phase resulting in plastic accommodation by dislocation motion.

Thermoelastic transformations (shape memory alloys) and non-thermoelastic martensitic transformations (steels) differ in that the macroscopic transformation strain is not reversible for non-thermoelastic martensitic transformations. The difference between the thermoelastic and non-thermoelastic behavior is characterized by the width of the hysteresis loop. Copper-based shape memory alloys have hysteresis in the range of 5 to 15 °C , while steel have hysteresis between 200 to 400 °C [77].

1.4.2 Thermodynamic framework

Kurdjumov developed the central idea that thermoelastic martensite transformation behavior is governed by an equilibrium balance between chemical and nonchemical forces, which continuously evolves as the martensite plate grows or shrinks [78]. The equilibrium balances associated with thermoelastic martensite transformation are local in nature. This local character explains why the growth and shrinkage of martensite plates occur sequentially. That is the first plates formed during cooling are the last plates to shrink upon heating during the reverse transformation. Chemical forces are associated with the chemical composition and atomic ordering of the alloy, while nonchemical forces include elastic and frictional terms. In the case of magnetic shape memory alloys, magnetic energy provides an additional nonchemical force. A thermodynamic framework of the thermoelastic martensite transformation has been treated by Ortin and Planes, and their framework is outlined in this section [78].

The equilibrium condition for the forward transformation can be expressed using the Gibbs free energy per mol of the moving plates.

$$G^{P\rightarrow M} = -\Delta G_{ch}^{P\rightarrow M} + \Delta G_{nch}^{P\rightarrow M} = 0 \qquad \text{Equation 1.1}$$

The superscript P→M refers to the forward transformation, while the subscripts denote the chemical and non-chemical contributions to the transformation. For clarity, the quantities are taken as positive, and a minus sign is used to denote negative values. The chemical free energy, $-\Delta G_{ch}^{P\rightarrow M}$, represents the change in the structural contribution of the martensite and austenite phases. In an ideal situation, where the parent phase was both defect-free and strain-free, $-\Delta G_{ch}^{P\rightarrow M} = 0$ at an equilibrium temperature $T = T_0$. The exothermic transformation would continue isothermally at $T = T_0$ releasing heat up to an amount equivalent to the latent heat of transformation, $-\Delta H_{ch}^{P\rightarrow M}(T_0)$ [78].

As the name suggests, a thermoelastic transformation elastically accommodates shape and volume changes with the transformation in order to minimize the strain energy associated with the volume change. The reversible elastic strain energy, $\Delta G_{el}^{P\rightarrow M}$, includes the interfacial energy associated with single or multiple interfaces and the elastic energy resulting from elastic strains. If no other non-chemical energies are considered, then the martensite transformation proceeds reversibly without a thermal hysteresis. However, Olson and Cohen have shown that elastic barriers to martensite nucleation result in a small hysteresis [79, 80]. The presence of a hysteresis loop indicates irreversible processes, such as frictional resistance to interface motion, transformation induced defects (stacking faults, twin boundaries), and plastic accommodation of the transformation strains [78]. The sum of the irreversible terms are grouped in one term, $E_{fr}^{P\rightarrow M}$.

Separating the non-chemical energies into reversible and irreversible components leads to the following equation.

$$\Delta G_{nch}^{P\to M} = \Delta G_{el}^{P\to M} - \Delta G_{mech}^{P\to M} + E_{fr}^{P\to M} \qquad \text{Equation 1.2}$$

where $\Delta G_{mech}^{P\to M}$ is the mechanical energy applied during the phase transformation [4]. In bulk alloys, tensile and compressive stresses tend to increase the transformation temperature, and a hydrostatic pressure may either increase or decrease the transformation temperature depending whether pressure aids or opposes the forward transformation. On the other hand, thin film materials are typically under a biaxial stress which leads to a hydrostatic pressure condition. Substituting Equation. 1.2 into Equation. 1.1, results in the following local balance for the forward transformation at individual austenite-martensite interfaces.

$$-\Delta G_{ch}^{P\to M} + \Delta G_{el}^{P\to M} - \Delta G_{mech}^{P\to M} + E_{fr}^{P\to M} = 0 \qquad \text{Equation 1.3}$$

While the chemical Gibbs free energy, $-\Delta G_{ch}^{P\to M}$, is constant throughout a homogeneous material, the other non-chemical terms are inhomogeneous. In general, this explains why the forward transformation does not transform homogenously.

The ferromagnetic properties of magnetic shape memory alloys require additional non-chemical terms in the thermoelastic balance. Equation 1.3 can be modified to include the effects of an applied magnetic field to a magnetic shape memory alloy.

$$\Delta G_{nch}^{P\to M} = \Delta G_{el}^{P\to M} - \Delta G_{mech}^{P\to M} + \Delta G_{mag}^{P\to M} + E_{fr}^{P\to M} \qquad \text{Equation 1.4}$$

where magnetic contribution of the Gibbs free energy can be expressed as

$$\Delta G_{mag}^{P\to M} = \mu_0 \Delta M^{P\to M} dH + \Delta S_{mag}^{P\to M} dT \qquad \text{Equation 1.5}$$

The total entropy can be expressed by the following expression [81, 82].

$$\Delta S_{tot} = \Delta S_{lat} + \Delta S_{elec} + \Delta S_{mag} \qquad \text{Equation 1.6}$$

where $\Delta S_{lat}, \Delta S_{elec}, and\ \Delta S_{mag}$ are the lattice (configuration), electronic, and magnetic contributions to the change in entropy associated with the phase transition. In a solid, the configurational change in entropy usually remains constant when a magnetic field is applied, and since $S_{lat}^{P} > S_{lat}^{M}$, $\Delta S_{lat} < 0$. The sign of the magnetic contribution of the entropy, ΔS_{mag}, depends on the magnetization of the austenite and martensite phases. If austenite posses a larger magnetization than martensite, then $\Delta S_{mag} > 0$, since austenite has a higher magnetic ordering, and the opposite is true for the converse. The electronic contribution of the conduction electrons is negligible below or near the Debye temperature [82]. Overall considering the effect of an applied magnetic field, the magnetic field stabilizes the phase with the highest magnetization.

1.4.3 Chemical composition and atomic ordering

Chemical composition

Many properties of martensitic Heusler alloys, such as volume, magnetic moment, and transition temperatures can be related to the valence electron concentration (*e/a*). The valence electron concentration can provide a useful map or guide to tailor the multifunctional properties of Heusler alloys [83-85]. Figure 1.5 represents a collection of phase diagrams for Ni-Mn-Z (Z = Ga, In, Sn, and Sb) alloys that illustrates the e/a dependence on the transformation and Curie temperatures.

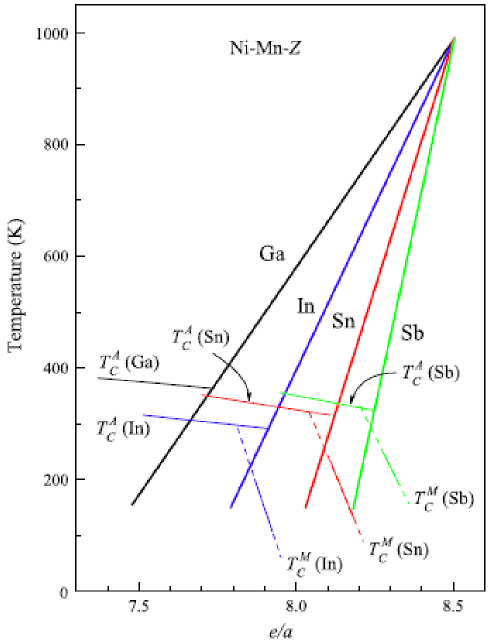

Figure 1.5 The e/a dependence of the martensite start temperature (M_S) and the Curie temperature (T_c) for both austenite and martensite states of Ni-Mn-Z alloys where Z = Ga, In, Sn, and Sb [85].

All the alloys share the same starting point that originates from the alloy composition common to all the alloys, $Ni_{50}Mn_{50}$ with *e/a* = 8.5, which corresponds to a tetragonal $L1_0$ structure at high temperature ~1000 K. The martensite start temperature decreases significantly for small changes in chemical composition with a distinctive slope for each Z species when the alloy is diluted with the third Z element. For example, the magnitude of the slopes ranges from ~80 K per 0.1 *e/a* and ~270 K per 0.1 *e/a* for Z = Ga and Sb, respectively [85].

Additionally, while the martensite start temperature decreases rapidly with *e/a*, the dependence on the Curie temperature is not as pronounced, although the austenite Curie temperature decreases with increasing *e/a*. The *e/a* dependence is related to the ferromagnetic coupling weakening as the amount of Mn increases, which decreases the Mn-Mn distance or enhances the number of Mn-Mn interaction – both lead to a decrease in ferromagnetism and eventually a drop in the Curie temperature.

Atomic ordering

In 1903, F. Heusler discovered that the Cu_2MnAl alloy was ferromagnetic even though the constituent elements are not individually ferromagnetic. Twenty years later, Potter and Persson individually showed that the atomic ordering and concentration of the Mn atoms were responsible for the ferromagnetic properties [86]. Heusler alloys X_2YZ are in the cubic space group Fm3m, and are composed of four interpenetrating fcc lattices where two are occupied equally by the X atoms, while the other two are occupied with Y and Z atoms. X and Y atoms are transition metals, and the Z atom is a main group element. The X, Y, and Z atoms Wyckoff positions are located at 8c (1/4,1/4,1/4), 4a (0,0,0), and 4b (1/8,1/8,1/8), respectively [87]. The Mn-Mn distance significantly influences the ferromagnetic properties of Heusler-type alloys [88, 89], and the atomic ordering has been known to influence the martensite transformation temperatures in magnetic shape memory alloys.

Recarte et al. studied the dependence of the martensite transformation and magnetic transition on the atomic order of Ni-Mn-In metamagnetic shape memory alloys [90]. Patak et al. studied the effect of partially substituting cobalt for nickel on the electrical and magnetic properties of $Ni_{50}Mn_{35}In_{15}$ alloy [91]. Reacarte et al. investigated how the stability between austenite and martensite was affected by the atomic ordering in a Ni-Mn-In alloy [92]. Wang et al. reported the effect of post-annealing on the phase transformations and bulk properties of Ni44Mn45Sn alloy [93]. Segui and Cesari investigated how thermal treatments affect the structural and magnetic transformations and related entropy changes in a Ni-Co-Mn-Ga alloy [94].

Figure 1.6 shows the temperature dependence on the magnetization of two NiCoMnIn alloys quenched at 623 and 923K. The specimens were measured in magnetic fields of 0.5 and 7 T. Both sample water quenched from 1173 K, which is above the $B2/L2_1$ order-disorder temperature, $T_o^{B2/L2_1}$ = 896 K. The samples were annealed for 24 h at 623 and 923 K, and resulted in a fully ordered $L2_1$ and partially ordered B2 phase, respectively [95]. Two things are important to note. One, the Curie temperature of the B2 phase is ~ 30 K lower compared to the ordered $L2_1$ phase. Second, The $L2_1$ phase stabilizes the austenite phase at lower temperatures, since the transformation occurs ~ 80 K lower compared to the more disordered B2 phase.

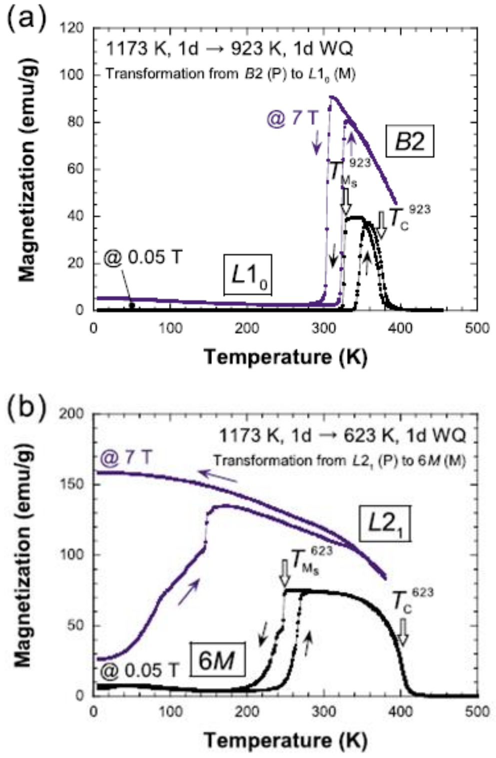

Figure 1.6 Thermomagnetization curve for two NiCoMnIn samples quenched from (a) 923 and (b) 623 K. Both samples were measured in magnetic fields of 0.05 and 7 T [95].

Tong and Wayman used a quasi-chemical approach to qualitatively describe why increased austenite ordering depresses the equilibrium temperature T_0, which can be bracketed between M_s and A_f for thermoelastic martensitic transformations.

The reason for the behavior was expressed by the following latent heat equation.

$$\frac{\Delta H_{AA}+\Delta H_{BB}}{2} > \Delta H_{AB} \qquad \text{Equation 1.7}$$

where the left hand of the equation represents the latent heat released during a martensite transformation, while the right side of the equality refers to the latent heat released during a martensite transformation for an ordered alloy. Thus, we see that the latent heat of transformation is larger in disordered alloys compared to ordered alloys. In the same paper, Tong and Wayman develop an expression that relates the amount of required undercooling to overcome the saturated nonchemical forces [96].

$$\frac{\Delta T}{T_0} = \frac{\Delta \varepsilon_{nc}}{\Delta Q} \qquad \text{Equation 1.8}$$

where ΔT represents the amount of undercooling, T_0 is the equilibrium temperature, $\Delta \varepsilon_{nc}$ is the saturated nonchemical energy associated with ΔQ, the latent heat of transformation. Therefore, from Equations 1.7 and 1.8 we see that increased atomic ordering leads to a larger undercooling.

1.4.4 Effect of precipitates on Ms

Coherent precipitation hardening is a common technique used to improve the shape memory and mechanical properties of SMAs [97-99]. Formation of precipitates alters the local composition of an alloy, and introduces coherent/incoherent interface with the matrix. The change in the matrix chemical composition alters the average electron concentration in the matrix, and the slightest change in the local composition of a magnetic shape memory alloy will significantly affect the transformation temperature as discussed earlier in *Section 1.4.1*.

A number of studies on NiTi have been reported on appropriate heat treatments can lead to improved shape memory and mechanical properties [100]. The change of M_s temperature in NTi-based SMAs depends on how the formation of precipitates changed the average composition of the matrix. For instance, an increase in *e/a* density ($\sim e/a/V_{cell}$)

resulted in a decrease in transformation temperatures, while an increase in transformation temperatures was observed for a decrease in *e/a* density.

Precipitation in NiMn-based MSMAs tends to produce Ni-rich precipitates, which reduces the average chemical composition of the matrix. In contrast to NiTi-based SMAs, the M_s temperature decreases in NiMn-based MSMAs as *e/a* of the matrix decreases. The difference is due to *e/a* dependence of M_s temperature for NiTi- and NiMn-based alloys. NiTi-based SMAs have a negative Ms vs. *e/a* slope, while the slope is positive for NiMn-based alloys.

1.4.5 Effect of stress on Ms – applied and residual

Applied stresses

Historically, a shear-stress criterion was used to describe the martensite formation as a strain transformation where the martensitic transformation competes with slip when external stresses are applied to the parent phase [101]. While the required shear stress required to initiate yielding by slip increases as temperature decreases, the shear stress required to activate the martensitic transformation mode decreases as the temperature approaches the martensite start temperature. Therefore, on one hand, at or near the martensite temperature, M_s, applied stresses should initiate plastic yielding by a martensitic transformation rather than by slip. On the other hand, at temperatures well above the M_s temperature, slip is the primary mode of deformation.

Figure 1.7 illustrates the change in M_s temperature of a carbon-nickel steel bar under uniaxial tension and uniaxial loads, and the M_s temperature response of a nickel-iron alloy rod to increased amounts of hydrostatic pressure. The corresponding slopes for the tension, compression, and hydrostatic pressure loads were 1.0, 0.65, and -0.57 °C/psi, respectively.

The difference in slopes for the tension and compression cases is at odds with a criterion based on shear stress alone, since the shear components are identical. Additionally, the change in sign for the hydrostatic case suggests that the shear-stress criterion is unable to account for the difference in slopes.

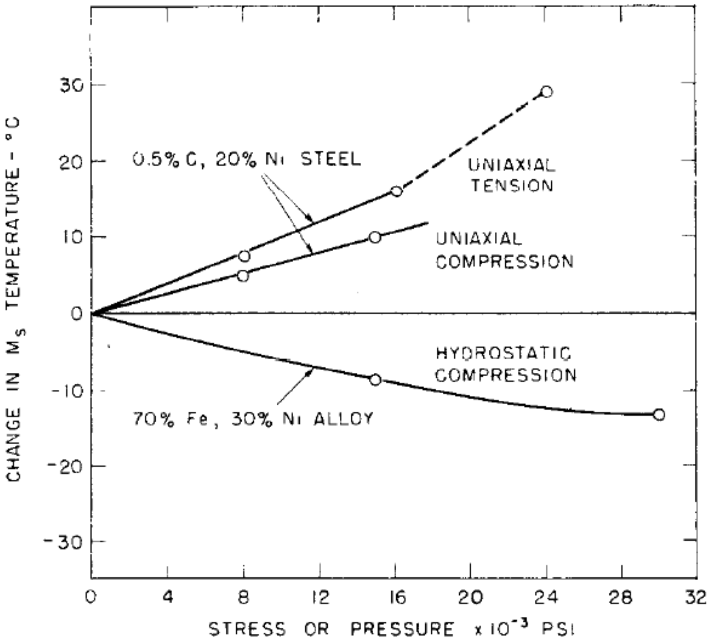

Figure 1.7 The stress or pressure dependence on the change in martensite start temperature (M_s) of iron-nickel alloys [101].

Cohen and Patel argued that Scheil's concept of a shear-stress criterion was invalid since it did not account for normal components of the applied stress [101]. They argued that the dilational component of the martensite transformation strain was responsible for asymmetric nature of the change in M_s when subject to uniaxial tension and compression loads. They proposed a criterion based thermodynamics where the applied stress was resolved into shear and normal component to describe how applied stresses affect the martensite transformation temperatures in steels and iron-based alloys. The following discussion outlines their criterion for applied stresses and its effect on martensitic transformations.

The work (W) associated with the applied stress is decomposed into two components: the shear stress times the shear strain ($\tau\gamma_0$), and a normal stress perpendicular to the habit plane times the transformation strain in the normal direction ($\sigma\varepsilon_0$). Therefore, the work done on or by the transformation can be expressed with the following expression

$$W = \tau\gamma_0 + \sigma\epsilon_0 \qquad \text{Equation 1.9}$$

A couple of things are worth noting. The first term on the left-hand side of the equation is always positive, since the product of the shear stress and stain is always positive. The sign of the second term is positive when the normal stress component aids the transformation and negative when the normal stress suppresses the transformation [101].

Figure 1.8 shows how a Mohr circle is used to determine the shear and normal components of the applied stress in terms of the applied stress orientation with respect to the habit plane. Substituting these expressions back into Equation 1.9 produces a function that relates the work associated with the transformation to the orientation between the stress axis and the habit plane.

$$W = \frac{1}{2}\gamma_0\sigma_1 \sin\theta \pm \frac{1}{2}\epsilon_0\sigma_1(1 + \cos 2\theta) \qquad \text{Equation 1.10}$$

Optimizing Equation. 1.10 allows one to determine the orientation that yields the maximum work (W_{max}) available to contribute or subtract from the Gibbs chemical free energy.

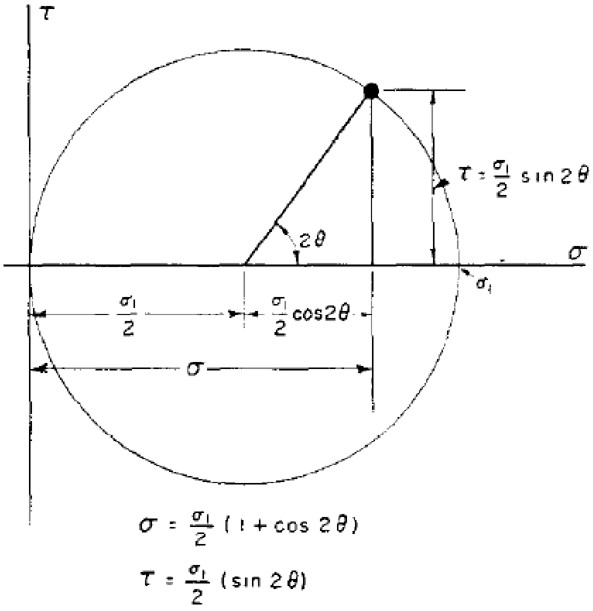

Figure 1.8 Mohr's circle for tension showing shear (τ) and normal (σ) components of stress as a function of the applied stress (σ_1), and the orientation (θ) between the stress axis and the normal to the habit plane [101].

A positive value of W_{max} reduces the required driving force to initiate a martensite reaction; hence, the M_s temperature is raised by the applied stress. Additionally, this quantitatively explains the differences in material response to an uniaxial compression and uniaxial tensile stresses. Both applied stresses result in an increase in transformation temperature as the stress increases due to the fact that the shear stress component are positive, and this aids the transformation more effectively than the normal component [101]. However, under uniaxial tension, the positive normal component aids the transformation, while under uniaxial compression the negative normal component opposes the transformation. Therefore, the Ms temperature increases at a higher rate under uniaxial tension compared to uniaxial compression. Finally, increasing hydrostatic pressure reduces M_s due to the absence of a shear component and negative normal component that suppresses the transformation strain.

Residual thermal stresses in thin films

Residual thermal stresses arise in thin films due to the mismatch in coefficients of thermal expansion between the film and substrate. Doyle *et al.* used XRD stress measurements to investigate the effect of residual stresses in Ni-Mn-Ga thin films on different substrates [102].

Figure 1.9 (a) shows the film thickness dependence on the in-plane residual stress, while Figure 1.9 (b) shows the film-thickness dependence on both the Curie and transformation temperatures. Films deposited onto silicon and MgO substrates showed an inverse thickness dependence on residual stress when the film thickness decreased below sub-micron thicknesses.

The increase in residual stress is due to film/substrate interface interactions that obstruct dislocation activity [102, 103]. Contrary to the films deposited on Si and MgO, the residual stress decreased for films deposited onto Mo and Al_2O_3 substrates when the film thickness was reduced to sub-micron thicknesses. The decrease of residual stress was attributed to the surface roughness of the substrates.

Films deposited on Mo and MgO showed little variation in residual stress as the film thickness decreased corresponding to little variation in transformation temperatures. The transformation temperature decreases for films deposited on Si as the film thickness decreases and the residual tensile stress increases. The opposite trend is seen for decreasing film thickness on films deposited on Al_2O_3 with a decreasing tensile residual stress. While these two observations seem contradictory, these results align with Cohen and Patel's stress criterion discussed in the previous section. That is, thin films are in a plane-stress, and do not have shear stresses. Thus according to Cohen and Patel, a biaxial residual tensile stress is similar to a hydrostatic pressure that opposes the transformation strain and leads to a decrease in transformation temperature for increased biaxial tensile stresses.

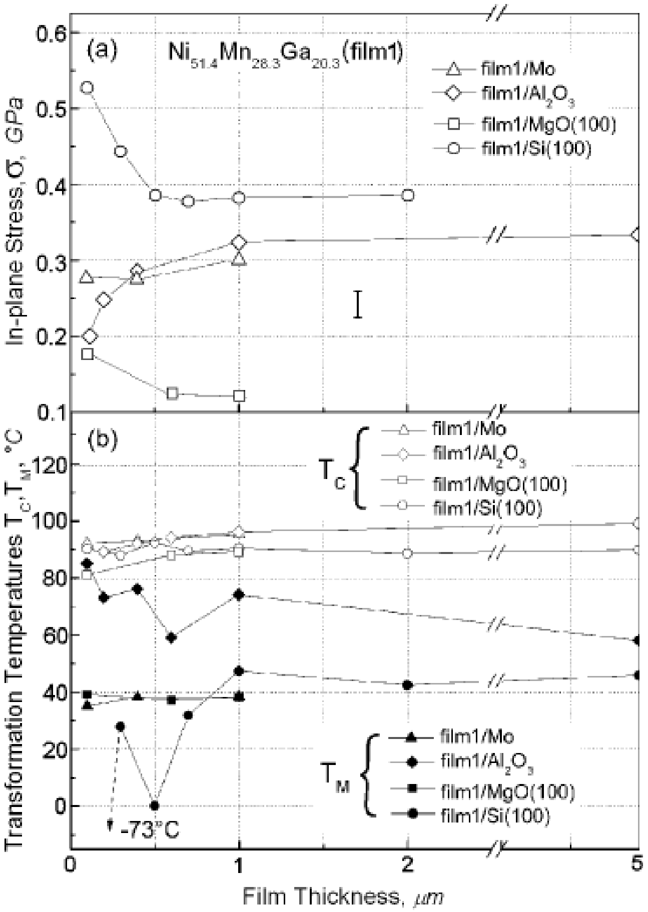

Figure 1.9 (a) The thickness dependence of residual stress measured at 150 °C, and (b) the martensitic (T_M) or Curie temperature (T_C) for Ni-Mn-Ga film attached to various substrates [102].

1.4.6 Size effects on Ms

Grain size effects in bulk

Salzbrenner and Cohen observed that multiple-interface transformations in Cu-14Al-2.2Ni alloys significantly depressed the martensite start temperature due to additional storage of elastic energy and increased frictional resistance compared to a single crystal. Additionally, they were able to measure thermodynamic quantities as a function of decreasing grain size [104]. The stored elastic energy was measured, and amounted to approximately 15% of the chemical enthalpy change.

Figure 1.10 illustrates the forward and reverse transformations for three different samples of a Cu-14Al-2.5Ni alloy. Figure 1.10 (a) is a single crystal that was cooled in thermal gradient, and it was observed that measured temperature was the same as the interface passed each thermocouple. Since elastic forces were absent in the single-interface run, the hysteresis was due solely to frictional resistance opposing the interface. The same single crystal was used in Figure 1.10 (b), except this time the sample was heated uniformly, and this resulted in the formation of multiple interfaces. The difference in Figures 1.10 (a) and (b) were a result of stored elastic energy in the single crystal made to undergo multiple-interface transformations. It is important to note that an equilibrium temperature can be determined using the result from Wayman and Tong that $T_0 = ½(M_s + A_f)$ [96, 104].

Figures 1.10 (c) and (d) demonstrate how the influence of stored elastic energy becomes more apparent in polycrystalline samples with different grain sizes. Most striking is the decrease in the transformation temperatures ~ 25 °C. Clearly, the increase in stored elastic increases undercooling, and if one were to incorrectly use the shifted values for M_s and A_f to calculate $T_{0,}$ discrepancies would be introduced into further additional thermodynamic calculations.

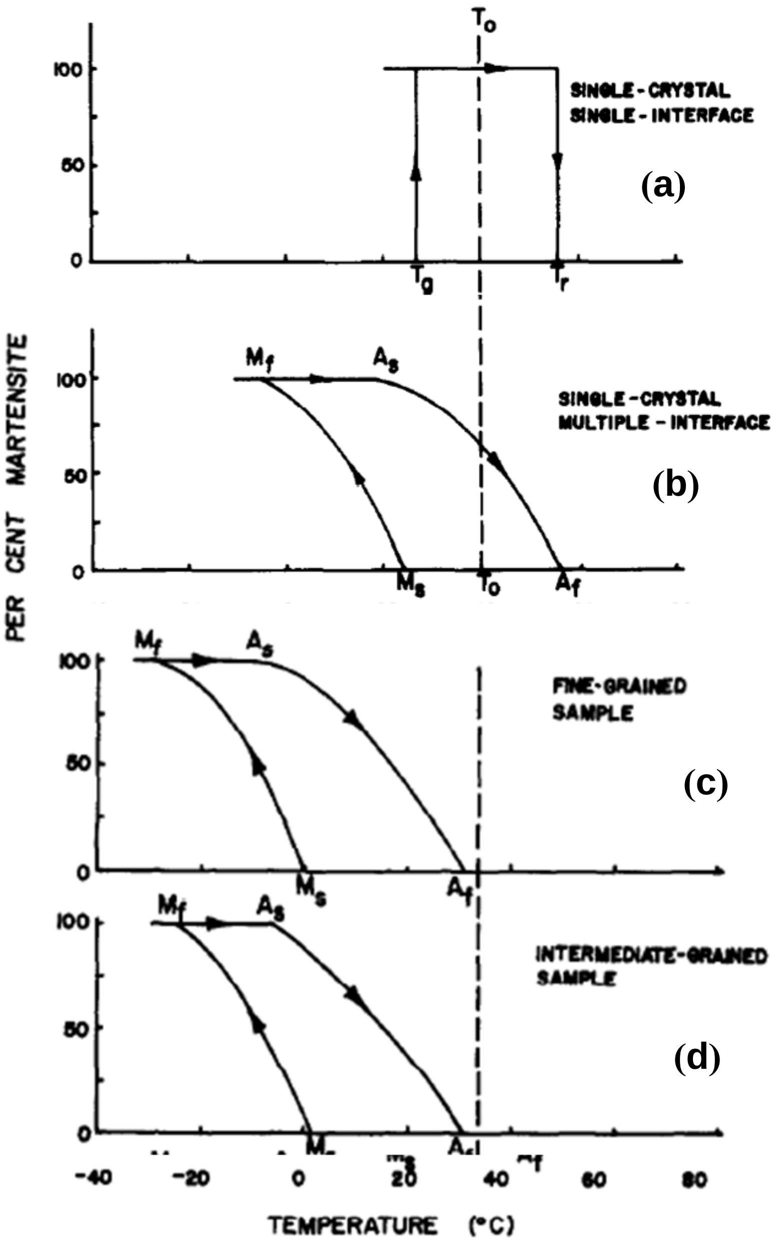

Figure 1.10 Transformation hysteresis curves for Cu-14Al-2.5Ni with different grain sizes (a) single crystal with single-interface transformation, (b) single crystal with multiple interface transformation, (c) fine-grained (d=0.5 mm), and (d) coarse-grained (d = 4.0 mm). Modified from [104].

Salzbrenner and Cohen performed an interesting experiment where they electroplated the single crystal sample with ~25 µm of nickel to inhibit surface nucleation and increase undercooling. The transformation temperature of the plated sample was reduced by 6 °C and the latent heat decrease ~ 18% [104].

Thin film confinement

Thin film materials are used in several engineering systems such as, integrated electronic circuits, high temperature surface coatings, tribological coatings, and mico-electrical-mechanical systems (MEMS). A surface coating or film is defined as a thin film when the film thickness is small compared to the supporting substrate (typically by a factor of 50 or more) [105]. When the thickness of the film approaches micron size scale dimensions, the thin film mechanical and physical properties are influenced to a greater degree by factors such as grain size and crystallographic texture. For example, thin films exhibit higher yield stresses compared to their bulk counterpart. This is due mainly to decreased dislocation mobility (see Figure 1.11).

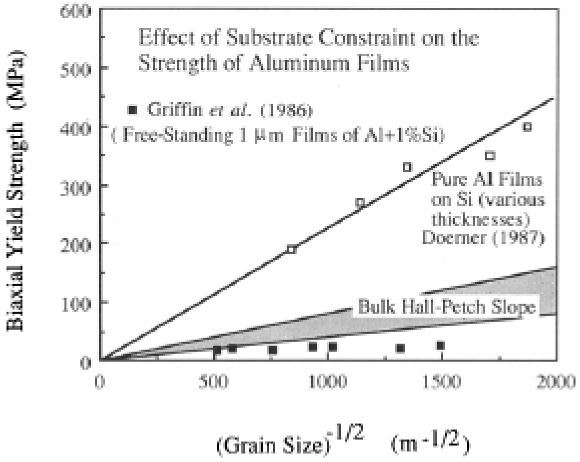

Figure 1.11 The grain size dependence of biaxial yield strength of aluminum films on silicon substrates and freestanding films. Thin film confinement on the substrate results in increased strength compared to freestanding films [103].

Additionally, the magnetic properties of thin films are strongly influenced when the grain size of the film drops below the exchange length. Therefore, it is interesting on two levels to study the effect of grain size on the martensitic transformation temperatures of thin films.

1.5 Brief history and crystal structures of NiCoMnIn

The NiCoMnIn Heusler alloy is part of an unusual group of magnetic alloys that exhibit a martensitic phase transformation where the parent and martensite have ferromagnetic and paramagnetic properties, respectively. Additionally, the martensite start temperature can be changed with an applied magnetic field. Ni-Mn-Ga, a well-studied magnetic shape memory alloy (MSMA), has been used for thin film microactuators. However, Ni-Mn-Ga uses a magnetically induced reorientation of the martensite variants as actuator mechanism and work output is limited by the magnetocrystalline anisotropy, whereas NiCoMnIn uses a magnetically induced austenite (MIA) as an actuation mechanism which allows for a significant increase in work output that is limited by difference in magnetic energy of the parent and martensite phase.

Although bulk NiCoMnIn alloys are a recent member of MSMAs, and investigations on this alloy system have been active since 2006, focusing on microstructure, phase transformation, magnetic properties and field induced phase transformations [27, 28, 35, 106]. However, studies for NiCoMnIn thin films are scarce. Only a few reports discuss the fabrication of NiCoMnIn alloy thin films [30, 41], and until now, only epitaxial NiCoMnIn grown on MgO have shown the MIA effect for potential use as a micro actuator.

1.5.1 Crystal structure

The crystal structure of NiCoMnIn alloys is based on the stoichiometric Ni_2MnIn Heusler alloy. While stoichiometric Ni_2MnGa exhibits a martensitic transformation, a martensitic transformation is not observed for Ni_2MnIn – however, it does exhibit ferromagnetism where the Curie temperature ~ 300 K [107]. However, off-stoichiometric compositions of $Ni_{50}Mn_{50-x}In_x$ (x = 15, 10, and 5 at%) alloys do exhibit a martensitic transformation.

The crystal structures of the austenite and martensite phases are illustrated below in Figure 1.12 Ito *et al.* characterized the crystal structure of several Ni-Mn-In and Ni-Co-Mn-In alloys. The selected area diffraction (SAD) patterns are taken from the martensite and austenite phases are shown in Figure 1.12. The $L2_1$ superlattice reflection, which is characteristic of the ordered $L2_1$ structure, is clearly observed [29]. From the SAD, the martensite phases were determined to have a mixture 10M and 14M modulated martensite. Kainuma *et al.* determined the lattice parameters of the austenite and martensite phases using XRD, and reported that the parent and martensite phases have the $L2_1$ Heusler-type ordered structure where a = 0.5978 nm and the 14M modulated structure where a = 0.4349 nm, b = 0.2811 nm, c = 2.9892 nm and = 93.24°, respectively [34].

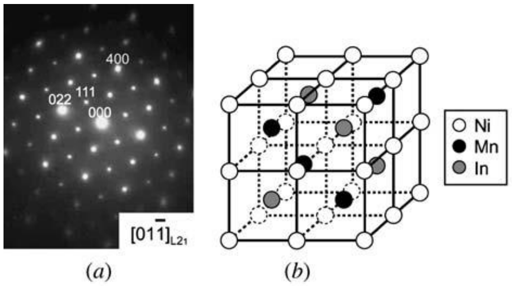

Figure 1.12 Selected area diffraction patterns from (a) parent phase, and (c) and (d) martensite phases for $Ni_{45}Co_5Mn_{36.7}In_{13.3}$ alloy. The crystal structures for (b) L21 parent phase and (e) $(220)_{L21}$ basal plane and (f) 10M and (g) 1M martensite phases [29].

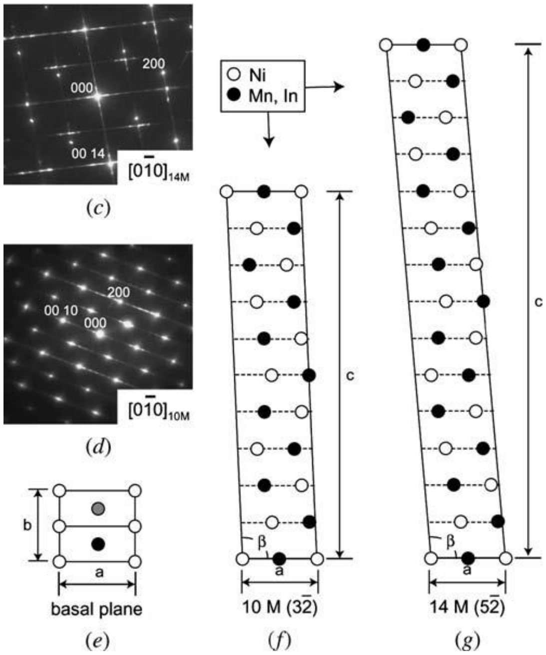

Figure 1.12 continued

1.5.2 Atomic ordering

Like other SMAs, the structural and physical properties of NiMnCoIn alloys are sensitive to the alloy's composition and atomic order. Ito et al. reported that the martensitic temperature of a Heusler-type NiCoMnIn alloy decreased by approximately 500 K by increasing the indium concentration by a few atomic percent [29]. In a separate study, the effect of atomic ordering on a NiCoMnIn alloy was investigated and the martensitic start temperature from the fully ordered $L2_1$ structure was 333 K less than the partially ordered B2 austenitic phase [31]. Annealing has been used to influence the physical properties of SMAs, and in some cases results in precipitates that affect the ductility of SMAs as well as the transformation temperatures[38, 108-110]. Magnetic field induced phase transformation has also been observed in NiCoMnIn ribbons prepared by rapid solidification [36, 37, 39, 111].

Miyamoto *et al.* have recently investigated the order-disorder temperature for the $Ni_{50}Mn_{50-x}In_x$ alloy system [40]. DSC was used to determine the order-disorder temperature for the Ni-Mn-In alloy system, where corresponding endothermic and exothermic peaks marked the order-disorder temperature. Figure 1.13 (a) shows the DSC heating and cooling curves for $Ni_{45}Mn_{35}In_{20}$ alloy.

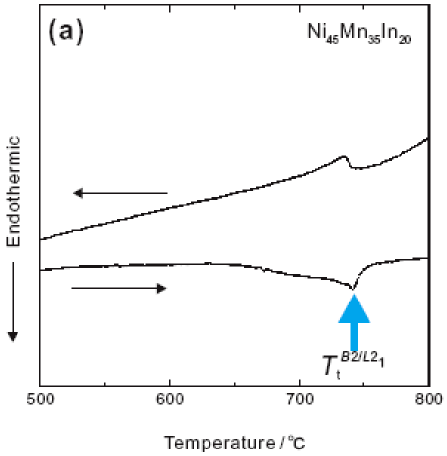

Figure 1.13 (a) DSC heating and cooling curves of the $Ni_{45}Mn_{35}In_{20}$ alloy. The critical temperature of order-disorder transition temperature is marked by the minimal point in the heating curve (bottom curve) as indicated by $B2/L2_1$ arrow. (b) The critical order-disorder temperatures for $B2/L2_1$ compositions are represented with a symbol (+) [40].

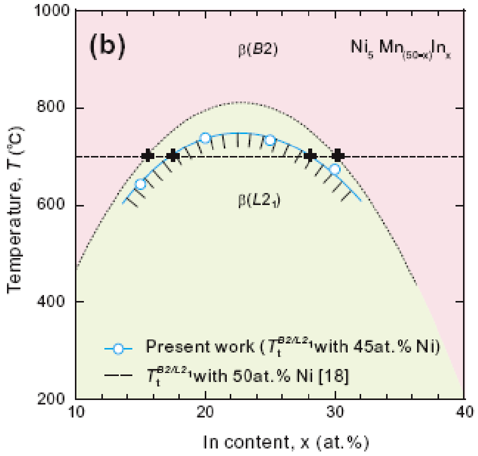

Figure 1.13 continued

1.5.3 Magnetic field induced phase transformation

In 2006, Kainuma *et al.* reported that the $Ni_{45}Co_5Mn_{36.6}In_{13.4}$ alloy exhibited a martensitic transition from the ferromagnetic austenite phase to the paramagnetic or antiferromagnetic martensitic phase, and the transformation temperatures decreased when a magnetic field was applied (see Figure 1.14) [34].

Additionally, compressive testing was used to investigate the stress-strain behavior of the austenite and martensite phases of NiCoMnIn single crystals. A compressive strain ~7% was applied at room temperature. The $Ni_{45}Co_5Mn_{36.5}In_{13.5}$ alloy ($A_s = 235$ K, $A_f = 273$ K) showed almost perfect pseudoelasticity.

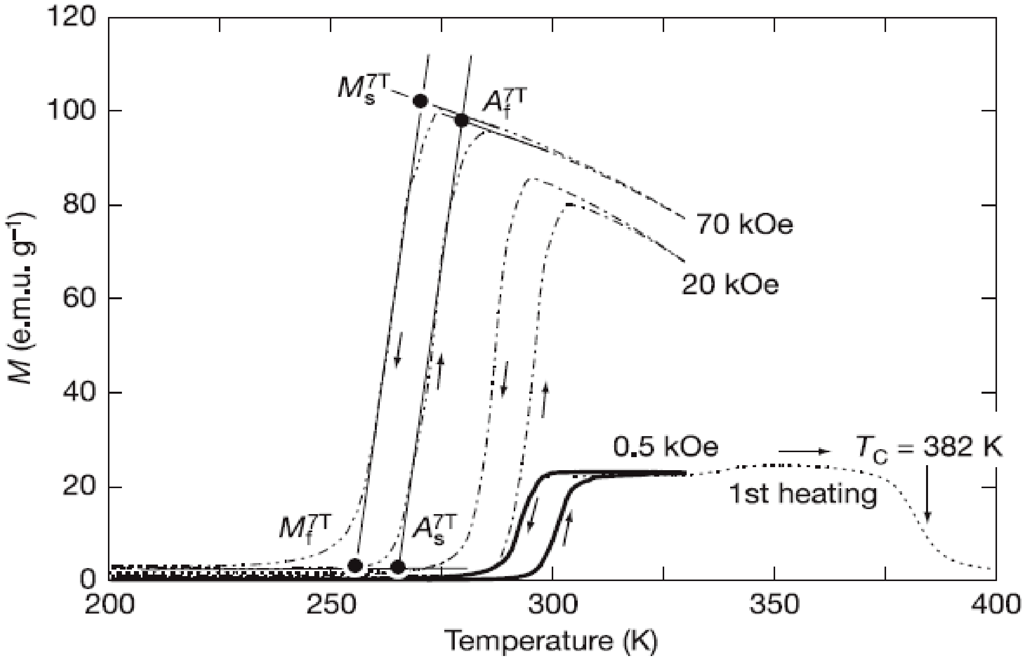

Figure 1.14 Thermomagnetization curves of the Ni45Co5Mn36.6In13.4n alloy measured in 0.5, 20, and 70 kOe magnetic fields (10 kOe = 1 T). The sample was quenched from 1173 K [34].

Finally, they demonstrated shape recovery from a ~3% compressive pre-strain induced by a magnetic field. Since this recovery or shape-memory effect is analogous to the traditional shape-memory effect induced by heating, Kainuma *et al.* proposed and coined the term "metamagnetic shape-memory effect" to describe the shape-memory effect due to a magnetic field induced phase transformation [34].

1.6 Brief history and crystal structures of NiCoMnAl

Recently, NiCoMnAl has been identified as a metamagnetic shape memory alloy after replacing expensive indium with inexpensive aluminum [31]. In contrast to the brittle

NiCoMnIn alloys, the grain boundaries of NiCoMnAl alloys have relatively high strength and even polycrystalline alloys can be deformed under compression, indicating enhanced deformability [26, 54].

1.6.1 Crystal structure

NiCoMnAl alloys are base on the B2-type NiMnAl alloys. These alloys were originally investigated for potential use as high temperature shape memory alloy applications [112]. Kainuma *et al.* used XRD at RT to determine the lattice parameters for B2-type NiCoMnAl alloys two different compositions that corresponded to a austenite and martensite phase. The diffraction lines of the parent composition, $Ni_{40}Co_{10}Mn_{32}Al_{18}$ was indexed as a cubic B2 structure where a_{B2} = 3.885 Å. The diffraction lines of the martensite composition $Ni_{40}Co_{10}Mn_{34}Al_{16}$ was indexed as tetragonal $L1_0$ crystal structure where a_{L10} = 3.885 Å and c_{L10} = 3.306 Å [31].

Figure 1.15 shows the three phase diagrams, the parent (β:B2) phase and martensite phase (β':$L1_0$).

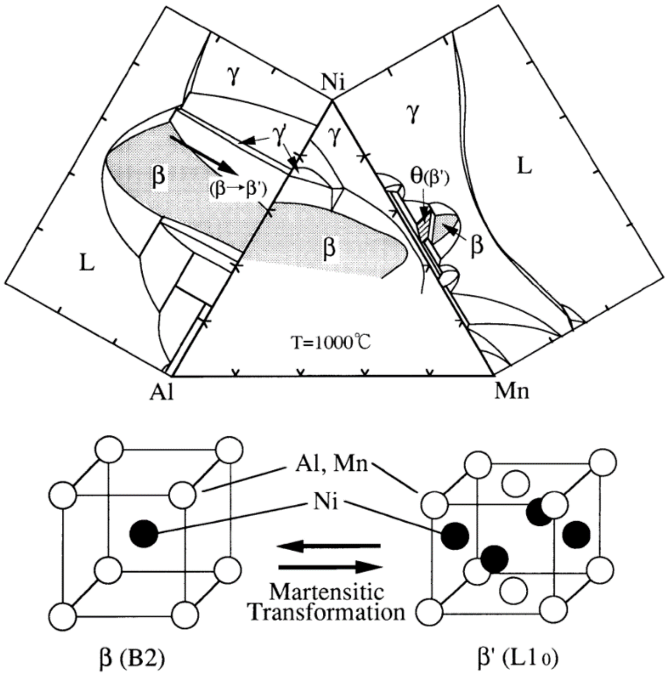

Figure 1.15 Phase diagram of the Ni-Mn-Al alloy system and martensitic transformations from the β (B2) to β’ (2M:$L1_0$) phases in Ni-Al and Ni-Mn binary systems [112].

The Ni-Mn and Ni-Al binary phase diagrams indicate a martensitic transformation from the B2 to $L1_0$ phase near equiatomic compositions, while the ternary phase diagram indicates illustrates that a two-phase structure consisting of β + γ (B2 + fcc) phases exist for a broad range in the Ni-Mn-Al ternary alloy [112].

1.6.2 Atomic ordering

Similar to the NiCoMnIn alloy system, the L2$_1$/B2 order-disorder temperatures for NiMnAl were determined form DSC measurements [113]. The data from the DSC measurements were plotted in Figure 1.16 for two different alloy systems. In one alloy, the amount of manganese was varied from 15 to 25 at.% (see Fig 1.16 (a)). In the other alloy, the aluminum was varied from 15 to 25 at.% (see Figure 1.16 (b)). The aluminum content was found to significantly affect the order-disorder temperature compared to manganese. The order-disorder temperature for Ni$_2$MnAl is approximately 500 °C, which is lower than Ni$_2$MnIn ~ 800 °C.

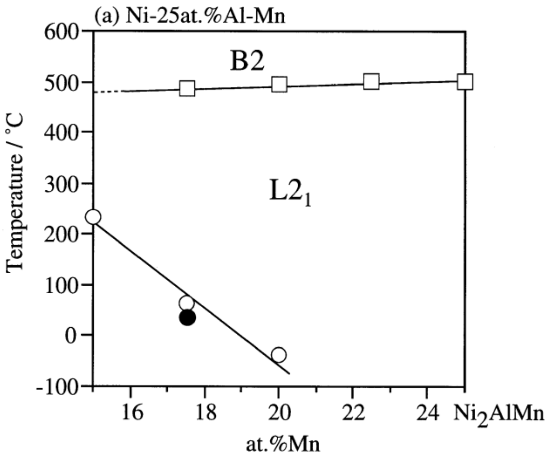

Figure 1.16 Order-disorder (T°) and martensite start temperatures (M_s) of (a) Ni-25 at% Al-Mn and (b) Ni-Al-25 at% Mn alloys [113].

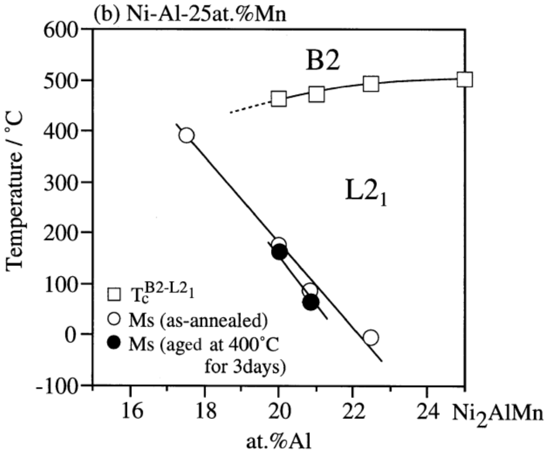

Figure 1.16 continued

1.6.3 Magnetic field induced phase transformation

A magnetic field induced transformation has recently been reported in bulk NiCoMnAl alloys, where the transformation temperatures were reduced by the applied magnetic field at a rate up to 3.6 K/T (see Figure 1.17) [31]. The underlying mechanism for this drastic change of phase transformation temperature is due to the partial substitution of Co for Ni in the Mn-rich NiMnAl alloy. The nearest neighbor distance between Mn atoms in a Mn-rich NiMnAl alloy is below a critical value for a ferromagnetic parent phase. The addition of Co modifies the exchange interaction between the Mn atoms to reverse the magnetic order of the parent phase from antiferromagnetic to ferromagnetic, and the saturation magnetization in NiCoMnAl martensite decreases[31].

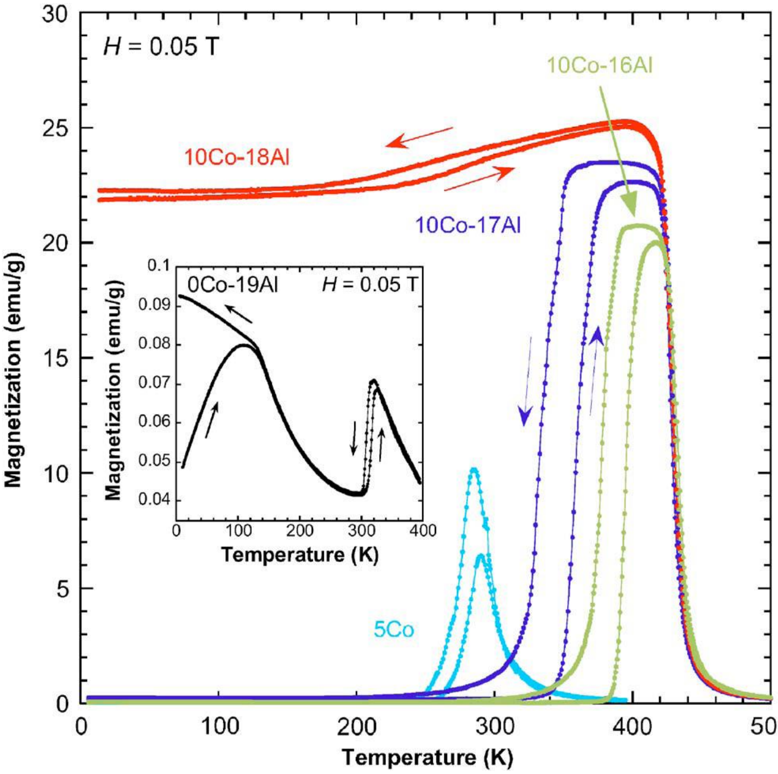

Figure 1.17 Thermomagnetization curves for various NiCoMnAl alloys in a magnetic field of 0.05 T. Thermomagnetization curve of NiMnAl alloy is shown in the inset [31].

1.7 Objectives

The objectives for this dissertation are two-fold. One objective of this research is to explore the impact of microstructure on the physical properties of magnetic shape memory alloy (MSMA) thin films for MEMS applications. This includes decoupling the effect of grain size and film thickness on the residual stress in thin films. The second objective of this work is to explore the feasibility of magnetic shape memory alloy thin films for MEMS devices for actuator applications. That is, can small magnetic fields be used to produce MFIPT in MSMA thin films?

By answering these questions, we can establish a design criterion for MSMAs and determine feasibility for MEMS applications. Additionally, we can develop a process to successfully transfer MSMA thin-film results to bulk alloys, which allows for a systematic approach to explore alloy compositions for structural transitions.

2. EXPERIMENTAL METHODS

2.1 Thin film fabrication via magnetron sputtering

Thin films were fabricated using a custom-built magnetron sputtering system operated by the Zhang and Nanolayer Group at Texas A&M University. The sputtering system is equipped with four circular high-vacuum magnetron sputtering sources powered by DC and/or RF power supplies, which allowed for the synthesis of films with varied compositions using a co-sputtering technique. The composition of the co-sputtered films was controlled by varying the deposition power of the respective targets and substrate to source distance. Prior to deposition the deposition chamber was pumped to a base pressure of ~ 5×10^{-8} Torr using a combination of turbomolecular and cryopumps. Ultra-high purity (UHP) argon gas was used to sputter the target material onto unheated substrates; deposition pressures were ~3×10^{-3} Torr.

2.2 X-ray diffraction (XRD)

XRD is a nondestructive technique commonly used to characterize the thin film microstructure. In the XRD experiment, the lattice spacing of the film acts as a diffraction grating for the incident x-rays. The x-rays are diffracted when Bragg's law is satisfied.

$$n\lambda = 2d \sin\theta \qquad \text{Equation 2.1}$$

where n is an integer that represents the order of the diffracted peak, λ is the wavelength of the incident beam, d is the interplanar spacing, and θ is the angle between the incident x-ray and the diffracted atomic plane.

In this work, powder XRD was performed at the Texas A&M Department of Chemistry X-ray Diffraction Laboratory. A Bruker-AXS D8 Bragg-Brentano X-ray Diffractometer, using Cu-Kα source (λ = 1.54 Å), was used to collect θ-2θ scans from deposited films. Additional XRD was collected from Dr. Haiyan Wang's Thin Film Laboratory located at Texas A&M Department of Electrical Engineering. The PANalytical X'Pert PRO Materials Research Diffractometer, also operated using Cu-Kα radiation allowed for specialized XRD measurements such as in-plane phi scans for residual stress measurements.

2.3 Differential scanning calorimetry (DSC)

Thermal measurements of films with sufficient mass (~5 mg) were measured using a differential scanning calorimeter (DSC) located at Texas A&M Department of Mechanical Engineering in Dr. Xinghang Zhang's laboratory. DSC measures the difference in heat flow between a sample and an inert reference as a function of time and temperature. Heat can flow either into the sample or out of the sample. Endothermic heat flow refers to heat flow into the sample as a result of endothermic processes, such as melting, evaporation, or a glass transition temperature. Exothermic heat flow refers to heat flow out of the sample as a result of an exothermic reaction, such as crystallization, oxidation, or curing [114, 115]. In general, the change in heat flow is due to a change in the sample heat capacity, which results in either an exothermic or endothermic process.

Figure 2.1 illustrates a schematic of a DSC sensor assembly. The sensor assembly consists of a sample and reference platforms. The sample is sealed in a small aluminum or copper pan enclosure using a crimping tool. The choice of metal depends on the maximum operating temperature. Copper and aluminum pans are used for temperatures up to 725 and 600 °C, respectively. The difference in heat flow is measured between the sample enclosed in a metal pan, which is placed on the sample platform, and the reference sample consists of an empty metal pan with similar weight of the sample pan is placed on the reference platform.

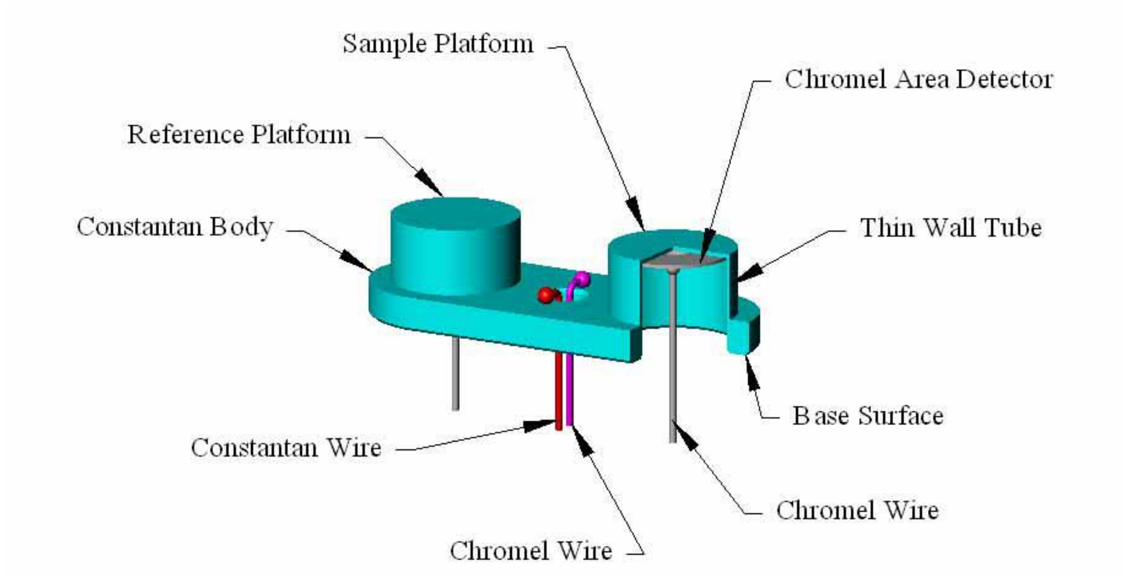

Figure 2.1 Differential scanning calorimeter sensor assembly [116].

A simple equation is used to describe the heat flow signal, $\frac{dQ}{dt}$, in a DSC is provided below.

$$\frac{dQ}{dt} = C_p \frac{dT}{dt} + f(T,t) \qquad \text{Equation 11}$$

The first component of the heat flow equation shows that the heat flow is a function of the sample heat capacity, C_p, and the heating rate, $\frac{dT}{dt}$, while the second part is a function of time and temperature, which represents the kinetic heat flow. The kinetic contribution of the heat flow equation is related time-dependent prrocesses such as glass transition temperatures or crystallization of a polymer from the melt or an amorphous metal.

Equation 2.2 shows how the heat flow increases linearly with the heating rate due to the heat capacity of the sample. For instance, if the heating rate is doubled from 20 to 40 °C/min, the heat flow doubles. Therefore, the heating rate dependence of the heat flow suggestst that a high heating rates should be used when trying to measure small transitions. Additionally, when the kinetic component is absent or negligible, DSC can be used to estimate the heat capcity using Equation 2.3.

$$C_p = \frac{dQ/dt}{dT/dt} \qquad \text{Equation 12}$$

The effective crystallization activation energy can be calculated by the Kissinger method.

$$\ln\left(\frac{T_p^2}{\beta}\right) = \left(\frac{E_a}{RT}\right) - C \qquad \text{Equation 13}$$

where β is the heating rate, E_a is the effective activation energy for crystallization, R is the universal gas constant, and C is a constant. From Equation 2.4, the effective crystallization activation energy E_a can be determined by plotting $\ln(T_p^2/\beta)$ vs. $1/T_p$.

2.4 Magnetization measurements

The thin film magnetic properties were measured as a function of temperature and magnetic field using a superconductor magnetometer located at Texas A&M Department of Electrical Engineering in Dr. Haiyan Wang's Thin film Laboratory. The magnetization of a ferromagnet depends on the magnitude of the applied field and the sample temperature. Therefore measuring, how the magnetization varies as a function of temperature is a good way to measure a phase transformation for a MSMA. Figure 2.2 is a schematic of a superconducting magnetometer used to measure the magnetization of a sample as a function of temperature and magnetic field.

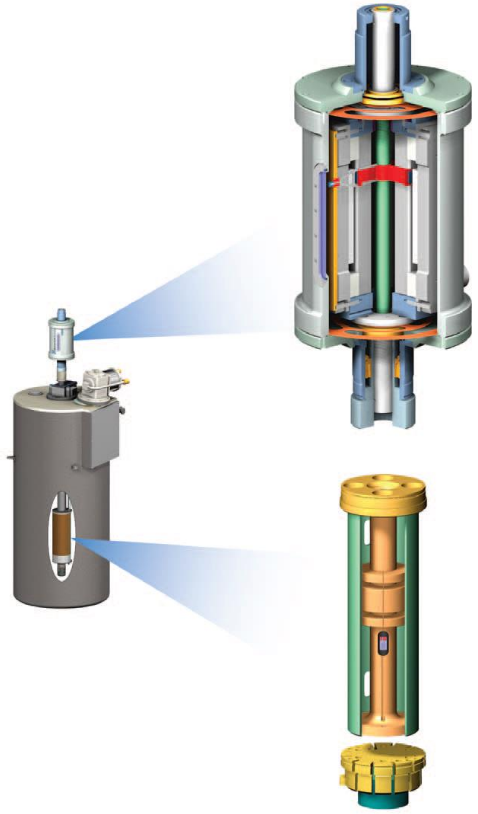

Figure 2.2 An illustrated schematic of Quantum Design's Physical Property Measurement System (PPMS) equipped with a vibrating sample magnetometer module [117].

A vibrating sample magnetometer oscillates a sample through a magnetic field in between a detection (pick up) coil. The operating principle is based on Faraday's law, which states that a change in magnetic flux through a conducting wire induces an electromagnetic field (emf) to oppose the change in flux. This can be expressed with the following expression.

$$V_{coil} = -n\frac{d(BA)}{dz}\frac{dz}{dt} \qquad \text{Equation 14}$$

where V_{coil} is the induced emf, n is the number of turns in the coil, A is the cross-sectional area of the detection coil, B is the magnetic field, and z is the vertical height of the sample with respect to the coil. The detection coil remains fixed in a constant magnetic field, where the magnetic induction is $B = \mu_0 H$. When the a magnetic sample is placed into the coil, the magnetic induction increases, $B = \mu_0(H + M)$. Therefore the change in flux with the sample in and out of the coil is

$$\Delta B \sim \mu_0 M \qquad \text{Equation 15}$$

For an oscillating sample, the induced emf from the magnetic sample can be expressed with the following expression

$$V_{coil} \sim fmA \qquad \text{Equation 16}$$

where f is the frequency of the oscillation, $m=M*V_{sample}$ is the magnetic moment of the sample, and A is the amplitude of the oscillation. The above discussion and equations describe the basic operational for a VSM. The VSM can be used with a regular electromagnet or placed in a super conducting quantum interference device (SQUID). From Equation 2.7 we see that the induced emf is proportional to the sample size, since $m = MV$. Therefore, measuring the magnetization of thin films becomes challenging with a traditional detection coil between electromagnets. Increased sensitivity requires the use of a superconducting quantum interference device (SQUID), to measure samples with magnetizations too small to detect in a traditional detector coil made from copper. Additionally, for similar reasons, the use of the SQUID sensitivity allows the measurement phase transformations that are too small to detect in a DSC.

3. CRYSTALLIZATION AND HIGH TEMPERATURE SHAPE MEMORY BEHAVIOR OF SPUTTER-DEPOSITED NIMNCOIN THIN FILMS[*]

3.1 Overview

Amorphous $Ni_{50}Mn_{38}Co_6In_6$ films of 20 μm in thickness are fabricated using DC magnetron sputtering technique. Ex-situ annealing studies demonstrate the crystallization at elevated temperature, and the retention of $L1_0$ martensite at room temperature. In-situ annealing inside a transmission electron microscope reveal the crystallization process as well as the transformation to B2 austenite at elevated temperatures. Differential scanning calorimetry studies show the crystallization activation energy of ~ 239 kJ/mol, a reversible martensitic phase transformation temperature of ~ 350 °C, and a hysteresis of ~ 75 °C.

3.2 Introduction

A magnetic field can induce shape memory effect in magnetic shape memory alloys (MSMAs), such as NiMnGa alloys [18, 20] by a field-induced rearrangement of martensite variants [18] or by controlling the forward and reverse martensitic transformation with a magnetic field [4, 33, 118, 119]. MSMAs are compelling candidates compared to other smart materials, because they offer the promise of conventional shape memory alloys

---

[*] This chapter reprinted with permission from "Crystallization and high temperature shape memory behavior of sputter-deposited NiMnCoIn thin films" by S. Rios, I. Karaman, and X. Zhang, 2010. *Applied Physics Letters*, Volume 96, 173102 by AIP Publishing

(SMAs), such as high strain, and in addition, a much shorter response time dictated by an applied magnetic field.

In parallel, high temperature bulk SMAs are also developed for a variety of technological applications in the aircraft, automotive, and oil industries [62, 120]. In conventional SMAs with martensitic phase transformation close to room temperature, the rate limiting step for the phase transformation is cooling rate. In high temperature SMAs, a much higher phase transformation temperature indicates that a much faster cooling rate, and consequently a shorter response time can be achieved. Compared to NiTiX (X = Pd, Pt, Au) [61], bulk NiMnGa with certain compositions, and other ferromagnetic SMAs, such as CoNiGa [121], are economical alternatives that demonstrate high temperature shape memory effect. Besides NiMnGa, Kainuma *et al.* have recently reported that the $Ni_{45}Co_5Mn_{36.6}In_{13.4}$ alloy exhibited a martensitic transition from the ferromagnetic austenite phase to the paramagnetic or antiferromagnetic martensite phase [34]. Near perfect strain recovery induced by magnetic field was reported. Magnetic field induced phase transformation has also been observed in NiCoMnIn ribbons prepared by rapid solidification [37]. Although magnetron sputtering has been used to fabricate NiTiPd and NiMnGa thin films, there has been no work reported in literature regarding the preparation of NiCoMnIn thin films by sputtering. Compared to rapid solidification, magnetron sputtering has the advantages of precise control of film thickness with sub-nanometer precision, low surface roughness, and integration of films for device applications. In this work, we report high temperature, reversible shape memory effect in $Ni_{50}Mn_{38}Co_6In_6$ films fabricated by magnetron sputtering. The crystallization behavior of sputtered amorphous films and the evolution of microstructures are investigated by ex-situ studies as well as in-situ TEM annealing studies.

3.3 Experimental

$Ni_{50}Mn_{38}Co_6In_6$ films, ~ 20 μm in thickness, were deposited on unheated SiO_2 substrates using DC magnetron sputtering. Sputtering was performed with a base pressure of < 2 × 10^{-7} Torr and an argon pressure of ~ 4 mTorr. Freestanding films were obtained by peeling the deposited film from the substrate. Three sets of freestanding films were annealed ex-situ in a high vacuum furnace (5 - 20× 10^{-8} Torr) for one hour at 400, 600, and 900 °C, respectively. The crystal structure of the films was analyzed at room temperature using a Bruker-AXS D8 x-ray diffractometer (XRD) with Cu K_α radiation. In-situ annealing of an as-deposited film up to 600 °C, at an average heating rate of 3 ^{o}C/min, was performed in a JEOL 2010 transmission electron microscope (TEM) operated at 200 kV. Temperatures were kept constant for 5 minutes to reduce thermal drift before recording micrographs. The crystallization and martensitic transformation temperatures were determined using a TA Q1000 differential scanning calorimeter (DSC).

3.4 Results and discussion

Room temperature XRD spectra of ex-situ annealed films are illustrated in Figure 3.1. The small diffraction peaks superimposed onto the broad peak of the as-deposited films indicate the presence of certain crystallinity in an amorphous matrix. Crystallization is clearly detected in the films annealed at 400 °C.

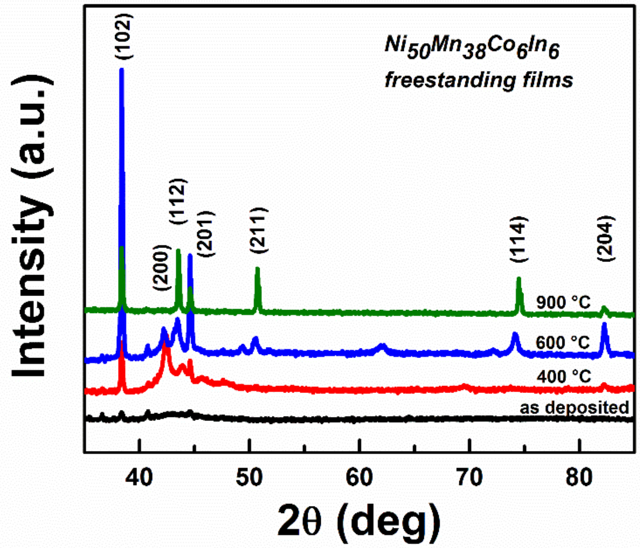

Figure 3.1 Room temperature XRD spectra of free standing $Ni_{50}Mn_{38}Co_6In_6$ films in the as-deposited amorphous state and annealed for one hour. Annealed films have a tetragonal $L1_0$ structure.

To reveal the microstructures of ex-situ annealed films in detail, TEM experiments were performed. Figure 3.2 (a) shows that significant crystallization occurs after annealing at 400 °C, and the average grain size is ~ 100 nm. The continuous diffraction ring in the inserted selected area diffraction (SAD) pattern indicates the existence of nanocrystals.

After annealing at 600 ^{o}C, the average grain size increases to ~ 150 nm (Figure 3.2 (b)). The crystal structure was determined to be a tetragonal $L1_o$ structure with a = b = 4.28 Å and c = 5.69 Å. It has been reported that NiMnIn alloys are martensitic at room temperature with indium concentrations less than 15 at.% and that the martensite has a nonmodulated tetragonal $L1_o$ structure when the indium concentration is 5 at.% [37].

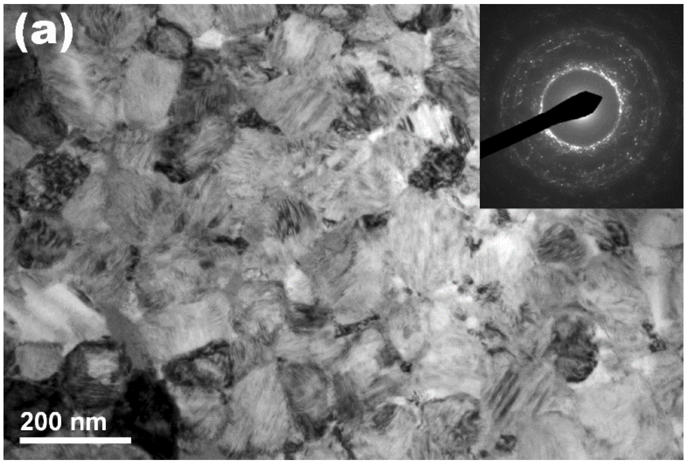

Figure 3.2 Freestanding $Ni_{50}Mn_{38}Co_6In_6$ films annealed in a high-vacuum furnace for one hour at (a) 400 °C with an average grain size of ~ 100 nm, and (b) at 600 °C with an average grain size of ~ 150 nm.

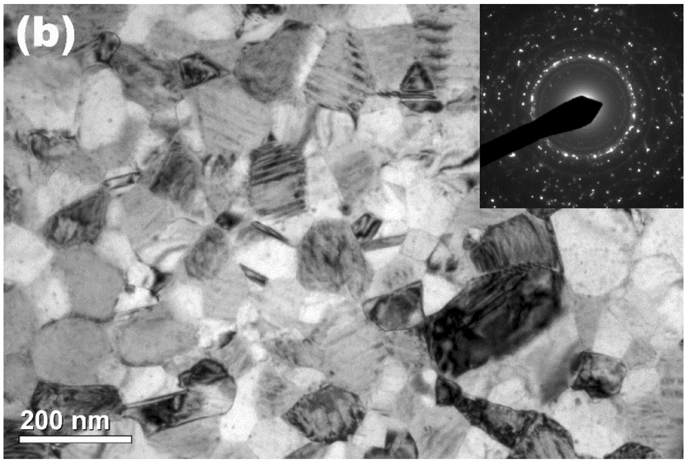

Figure 3.2 continued

A series of TEM images and corresponding SAD patterns of an in-situ annealed film are displayed in Figure 3.3. The as-deposited film is featureless as shown in Figure 3.3 (a), and the diffuse ring in the SAD pattern indicates the amorphous nature of the film. After annealing at 350 °C, nuclei indicated by nanoscale areas of dark contrast emerge from the amorphous matrix in Figure 3.3 (b), depicting an initial stage of the crystallization process. Upon further heating to 400 °C, a mixture of nucleation and grain growth processes is identified by nuclei, 1-3 nm in diameter, coexisting with coarse nanocrystals, 5-20 nm in diameter, as indicated by arrows in Figure 3.3 (c). At 600 °C, considerable grain growth occurs where the majority of grains remain less than 100 nm (Figure 3.3 (d)). The distinct diffraction pattern of the large grains in Figure 3.3 (d) is identified to be the B2 crystal structure, which is the structure of a high-temperature austenite phase. From the SAD pattern, the lattice parameter was calculated as a = 6.81 Å at 600 °C. The differences in the microstructures found during the 600 °C ex-situ and in-situ anneals may be explained by the difference in annealing duration. The ex-situ annealing was performed for 60 minutes as opposed to 15 minutes for the in-situ annealing. Hence, during the in-situ annealing it is likely that the grain growth had not progressed as much as was seen in the ex-situ annealed specimen.

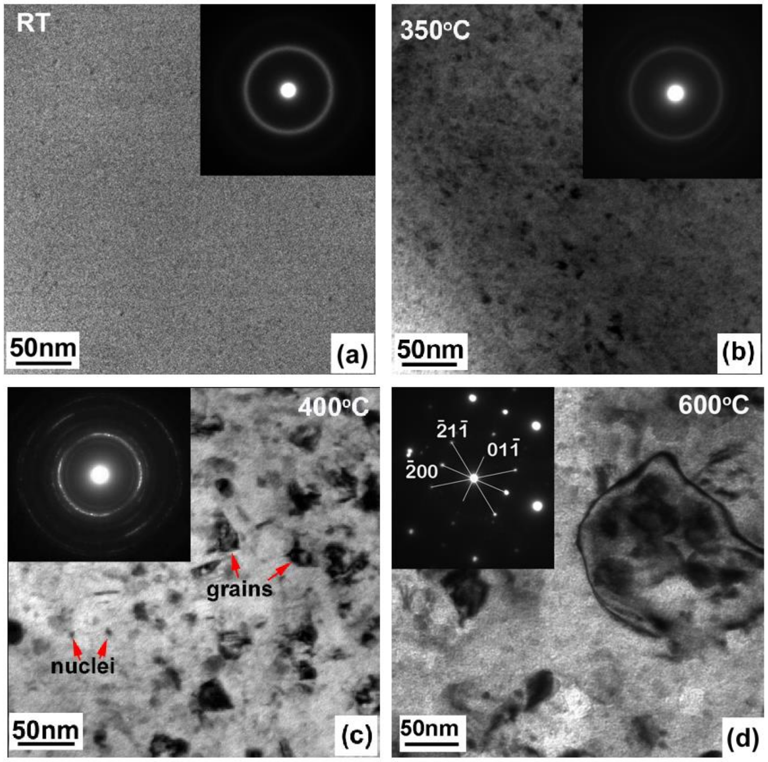

Figure 3.3 Bright-field TEM images and selected area diffraction (SAD) patterns of the in-situ crystallization process: (a) amorphous film at room temperature, (b) initial crystallization of nanocrystals detected at 300 °C, (c) significant crystallization at 400 °C, and (d) the confirmation of austensite phase at 600 °C.

Figure 3.4 (a) is a typical DSC curve obtained from the as-deposited $Ni_{50}Mn_{38}Co_{6}In_{6}$ free-standing film at a constant heating - cooling rate of 80 ^{o}C/min for two cycles. Initial heating (segment 1) results in an exothermic peak at a peak temperature,

T_p, of 450 °C, corresponding to the crystallization of the amorphous structure. When cooling the sample from 500 to 40 °C (segment 2), the austenite to martensite transformation starts at M_s = 350 °C and finishes at M_f = 319 °C. Heating the same specimen for a second time, the transformation from martensite to austenite begins at A_s = 388 °C and ends at A_f = 429 °C. Figure 3.4 (b) represents a series of isochronal DSC experiments used to determine the crystallization activation energy. Based on values of T_p, the effective crystallization activation energy was calculated by the Kissinger method using, $\ln\left(\frac{T_p^2}{\beta}\right) = \left(\frac{E_a}{RT}\right) - C$, where β is the heating rate, E_a is the effective activation energy for crystallization, R is the universal gas constant, and C is a constant. A Kissinger plot of $\ln(T_p^2/\beta)$ vs. $1/T_p$ is shown as an inset in Figure 3.4 (b). The effective crystallization activation energy E_a was determined to be 239 ± 19 kJ/mol.

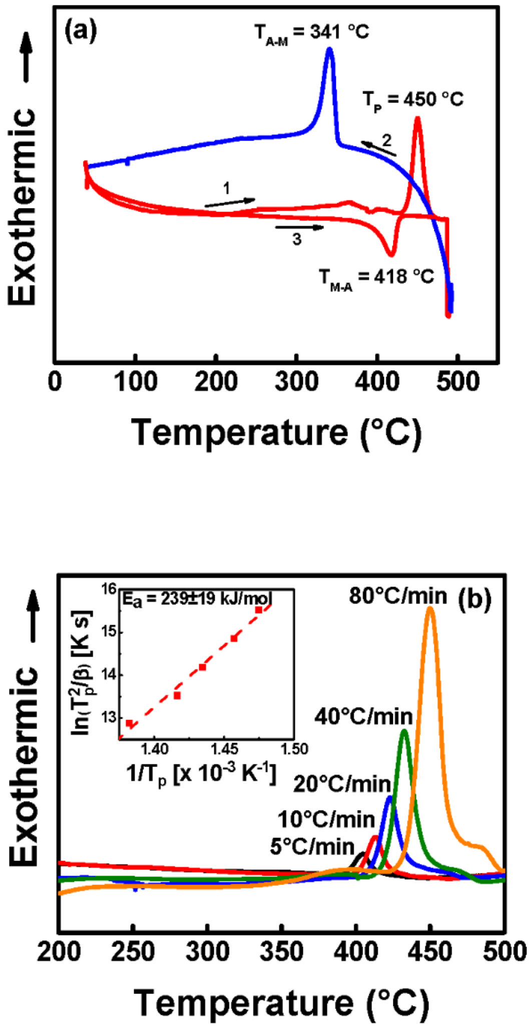

Figure 3.4 (a) DSC curve of an as-deposited amorphous freestanding film. The film was (1) heated, (2) cooled, and (3) reheated at a heating (cooling) rate of 80 °C/min. (b) isochronal DSC curves of the crystallization process in freestanding films heated linearly at different rates. The inserted Kissinger plot for the nanocrystallization process determined using the DSC data from Figure 3.4 (b) yields the effective activation energy for crystallization of 239 ± 19 kJ/mol.

The current study shows that NiCoMnIn films deposited at room temperature are predominantly amorphous, similar to the deposition of amorphous NiTi [122] and NiMnGa films [123] onto unheated substrates. Once crystallized, the films possess a $L1_0$

martensitic phase at room temperature, whereas the austenite phase shows a B2 structure at higher temperatures as evidenced by the in-situ TEM annealing studies. In bulk NiMnIn alloys, it has been shown that the austenitic phase could have $L2_1$ or B2 structures, where the latter is typically a result of lower In concentration [37].

The crystallized $Ni_{50}Mn_{38}Co_6In_6$ films possess a thermally induced reversible phase transformation at M_s temperature of 350 °C. Bulk NiMnIn alloys that have an indium concentration of 5 at.% were shown to have a M_s temperature of 487 °C [37]. Furthermore, the replacement of Ni by a concentration of Co greater than 3 at.% tends to decrease the M_s temperature of the NiMnIn alloys [37]. Ito *et al.* reported on the dependence of the M_s temperature for indium and cobalt concentrations ranging from 10-25 at.% and 0-7.5 at.%, respectively [29]. From their data of M_s vs. e/a ratio, we can infer an M_s temperature of ~ 327 ° C for a $Ni_{44}Mn_{44}Co_6In_6$ alloy (e/a = 8.2), comparable to our experimental observations of ~ 350°C for $Ni_{50}Mn_{38}Co_6In_6$ alloy films (e/a = 8.4). The phase transformation entropy, ΔS, is calculated by using $\Delta S = \Delta H/T_0$, where ΔH is the latent heat during phase transformation measured by DSC, T_0 is the transformation temperature where the parent phase has the same Gibbs energy as that of the martensite phase. In the current study, the T_0 was approximated as $(A_f + M_s)/2$ and the ΔS value is calculated to be ~ 67 J/kg•K. It has been shown that in the $Ni_{45}Mn_{50-y}Co_5In_y$ alloy, a lower indium concentration leads to a higher entropy change, ~ 68 J/kg•K for $Ni_{45}Mn_{40}Co_5In_{10}$ [29].

In the DSC studies, a broad peak after the primary crystallization peak was observed for samples heated at rates greater than 10 °C/min. This reaction sequence has been observed in the crystallization of amorphous alloys and is attributed to the formation of a eutectic reaction of the primary crystallization phase [124]. The crystallization temperature T_p and effective activation energy E_a for the $Ni_{50}Mn_{38}Co_6In_6$ alloy are comparable to near stoichiometric Ni_2MnGa ($T_p = 427$ °C, and $E_a = 234$ kJ/mol), but are much less than NiTi shape memory alloys ($T_p = 511$ °C and $E_a = 416$ kJ/mol) [125]. Lower E_a values for Ni_2MnGa and NiCoMnIn alloys may be due to a combination of the partial crystallization in the as-deposited films and the stronger interactions of the Ni-Ti constituent atoms versus the Ni-X (X = Ga, Mn, Co, In) constituent atoms [125, 126].

3.5 Summary

In summary, we have fabricated amorphous $Ni_{50}Mn_{38}Co_6In_6$ films by magnetron sputtering technique, and determined the effective crystallization kinetics and phase transformation temperatures in as-deposited amorphous films. The current films show phase transformations and reversible shape memory effect at high temperatures.

4. MAGNETIC FIELD INDUCED PHASE TRANSFORMATION IN POLYCRYSTALLINE NICOMNAL THIN FILMS*

4.1 Overview

NiCoMnAl thin films were deposited onto unheated substrates using dc magnetron co-sputtering. The microstructure of as-deposited films consisted of nanocrystals in an amorphous matrix and did not exhibit a martensitic phase transformation. After heat treatment, films crystallized into a B2 austenite phase, which exhibited a magnetic field induced martensitic phase transformation. The level of the change in the martensitic transformation temperatures in the magnetic field was determined to be ~ 2.1 K/Tesla. The films exhibited non-reversible magnetic field induced martensite to austenite transformation due to the large thermal hysteresis.

4.2 Introduction

Significant steps forward have been achieved in magnetic shape memory alloys (MSMAs) to obtain large actuation strains up to 10% under a magnetic field [4, 19, 20, 97] since the discovery of a large magnetic field induced strain (MFIS) in Ni_2MnGa [18]. The origin of the large MFIS in Ni_2MnGa is the rearrangement of martensitic variants by

---

* This chapter reprinted with permission from "Magnetic field induced phase transformation in polycrystalline NiCoMnAl thin films" by S. Rios, D. Bufford, I. Karaman, and X. Zhang, 2013. *Applied Physics Letters*, Volume 103, 132404 by AIP Publishing

an applied magnetic field, where the driving force is related to the magnetocrystalline anisotropy energy (MAE) of the martensite phase. Since the MAE is limited by the saturation magnetization of the martensite phase, the output stress that can be obtained from an applied magnetic field is often limited to a few MPa. MSMAs can also demonstrate large MFIS by magnetic field-induced phase transformation (FIPT).

The driving force for FIPT is the difference between the saturation magnetization of the parent and martensite phases. A family of MSMAs called metamagnetic shape memory alloys based on NiCoMnX (X = Al, In, Sb, and Sn) exhibit FIPT [25-33] In NiCoMnIn system, thermomagnetization studies show that under magnetic field up to 7 Tesla (7T), phase transformation temperature can decrease by as much as 30 K ($Ni_{45}Co_5Mn_{36.6}In_{13.4}$) [34]. Furthermore, near pseudo elasticity and 3% MFIS of field-induced strain were achieved in $Ni_{45}Co_5Mn_{36.5}In_{13.5}$ system under stress levels as high as 125 MPa [32].

The large field induced strain and associated mechanical work in NiCoMnIn system is attributed to the difference in saturation magnetization of parent and martensite phases: the austenite phase is ferromagnetic, whereas the martensite is antiferromagnetic or paramagnetic. Thus, the existence of a large Zeeman energy leads to substantial FIPT. Meanwhile, studies on NiCoMnIn thin films remain scarce. We reported temperature induced phase transformation in NiCoMnIn polycrystalline films[42]. Niemann *et al.* reported later that epitaxial NiCoMnIn films show FIPT [30].

Recently, NiCoMnAl has been identified as a metamagnetic shape memory alloy after replacing expensive indium with inexpensive aluminum [31]. In contrast to the brittle

NiCoMnIn alloys, the grain boundaries of NiCoMnAl alloys have relatively high strength and even polycrystalline alloys can be deformed under compression, indicating enhanced deformability [26, 54]. FIPT has recently been reported in bulk NiCoMnAl alloys, where the transformation temperatures were reduced by the applied magnetic field at a rate up to 3.6 K/T [31]. The underlying mechanism for this drastic change of phase transformation temperature is due to the partial substitution of Co for Ni in the Mn-rich NiMnAl alloy. The nearest neighbor distance between Mn atoms in a Mn-rich NiMnAl alloy is below a critical value for a ferromagnetic parent phase. The addition of Co modifies the exchange interaction between the Mn atoms to reverse the magnetic order of the parent phase from antiferromagnetic to ferromagnetic, and the saturation magnetization in NiCoMnAl martensite decreases[31].

Although the multifunctional properties of bulk NiCoMnAl alloys have been presented [26, 31, 54], no work has been reported in the literature on the preparation and properties of NiCoMnAl thin films. Motivated by the recent studies on bulk NiCoMnAl alloys, we report the FIPT effect in polycrystalline Ni-Co-Mn-Al thin films. While bulk MSMAs can be used for structural components, in many cases MSMA thin films are preferred for device applications, such as miniaturized actuators and micro-electro-mechanical systems (MEMS). There are extensive studies on NiMnGa films in the past few years [127-131]. However studies on NiCoMnAl films do not exist. The challenge lies in delicate control of film compositions, precipitation, microstructure, residual stress and mechanical properties. Understanding these issues is crucial for the application of NiCoMnAl based MSMA thin films for device applications. Under this context, we performed the first investigation on microstructure and field induced phase transformations in NiCoMnAl films.

The current paper seeks to understand the synthesis and microstructure of NiCoMnAl alloy thin films, and field induced phase transformation. This study will form the basis for tuning functional properties for thin film actuator devices. The large field induced variation of phase transformation temperature exceeds 2 K/T, in comparison to ~ 1.5 K/T in epitaxial NiCoMnIn films [30].

4.3 Experimental

A 500 nm thick $Ni_{45}Co_7Mn_{28}Al_{20}$ alloy film was deposited onto unheated SiO_2 substrates co-sputtering Co and Ni-Mn-Al alloy targets with 99.95% purity. In order to ensure homogeneity in film thickness and chemical composition, both sputter sources were inclined towards the center of the rotating substrate. The base pressure prior to the deposition and argon pressure during deposition were 5×10^{-8} Torr and 3.5 mTorr, respectively. As-deposited films were annealed from room temperature to 973 K at a rate of 20 K/min in ultra-high purity nitrogen (99.999 %) environment. The structures of the as-deposited and annealed films were analyzed at room temperature using x-ray diffraction (XRD, Bruker AXS-D8 with Cu K_α radiation). Transmission electron microscopy (TEM) and nanobeam diffraction experiments were conducted with a JEOL 2010 microscope operated at 200 kV, and images were recorded using a Gatan SC1000 ORIUS CCD camera. The chemical compositions of the as-deposited films were determined using electron probe microanalysis (EPMA, Cameca SX50 electron microprobe, 20 kV, 10 nA). The magnetic properties of the annealed films were measured using a physical properties measurement system (Quantum Design) with a vibrating sample magnetometer module.

4.4 Results and discussion

Room temperature XRD was used to determine the crystal structure of the as-deposited and annealed films. The broad diffraction peak in Figure 4.1 indicates that microstructure of the as-deposited film is a mixture of nanocrystalline grains embedded in an amorphous matrix. The main diffraction peak in the spectrum for the annealed film (973 K followed by isothermal annealing at 623K/1h) can be identified as the (110) plane of the B2 structure for the parent phase with a calculated lattice parameter, a = 2.88 Å. A small unidentifiable peak was also observed and may be related to the atomic disorder between the constituent atoms that leads to a mixture of A2 and B2 structures in the annealed film.

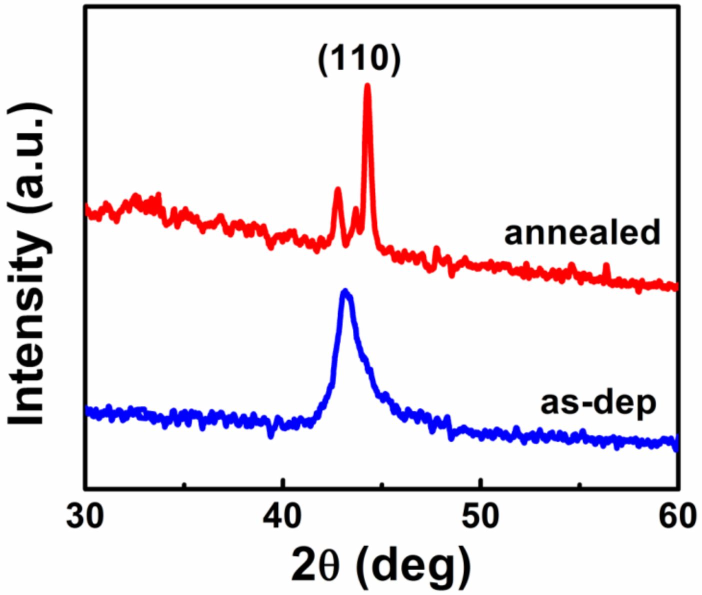

Figure 4.1 XRD profiles for as-deposited and annealed films. Annealing leads to the formation of B2 austenite phase with (110) texture.

TEM experiments were performed to study the microstructure of both the as-deposited and annealed films. The as-deposited film showed grain sizes of approximately a few tens of nanometers, as seen in Figure 4.2 (a). The inset selected area diffraction (SAD) pattern confirms the nanocrystalline nature of the film. The center of the first order ring labeled in the figure corresponds to a d-spacing of 2.07 Å, consistent with the broad peak seen in the XRD spectrum. After annealing at 973 K, a bimodal microstructure was obtained. Some grains reached sizes of several hundred nm, as seen in Figure 4.2 (b). However, the film was not fully recrystallized, and numerous smaller grains with sizes of ~ 50 nm could still be found. The inset SAD pattern shows dotted diffraction rings, implying that the annealed film is polycrystalline with much larger grains than those in the as-deposited case. The first (inner) diffraction ring was indexed to be (110) of B2 austenite. Some larger grains showed an apparent layered or marbled structure (Figure 4.2 (b)).

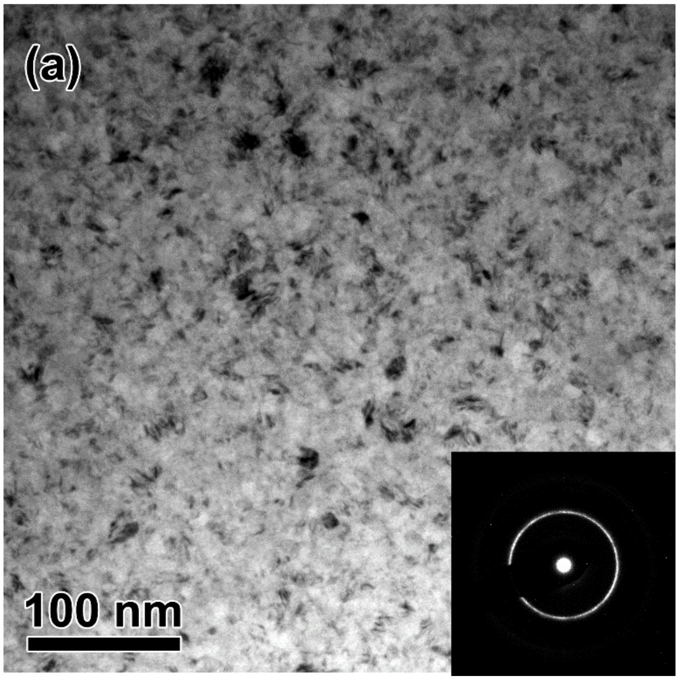

Figure 4.2 (a) As-deposited films have grain size of ~10 nm. The inset SAD pattern of the same area collected with a large (1 μm) aperture confirms the nanocrystalline structure. (b) After annealing for 1 hour at 973 K, the film shows significant recrystallization. The formation of austenite phase is identified. (c) Higher magnification of austenite grains with some stacking faults. The inset SAD pattern obtained from nanobeam diffraction (NBD) on the labeled grain shows austenite phase examined along <100> diffraction zone.

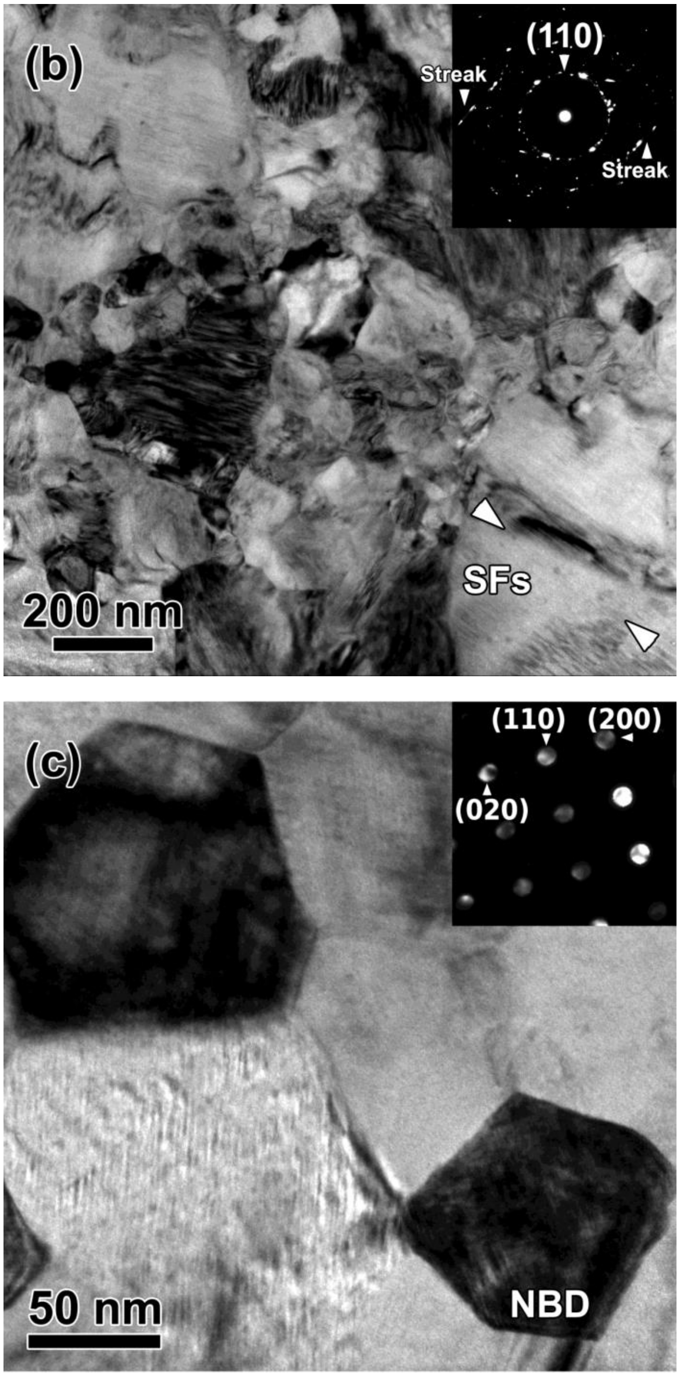

Figure 4.2 continued

Thermomagnetization (in unit of emu/cm^3 (emu/cc)) measurement was performed for the annealed films. Neither ferromagnetic behavior nor a martensitic phase transformation was observed in as-deposited films. Figure 4.3 (a) shows a series of thermomagnetization (MT) curves for heating and cooling cycles from 20 to 400 K obtained in magnetic fields of 0.05, 1, 5, and 9 T for annealed films. In a 50 mT magnetic field, the magnetization began to increase rapidly upon cooling below the Curie temperature (T_C) of the film, 290 K, and reached a maximum at approximately 230 K. Upon further cooling the magnetization decreased until it reached a constant value, ~ 120 emu/cc, at approximately 90 K. When the sample was reheated to 400K, a smaller maximum magnetization was reached at a slightly higher temperature of 258 K followed by the enclosure of the thermomagnetization hysteresis loop. Similar hysteresis loops were observed when the measurements were repeated in magnetic fields of 1, 5, and 9 T. The magnetization reached a maximum value of 520 emu/cc at 9T. The square symbols on the cooling curves represent the inflection point (the peak temperature of the first order derivative plot of the thermomagnetization curve) of the cooling curves as a means to measure and compare the martensitic phase transformation temperature T_M to other alloy systems.

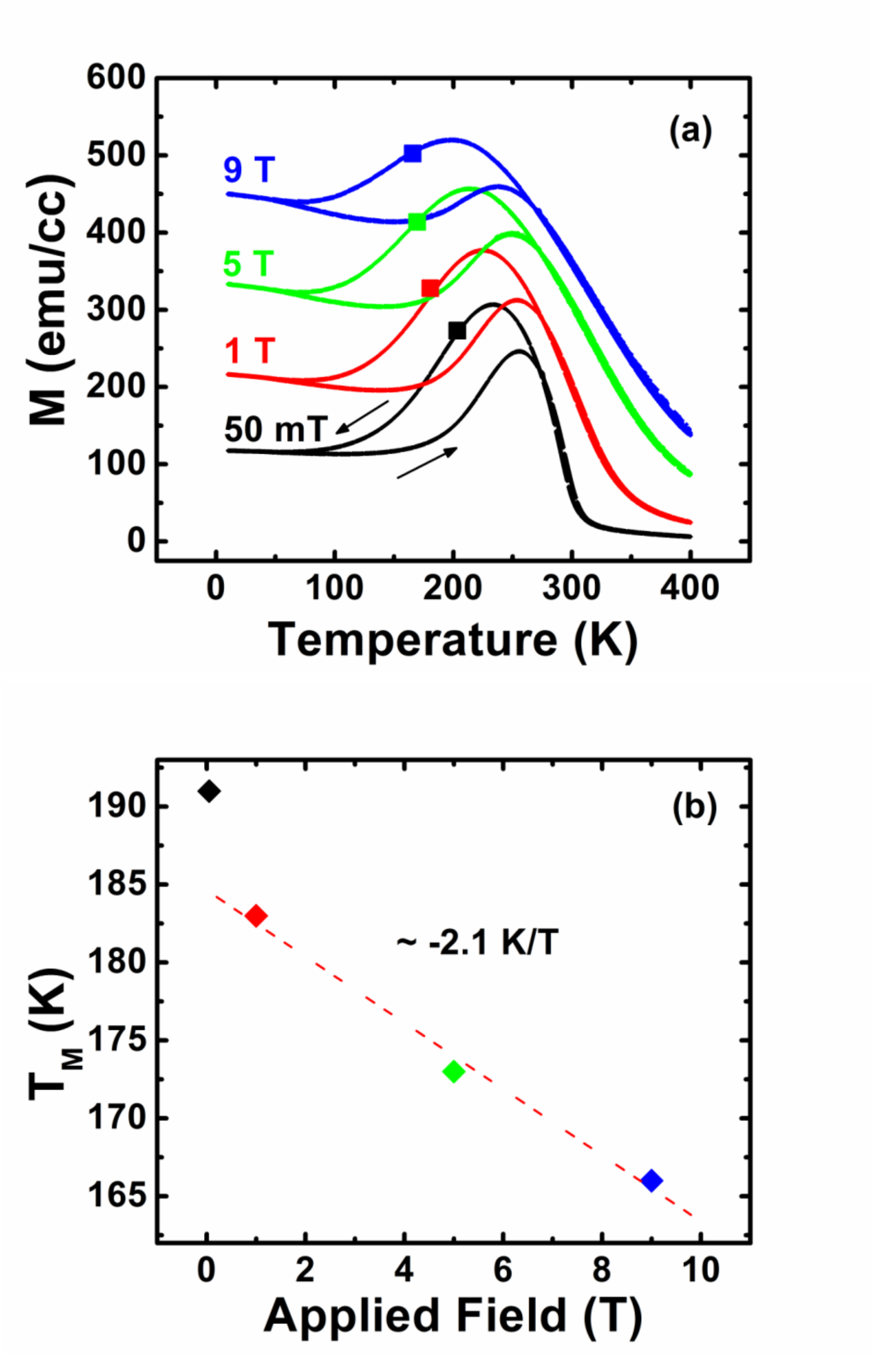

Figure 4.3 (a) Thermomagnetization curves of Ni45Co7Mn28Al20 film in magnetic fields varying from 0.05 to 9 T applied to the surface of the film in plane. The square symbols on the cooling curves represent the inflection point during cooling and has been chosen at the martensite formation temperature TM to compare with similar work found in literature [151]. (b) The martensite temperature as a function of applied field summarized from (a). The slope of the fitted line is ~ 2.1 K per Tesla.

Figure 4.3 (b) represents a summary of the martensitic phase transformation temperatures collected from Figure 4.3 (a). The martensitic phase transformation temperature decreased linearly as the applied magnetic field increased above 1 T. The slope of the graph is related to the Clausius-Clapeyron equation,

$$dT_M/dH = -\Delta M/\Delta S \qquad \text{Equation 4.1}$$

where ΔM and ΔS are the change in magnetization and entropy between the two transforming phases, respectively. A linear fit of Figure 4.3 (b) yields a slope of -2.1 K/T above 1 T, while including the data point at 50 mT would lead to a slightly greater slope, -2.5 K/T.

Additionally, magnetization was measured as a function of applied field at various temperatures ranging from 100 to 300 K (Figure 4.4). The sample was cooled to 20 K before each consecutive measurement to establish well-defined starting conditions. Hysteresis loops were identified in the specimens at 150, 200 and 250K. At 100 and 300K, extremely narrow hystereses were identified and M-H plots appeared to be overlapping in Figure 4.4.

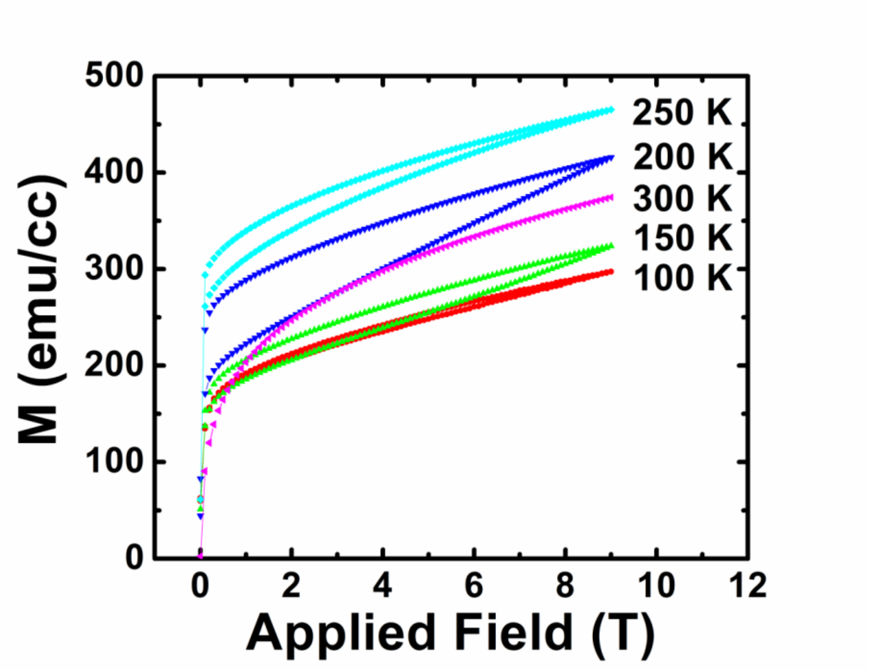

Figure 4.4 Magnetization as a function of applied magnetic field at various temperatures (100 - 300 K) consecutively measured after cooling to 20 K. A kink was observed for films tested at 150K at a field of ~ 7 T, indicating the occurrence of magnetic field induced phase transformation at this condition.

EMPA studies showed that the compositions of the as-deposited and annealed NiCoMnAl films are similar, and after crystallization, a B2 austenite phase was stabilized at room temperature. A bimodal grain size distribution and the occurrence of a small unidentifiable peak in XRD indicate that a second phase may have formed in annealed films. The chemistry and dimensions of the second phase require further investigation.

The field induced variation of critical stress $\partial\sigma_c/\partial H$ for martensitic phase transformation can be described by

$$\frac{\partial\sigma_c}{\partial H} = \frac{\partial\sigma_c}{\partial T} \cdot \frac{\partial T_M}{\partial H} \qquad \text{Equation 4.2}$$

where T_M is martensitic transformation temperature, it is evident that a large variation of field induced phase transformation temperature is necessary to achieve greater $\partial\sigma_c/\partial H$ for actuator applications. A value of 19 MPa/T was estimated for bulk polycrystalline $Ni_{40}Co_{10}Mn_{33}Al_{17}$ alloy [54]. The value of dT_M/dH for our sputtered NiCoMnAl films was measured to be ~ 2.1 K/T, which is lower compared to bulk, ~ 3.6 K/T [31] , but slightly higher than that of the epitaxial Ni-Co-Mn-In film, ~ 1.5 K/T [30].

The thermal hysteresis of the current films is relatively wide. It has been reported that the addition of Co leads to a change in the martensitic crystal structure from a modulated structure such as 10M and 14M to a non-modulated structure, $L1_0$, and that the thermal hysteresis in the martensitic transformation from B2 to $L1_0$ phase is larger than the transformation to a modulated structure [31]. Additionally we suspect that the existence of small grains in annealed films may have contributed to the broad hysteresis. Small second phase grains could increase both the stored elastic energy and the frictional resistance to interfacial migration, and thus lead to larger hysteresis loop. The M-H hysteresis is negligible at 100 K as the film is in martensitic state, which is only weakly magnetic, and there is no reverse (martensite-to-austenite) phase transformation throughout the range of applied field (up to 9 T). At 150 K, the sample exhibits the onset of magnetic field-induced reverse transformation due to different magnetization between martensite and austenite. Such a transition has also been identified in epitaxial NiCoMnIn films at ~ 8.5 T at 350K [30]. As the temperature increases, the magnitude of applied field required to induce FIPT decreases. Furthermore, the area within the M-H hysteresis loop increased to a maximum at ~ 200 K, indicating that the field induced phase transformation is most dramatic, but still may not be completed at such a temperature. Further increase in test temperature leads to diminished hysteresis. At 300K, an extremely narrow hysteresis is identified as austenite becomes dominant at this temperature.

4.5 Summary

In summary, $Ni_{45}Co_7Mn_{28}Al_{20}$, films were fabricated using a co-sputtering technique. Co-sputtering was employed to tailor film composition to similar compositions of bulk NiCoMnAl alloys reported in literature. While as-deposited films had a mixture of amorphous and nanocrystalline microstructure, and thus, did not exhibit a martensite-to-austenite phase transformation, annealed films exhibited a magnetic field induced martensitic transformation. The field-induced phase transformation temperature rate exceeds 2 K/T, implying that a large field induced variation of critical stress is likely in such a thin film system. Further experiments to tailor the chemistry of films and explore appropriate heat-treatment procedures may lead to a complete and reversible magnetic field induced phase transformation with narrow hysteresis.

5. THE INFLUENCE OF GRAIN SIZE ON MARTENSITE TEMPERATURES IN POLYCRYSTALLINE NICOMNAL MAGNETIC SHAPE MEMORY ALLOY FILMS

5.1 Overview

$Ni_{46}Co_7Mn_{28}Al_{19}$ is a magnetic shape memory alloy, which undergoes a martensitic phase transformation in a magnetic field. However, as-deposited $Ni_{46}Co_7Mn_{28}Al_{19}$ films fabricated using magnetron sputtering consisting of nanocrystals does not exhibit ferromagnetic behavior or a martensitic phase transformation. In this study, we show that appropriate annealing times resulted in room temperature austenite grains that exhibited a martensite transformation, while longer annealing times produced martensite. Furthermore, we show that the controlled heat treatment leads to grain growth and consequently an increase in martensitic phase transformation temperatures, revealing a prominent grain size effect on martensitic phase transformation.

5.2 Introduction

Magnetic shape memory alloys (MSMAs) have received much attention since 1996 when a large magnetic-field induced strain (MFIS) was first reported in unstressed Ni_2MnGa single crystals [18]. The MFIS in Ni-Mn-Ga alloys, which can generate strains up to 10% in a magnetic field, originates from the ferromagnetic martensite variant reorientation as a result of the large magnetocrystalline anisotropy energy (MAE) [20]. Recently, a new class of magnetic shape memory alloys (MSMAs) termed metamagnetic

SMAs [34, 132], has been developed where a magnetic field lowers the martensite transformation (MT) temperatures to produce a magnetic field induced strain (MFIS) in both single crystal and polycrystalline alloys resulting in a magnetic field-induced reverse transformation (MFIRT). The decrease in transformation temperatures is due to the difference between magnetization of a ferromagnetic parent phase and non-magnetic or weakly magnetic martensite phase, and is proportional to the Zeeman energy. MSMAs that recover from prestrain by MFIRT are said to exhibit a metamagnetic shape memory effect.

The metamagnetic shape memory effect has been reported for Ni-Co-Mn-In [29, 34, 133], Ni-Co-Mn-Sn [25, 134], and Ni-Co-Mn-Al [26, 31, 54] alloys. Recently, we fabricated and characterized the MFIRT for a $Ni_{45}Co_{7}Mn_{28}Al_{20}$ thin film [56]. Since MFIRT does not depend on orientation and is proportional to the Zeeman energy, a larger work output is generated compared to work associated with martensite variant rearrangement [33]. Therefore, MSMAs that exhibit a metamagnetic shape memory effect are candidate materials for high performance multifunctional actuators. Moreover, MSMA thin films have potential use as MEMS sensors for active and passive damage detection.

Studies investigating size effects in SMAs [135] and MSMAs [136-139] have been reported for constrained and unconstrained structures. Thermally induced martensitic transformation was suppressed in bulk nanocrystalline NiTi with grain sizes of 60 nm or less [135], while a minimum thickness of 100 nm is required to observe a phase transformation in NiTi thin films [140]. Although a martensite transformation was not observed for FePd nanoparticles below 25nm [137], the largest MFIS (~0.065 %) observed for Ni-Mn-Ga bilayers was found for a 100 nm thick film on a 10 μm thick Mo substrate [138]. An obvious size effect exists where decreasing grain size or reducing film thickness results in a shift of the transformation temperature in both bulk and thin film materials. Few studies are available in the current literature regarding grain size dependence on the MT temperature for metamagnetic shape memory alloys, Ni-Co-Mn-X (X = In, Al, and Sn).

Fabrication of NiMn-based Heusler-type alloy thin films requires either deposition onto a heated substrate or post-deposition heat treatment to promote atomic ordering of the film's crystal structure. Improper heat treatment can lead to the formation of non-transforming precipitates, which is a deleterious effect [141]. Therefore, understanding how heat treatments affect the microstructure of MSMA films and their MT temperatures is paramount for achieving multifunctional properties in these films.

In this study, we study the effect of grain size on the MT temperatures of $Ni_{46}Co_{7}Mn_{28}Al_{19}$ MSMA films. We prepared films with various grain sizes using a controlled heat treatment after the deposition. The MT temperatures were determined from magnetic measurements.

5.3 Experimental

1500 nm thick $Ni_{46}Co_{7}Mn_{28}Al_{19}$ alloy films were deposited onto unheated SiO_2 substrates by co-sputtering of Co and Ni-Mn-Al alloy targets with 99.95% purity. The base pressure prior to the deposition was 5×10^{-8} Torr, while argon pressure during deposition was 3.5 mTorr. As-deposited films were mounted on a sliding quartz rod that enabled rapid movement between the heated and unheated portions of a tube furnace with constant argon flow. This setup allowed both annealing at 973 K for times ranging from 1-30 min and rapid cooling to be carried out in an inert environment. The microstructure of as-deposited and annealed films was analyzed at room temperature using x-ray diffraction (XRD, Bruker AXS-D8 with Cu K_α radiation). Film microstructure and texture were determined by imaging experiments conducted using a JEOL 2010 transmission electron microscope (TEM) operated at 200 kV, and equipped with a Gatan SC1000 ORIUS CCD camera. The chemical compositions of the as-deposited and annealed films were determined using electron probe microanalysis (EPMA, Cameca SX50 electron microprobe, 20 kV, 10 nA) and scanning transmission electron microscopy (STEM) experiments with electron-dispersive x-ray spectroscopy (EDS) analyses using a FEI Tecnai F20 Super Twin microscope operated at 200kV. The thermomagnetic properties of the films were measured using a physical property measurement system (PPMS, Quantum Design) equipped with a vibrating sample magnetometer module.

5.4 Results and discussion

Figure 5.1 shows room temperature XRD profiles for an as-deposited film and films annealed at 973 K for times ranging from 1 to 30 min. The as-deposited film has a broad diffraction peak suggesting that the microstructure consisted of nanocrystals in an amorphous matrix. Initial annealing at 973 K for 1 min resulted in crystallization of the as-deposited film, and a shift of the diffraction peak indicates a decrease in the average d-spacing. The singular peak belongs to $(110)_A$ austenite (B2 phase). The absence of the (111) superlattice diffraction peak indicates a lack of $L2_1$ ordering, and is consistent with cooling the films from above the Ni-Mn-Al B2/$L2_1$ order-disorder transition temperature, $T_c^o \sim 773\ K$ [142]. It is worthwhile to note that reported martensite finish temperatures (M_f) for similar bulk alloy compositions ranges from 353 – 369 K [31, 112]. Therefore, it is striking that films annealed for 5 min or less exhibit an austenite phase at room

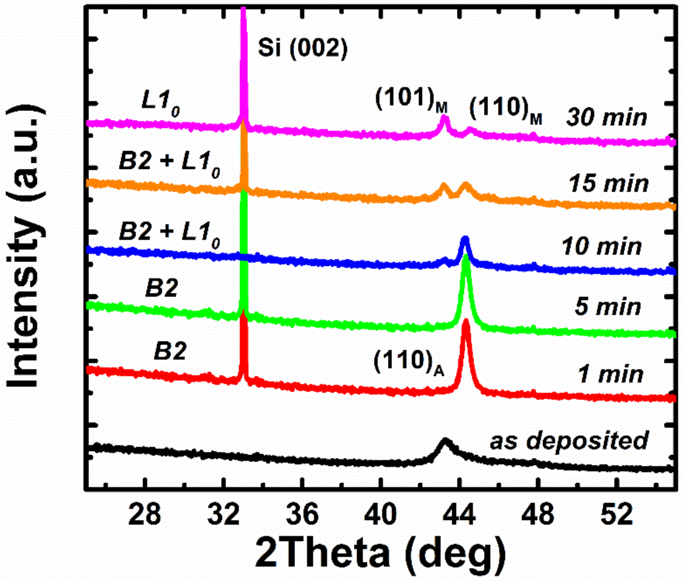

Figure 5.1 Room temperature XRD spectra of as-deposited and annealed $Ni_{46}Co_7Mn_{28}Al_{19}$ films 1500 nm in thickness. Films were annealed at 973 K for times ranging from 1 to 30 minutes. Increased annealing time leads to an additional peak indicating a transformation from austenite (A) to martensite (M) phase.

temperature. Increasing the annealing time to 10 min and greater leads to dissociation of the $(110)_A$ austenite peak, indicating a loss of crystalline symmetry, corresponding to a shift from a symmetric cubic austenite phase to a less symmetric martensite $L1_0$ phase. Calculated lattice parameters are $a_{B2} = 2.89$ Å and $a_{L1_0} = 2.88$ Å and $c_{L1_0} = 2.96$ Å, which are consistent with previous reports [31, 56].

Bright-field TEM images in Figure 5.2 demonstrate the evolution of grain growth in films annealed at 973 K for various times. As-deposited films had an average grain size of 25 nm embedded in an amorphous matrix, in qualitative agreement with the XRD data. After annealing for 1 min at 973 K, the film showed significant recrystallization (Figure 5.2 (b)). Annealing for 5 min led to complete crystallization and grain impingement. A bimodal grain size distribution became apparent after 10 min, with some grains exhibiting abnormal grain growth to many times the size of others. Grain size continued to increase after annealing for 15 min, and martensite variants became readily visible in the film annealed for 30 min (Figures 5.2 (e) and (f)).

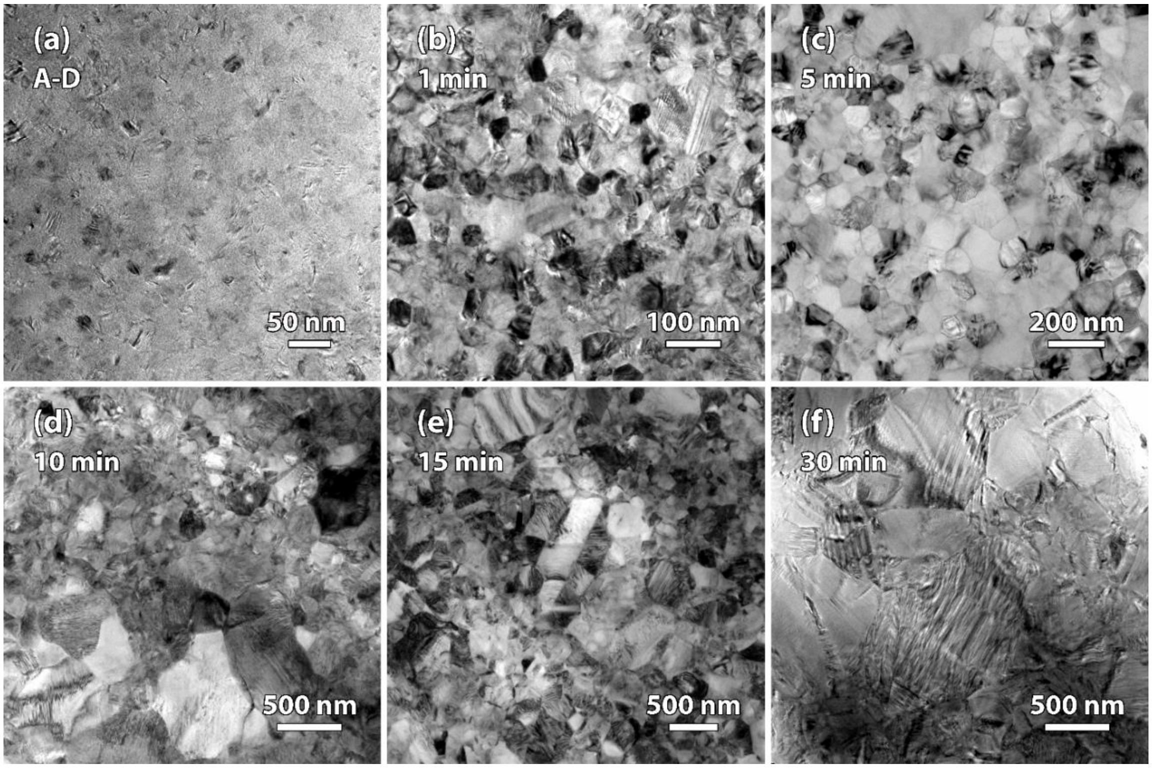

Figure 5.2 Bright-field TEM images of as-deposited and annealed $Ni_{46}Co_7Mn_{28}Al_{19}$ films annealed for different times at 973 K, (a) as-deposited, (b) 1 minute, (c) 5 minutes, (d) 10 minutes, (e), 15 minutes, and (f) 30 minutes.

Figure 5.3 (a) shows the thermomagnetization (M-T) curves for heating and cooling of an as-deposited film and annealed films in a magnetic field, H = 50 mT. The low magnetization of as-deposited film remains nearly constant as a function of temperature. This behavior indicates the film does not exhibit ferromagnetic behavior at low fields, which may be related to the lack of long-range crystalline order as seen from the XRD spectra in Figure 5.1. Interestingly, as the annealing time and grain size increased past 5 min, the peak magnetization decreases. The magnetization of the film as a function of temperature can be estimated near the Curie temperature (T_C) using mean-field approximation theory as $M(T) \propto (T_C - T)^{\beta}$, where β ~ 0.3 – 0.5 is a critical exponent [143]. Therefore, as the martensite start temperature (M_s) approaches T_C, the magnetization of the annealed films decreases. Kainuma *et al.* reported magnetization for similar bulk alloy compositions at small magnetic fields (M_p is 10 – 23 emu/g at 50 mT), where M_p is the peak magnetization [31]. In this work, the austenitic films have a higher magnetization as compared to the bulk under low-field measurements, which indicate the films may have a lower coercivity compared to the bulk alloys.

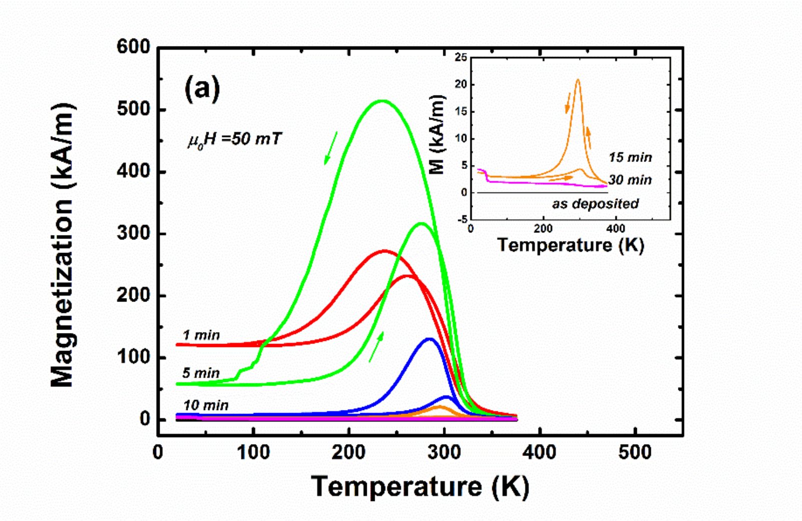

Figure 5.3 (a) Thermomagnetization curves of as-deposited and annealed $Ni_{46}Co_7Mn_{28}Al_{19}$ films measured in a magnetic field of 50 mT. The inset illustrates the non-ferromagnetic behavior of the as-deposited film and weakening magnetization of films annealed for times greater 15 minutes. (b) Martensitic transformation temperatures vs. annealing time extracted from the thermomagnetization measurements in Figure 5.3 (a). The transformation temperatures are defined from the extrapolations as shown in the inset.

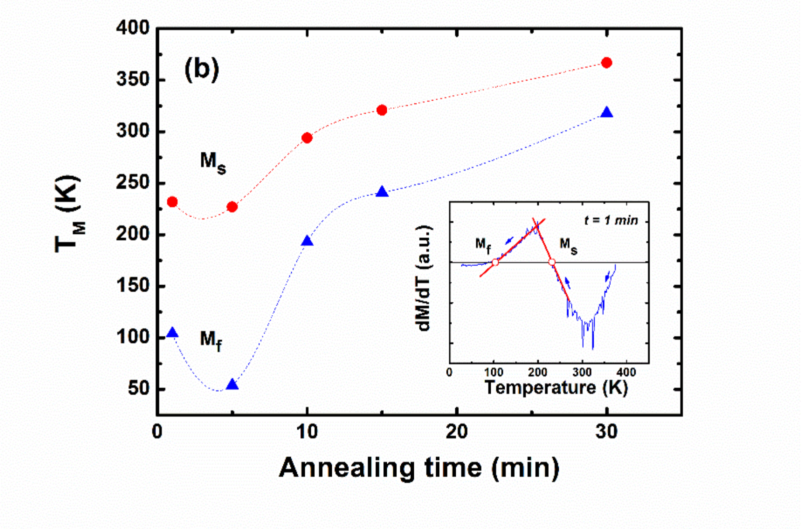

Figure 5.3 continued

Figure 5.3 (b) shows the annealing time dependence of the MT temperatures. The M_s and M_f temperatures are defined as the intersection of the baseline, dM/dT = 0, and the extrapolation of the side peak (see Figure 5.3 (b) inset). Initially, the MT temperatures decrease as the annealing temperature is increased from 1 to 5 min. However, the transformation temperatures increase for annealing times greater than 5 min. Potential mechanisms behind such a reversal will be discussed later.

Figures 5.4 (a) and (b) show that the M_s temperature increases as the average grain size increases and approaches ~ 385 K, which is the M_s for bulk compositions with similar valence electron concentrations, *e/a* = 7.76 [31, 112]. A similar effect of austenitic grain size on martensitic transformations has been studied in steels, SMAs, and MSMAs. Nanostructured materials contain a large number of grain boundaries that resist martensitic transformation [135]. A grain boundary is a defect in the crystal structure, and may in some cases act as a preferential site for martensite nucleation provided there is enough volume for the growing variant. However, dense grain boundaries and small grain volumes in nanocrystalline MSMAs impose geometrical constraints that stabilize the austenite phase by suppressing the martensite transformation. Hence, increasing annealing time leads to larger grain size, which increases the transformation temperatures due to the reduction of constraints from grain boundaries.

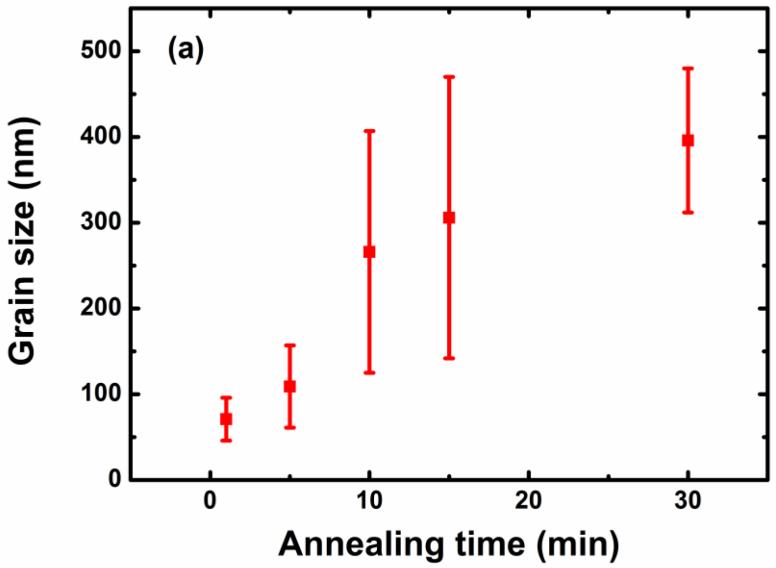

Figure 5.4 (a) Average grain size increases monotonically with annealing time. (b) Martensite start temperature typically escalates with increasing grain size.

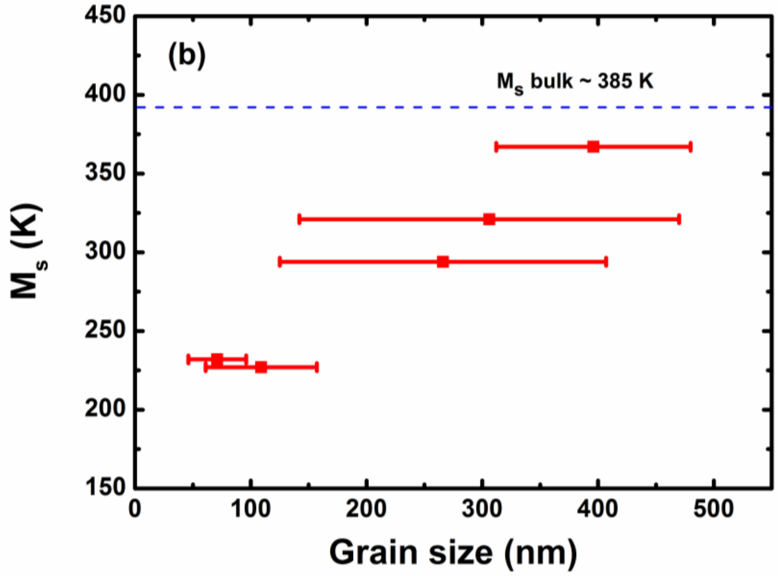

Figure 5.4 continued

The martensite transformation temperatures depend largely on the chemical composition and atomic ordering [45, 95], and to a degree on non-chemical effects such as stress and moderate applied magnetic fields. The martensite transformation occurs near the equilibrium temperature, *T_0*, between austenite and martensite phases, and needs additional energy to overcome nonchemical terms in the thermoelastic balance [78]. Nonchemical terms in the thermoelastic balance include magnetic contributions, which are responsible for the metamagnetic shape memory effect, and include elastic terms. As grain size decreases, the elastic energy term increases, and thus, more undercooling is required in order to complete the martensitic transformation. In addition to increased elastic energy due to grain size effects, thin films are subject to residual stresses due to substrate confinement.

Residual stresses in polycrystalline thin films are due to intrinsic and thermal stresses. Intrinsic stresses develop during the deposition process, while thermal stress result from the differential expansion of the substrate/film interface subjected to a temperature change. The film annealed for 1 min delaminated from the substrate, which was caused by CTE and thermal conductivity differences between the metallic film and ceramic substrate. Films annealed for longer times allowed sufficient time for the film and substrate to reach thermal equilibrium, and thus remained confined to the substrate. In this study, the films were heated and cooled to the same temperature. Therefore, the residual stress is similar for films annealed for times greater than 1 minute. Thus, increased annealing times beyond 5 min do not increase the residual stress significantly enough to explain an increase in the MT temperatures.

Although the film annealed for 1 min delaminated from the substrate resulting from a large tensile thermal residual stress, the film is freestanding, and under less residual stress than the films confined to the substrate. The decrease of M_s observed from annealing 1 to 5 min, could be related to greater residual stresses developed in the confined films annealed for 5 to 30 min. A similar trend was observed in N-Mn-Ga films where the transformation temperature was found to increase as the film thickness and stress decreased [102]. Thus, the freestanding film, which was annealed for 1 min, underwent a MT at a higher temperature than would be observed for a similar film confined to a substrate.

A few factors should be considered when discussing the shift of MT temperatures: alloy composition, degree of ordering, stress (applied or residual), and parent phase grain size. MT temperatures are largely dependent on alloy composition in MSMAs. First, from STEM/EDS measurements, the composition of the films was found to be almost constant, irrespective of the annealing time. Therefore, the effect of composition on MT temperature in this study is likely to be insignificant. Second, the absence of a (111) $L2_1$ superlattice reflection, irrespective of annealing time suggests that the degree of order is not significantly changed with annealing time, excluding the effect of degree of ordering. Third, with the exception of the film annealed for 1 minute, the thermal residual stress in the films remain relatively constant for the isothermally annealed films, and thus does not explain the large increase in MT temperatures. Finally, the shift in the transformation temperature is consistently correlated to the increase in average grain size from a few to hundreds of nanometers after annealing.

The decrease in the MT temperature induced by a magnetic field in metamagnetic alloys can be determined from the following Clausius-Clapeyron relation between temperature and a magnetic field as follows

$$\frac{dT}{dH} = \frac{-\mu_0 \Delta M}{\Delta S} \qquad \text{Equation 5.1}$$

where μ_0 is the vacuum permeability, ΔM and ΔS are the change in the magnetization and entropy from the martensite to the parent phase, respectively. Equation 20 can be approximated as

$$\Delta T = \frac{-\mu_0 \Delta M}{\Delta S} H \qquad \text{Equation 5.2}$$

where H is the applied magnetic field. A strong inverse correlation exists between ΔS and the difference between the Curie temperature and martensite start temperature, $(T_c - M_s)$, that is ΔS decreases as $(T_c - M_s)$ increases. This entropic relationship is qualitatively explained from thermodynamic considerations [29, 133]. Therefore, in addition to the chemical composition and atomic ordering, grain size may be used to increase the MT temperature shift by decreasing the change in entropy between austenite and martensite phases.

5.5 Summary

In summary, as-deposited films exhibited neither ferromagnetic nor martensitic behavior. Controlled heat treatment of the as-deposited films with increased annealing time results in increased grain size, which leads to ferromagnetic behavior and an increase in MT temperatures. Significant implications of this study include the use of submicron-sized grains to tailor the difference between the Curie temperature and M_s temperature $(T_c - M_s)$, which is inversely proportional to the change in entropy, to cause an increase in dT/dH. These parameters, along with composition, are essential to fabricating systems that reversibly transform in an applied magnetic field.

6. PRECIPITATION AND GRAIN SIZE EFFECTS ON THE MARTENSITIC PHASE TRANSFORMATIONS OF NICOMNIN HIGH TEMPERATURE SHAPE MEMORY ALLOYS

6.1 Overview

Amorphous $Ni_{50}Co_6Mn_{38}In_6$ films 20 μm in thickness were fabricated using DC magnetron sputtering. Freestanding films crystallized during annealing in a differential scanning calorimeter (DSC) where the maximum temperature was varied from 450 to 700 °C. Crystallized films retained a non-modulated $L1_0$ martensite structure at room temperature. DSC studies showed that as the annealing temperature increased, the martensitic phase transformation temperature decreased substantially. Scanning transmission electron microscopy revealed the formation of cobalt-rich precipitates near 500 °C and an increase in martensite grain size as the annealing temperature increased from 500 to 700 °C. It has been shown that cobalt-rich precipitates decrease the valence electron concentration (*e/a*) of the twinned martensite, and hence cause a decrease in martensitic phase transformation temperature. Additionally, submicron grain size in the annealed freestanding films significantly suppressed the martensite transformation temperatures compared to similar bulk compositions.

6.2 Introduction

Shape memory alloys (SMAs) perform work when acting against a biasing force while the SMA recovers from its deformed shape, which is a result of a reversible martensitic transformation. The martensitic transformation (MT) is a diffusionless solid to solid phase transformation that can be controlled by a temperature, stress, or magnetic field. SMAs may be classified as conventional, magnetic, or high temperature. Conventional SMAs operate at temperatures below 100 °C, and consequently have been integrated into MEMS devices for biomedical applications such as micropumps used for drug delivery [11, 12]. Magnetic shape memory alloys (MSMA) utilize energy generated from an applied magnetic field to provide actuation, and are able to operate at higher frequencies rates (< 1,000 Hz) compared to conventional SMAs (<100 Hz), which are limited by a slower heat transfer mechanism [24]. High temperature shape memory alloys (HTSMA) operate at temperatures above 100 °C, so the rate of cooling offers a faster response time compared to conventional SMAs. Additionally, the automotive, aerospace, and oil industries have a technological need for compact actuators that are able to operate at temperatures above 100 °C, possibly as fail-safe devices [24, 61, 144].

While the majority of conventional SMAs operate near room temperature, HTSMAs operate in a temperature regime where the MT, a diffusionless process, may be influenced by diffusion based processes such as recrystallization, decomposition, and recovery [5]. Firstov *et al.* distinguishes HTSMAs from classical SMAs by the reverse transformation temperature, A_s; the onset of the reverse transformation starts only above 120 °C in a stress-free condition. It is important to note that this definition includes SMAs that exhibit a phase transformation (Ms, Mf) below 120 °C, but excludes alloys with A_f below 120 °C [61]. Ma *et al.* categorize HTSMAs into three temperature ranges based on the operating temperature of a potential application: 100-400 °C, 400-700°C, and above

700°C. Due to the relative ease of experimentation compared to the higher temperature ranges, most HTSMA research has been performed within the 100-400 °C. However, to date no successful alloy has been developed with transformation temperature well above 120 °C, and thus are not readily found in commercial high temperature applications [26, 61]. Ti-Ni-(Pd, Pt) alloy systems have received the most attention, and derive their increased transformation temperatures from Ti-Pd (M_s = 600 °C) and Ti-Pt (M_s = 1100 °C) binary systems, and shape memory behavior from the NiTi SMA [26, 145]. However, both Pd and Pt are heavy and expensive elements, and at least 15 at% of either is required to increase the transformation temperature.

Ni-based HTSMAs were some of the earliest SMAs extensively studied with transformation temperatures above 100 °C [146-149]. The two main alloy systems were Ni-Mn and N-Al. Ni-Mn alloys exhibit nearly thermoelastic MT between 650 and 750 °C. Ni-rich N-Al alloys exhibit a B2 to L10 thermoelastic transformation with MT temperatures as high as 900 °C. However, binary NiMn is very brittle and prone to tempering at 400 °C [148, 150]. Magnetron sputtering can be used to study and optimize the shape memory behavior of Ni-Mn alloy thin films.

Like other SMAs, the structural and physical properties of Ni-Mn-Co-In alloys are sensitive to the alloy's composition and atomic order. Ito *et al.* reported that the martensitic temperature of a Heusler-type NiCoMnIn alloy decreased by approximately 230 °C by increasing the indium concentration a few atomic percent [29]. In a separate study, the effect of atomic ordering on a NiCoMnIn alloy was investigated and the martensitic start temperature from the fully ordered $L2_1$ structure was 60 °C less than the partially ordered

B2 austenitic phase [95]. Annealing has been used to influence the physical properties of SMAs, and in some cases results in precipitates that affect the ductility of SMAs as well as the transformation temperatures [108-110]. The NiCoMnIn system presents numerous opportunities for additional study. It is also possible that while the formation of precipitants is generally detrimental to the shape memory effect, a small volume of precipitants may increase ductility [99]. This could prove useful in some industrial applications.

Additionally, microalloying, melt spinning, and powder metallurgy have been used to refine grain size to improve ductility [150]. Microalloying Ti-Ni-Pd HTSMAs with boron increased room temperature elongation to failure from 8 to 16% strain, but did not improve shape memory behavior [26].

Recently, we fabricated and characterized a high temperature shape memory Ni-Mn-Co-In alloy that exhibited a reversible shape memory effect [42]. In thin films, recrystallization leads to a change in residual stresses [6], and the formation of precipitates that create chemical and stress gradients that affect the transformation behavior of HTSMA thin films [7,8].

In this paper, we investigate how the evolution of precipitates influence the transformation temperatures of a HTSMA NiCoMnIn, and how submicron grain sizes suppress the martensitic transformation temperatures compared to bulk.

6.3 Experimental methods

Using dc magnetron sputtering, a 20µm Ni-Co-Mn-In film was deposited onto an unheated Si (100) substrate with a one µm thick thermal oxide. Sputtering was performed using a base pressure of 3×10^{-5} Pa, an argon pressure of 0.5 Pa, and deposition power of 600 W for approximately 8,000 seconds. Poor adhesion between the deposited film and substrate resulted in freestanding films that were freed from the substrate. A series of 3 mm disks were formed from the freestanding films and used for further characterization.

Transformation temperatures for the as-deposited freestanding films were identified using a TA Instruments Q1000 pressurized differential scanning calorimeter (DSC). The cell was pressurized with an ultra-high purity nitrogen atmosphere to a constant pressure of 140 kPa. Individual samples weighing approximately 2 mg were heated at a rate of 20 °C/min to target temperatures of 450, 500, 600, and 700 °C. The films cooled in the inert atmosphere to 50 °C and the cycle was repeated once.

Grain size analyses of the annealed films were performed using transmission electron microscopy (TEM). Plan-view samples were prepared from the 3 mm disks annealed in the DSC and ion-milled to electron transparency. Imaging was performed in a JEOL-JEM 2010 transmission electron microscope with a 200 kV accelerating voltage.

An energy dispersive spectrometer (EDS) interfaced with a FEI TECNAI G2 F20 field emission TEM was used to determine chemical compositions of individual grains as well as provide a compositional gradient between neighboring grains. Chemical analyses of the as-deposited freestanding film were carried out using a CAMECA SX 50 microprobe using wavelength dispersive methods (WDS).

6.4 Results

6.4.1 DSC results

As-deposited samples were cycled twice in the calorimeter to different maximum temperatures to determine the crystallization temperature (Tx) and stability of MT peaks. Figure 6.1 (a) shows a typical DSC curve for two NiCoMnIn films heated to 500 and 700 °C, and cooled to 50 °C. Two sets of peaks were observed for both films. The large-exothermic peaks correspond to the film crystallization that occurs during the initial heating, and the smaller-endothermic peaks correspond to the forward transformation from the austenite to martensite phase while cooling the sample. Due to a lack of crystalline order in the as-deposited film prior to film crystallization, a reverse martensitic transformation from the martensite to parent phase was not observed during the first heating cycle.

The crystallization temperature was defined as the maximum intensity of the crystallization peak and was approximately, $T_x \sim 450$ °C. The MT temperatures were determined using the intersection of the baseline and the tangent line with the largest slope of the peak. The M_s temperature varied from 350 to 275 °C for the films heated to 500 and 700 °C, respectively. The origin of this shift in MT temperature will be discussed later.

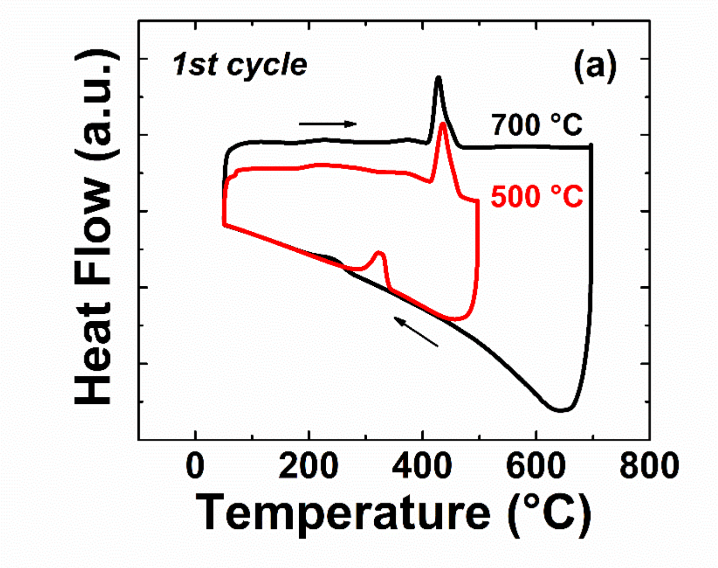

Figure 6.1 (a) The first cycle of heating and cooling DSC curves for two NiCoMnIn foils: one heated to 500 °C and the other to 700°C. Crystallization was observed during the heating, but the reverse transformation was absent. The forward transformation was observed during cooling. (b) The second cycle of heating and cooling DSC curves for the same NiCoMnIn foils. Both forward and reverse transformations were observed in the crystallized film. (c) Heating segments for three samples heated treated at 500, 600, and 700 °C Martensite to austenite phase transformation leads to an endothermic peak. Peak temperature is the highest for the film annealed at the lowest temperature.

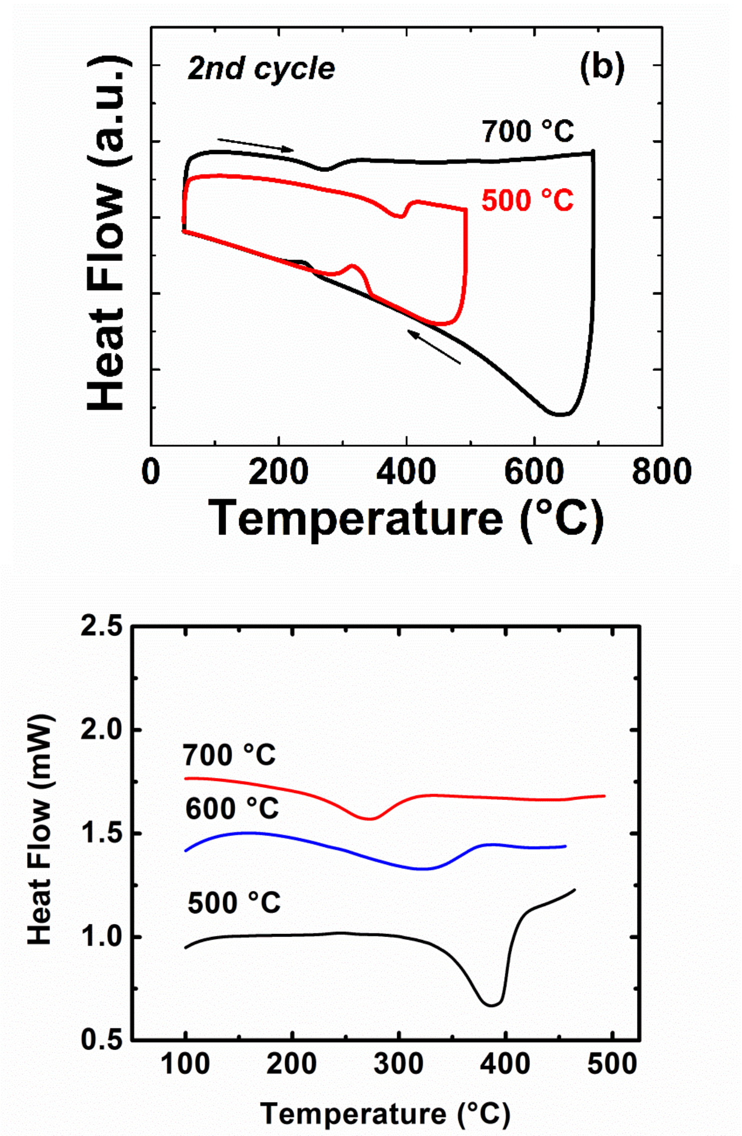

Figure 6.1 continued

Figure 6.1 (b) shows the second cycle of the heating and cooling cycle where the presence of both the reverse and forward MT temperatures indicates a reversible shape memory effect for this alloy. Additionally, we notice the absence of the crystallization peak as expected. However, it is important to note the difference in MT temperatures for the films annealed at different temperatures, and the reduction of the area of the exothermic and endothermic peaks.

For clarification, Figure 6.1 (c) shows only the heating curve for films annealed at 500, 600, and 700 °C. From this figure we see a consistent decrease in the reverse MT temperature. A similar trend is observed for the forward transformation.

6.4.2 TEM results

TEM samples were prepared from the samples annealed in the DSC in order to further investigate the annealing temperature dependence of the transformation temperatures, Figure 6.2 shows TEM micrographs of samples annealed at temperatures ranging from 450 to 700 °C.

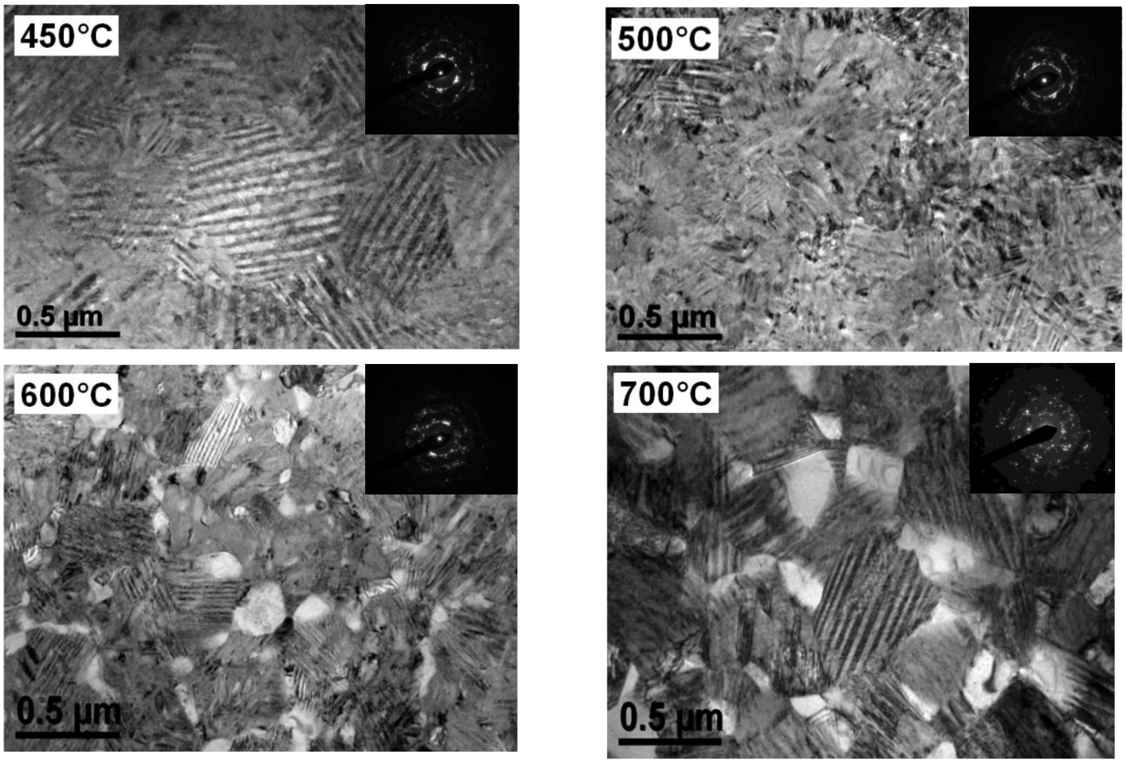

Figure 6.2 Plan-view TEM micrographs of samples annealed to various maximum temperatures. Annealing induces grain growth, and the formation of twined martensite.

Films annealed at 450 °C had an average grain size of 350 nm. As the annealing temperature increased from 450 to 700 °C, the average grain size initially decreased to 110 nm at 500 °C, and then monotonically increased to an average grain size of 320 nm for films annealed at 700 °C. At 500 °C, the grain size decreases and the grain boundaries become less defined. The reason for this unclear, but may be due to the competition between recrystallization of the austenite grains and nucleation of precipitates at the parent phase grain boundary. Using nanobeam diffraction, the crystal structure of the precipitates were determined to correspond with the fcc γ phase.

6.4.3 STEM results

Figure 6.3 (a) is a room temperature STEM micrograph of a sample annealed at 700 °C in the DSC. The red line located next to the red cross indicates the path of the of the electron beam used for STEM-EDS analysis. A beam diameter of approximately 2nm was used to determine the change in valence electron concentration, *e/a*, of the individual grains (see Figure 6.3 (b)).

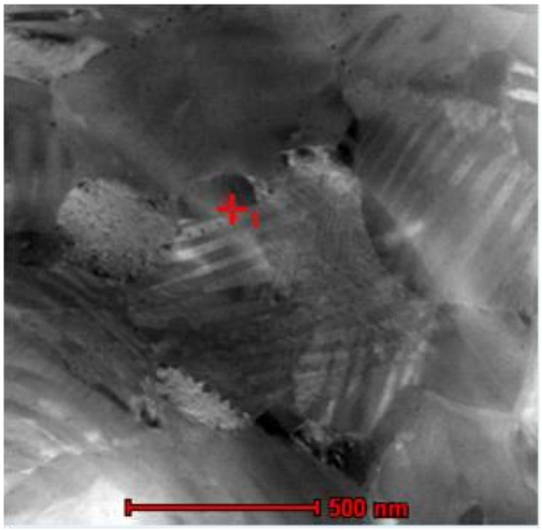

Figure 6.3 (a) An STEM micrograph of a NiCoMnIn film annealed to 700 °C. (b) EDS compositional line profile for the annealed NiCoMnIn film. The dash line is a guide to mark the location of interface between the precipitate and the matrix. The matrix appears to have a depletion of Ni and Co and enrichment of In. (b) is an energy dispersive x-ray spectroscopy (EDS) line scan across a grain boundary interface of a precipitate and the matrix. The area of the line scan is indicated by the crosshair in Figure 6.3 (a). The change in atomic concentration across the grain boundary indicates a Co-rich and In-deficient precipitate forms when the annealing temperatures are above 450 °C. As the annealing temperature increases, the grain size of indium rich and cobalt deficient precipitates increase, which causes an overall decrease in the electron concentration, *e/a*, of the transforming matrix, and decrease in the martensitic transformation temperature.

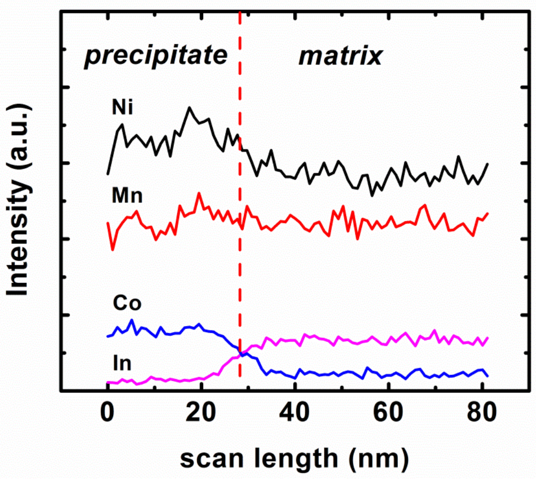

Figure 6.3 continued

Figure 6.3 (b) indicates that the chemical composition changes as the electron beam scans across the precipitate and twinned matrix interface. STEM confirms that the decrease in the electron concentration (*e/a*) of the twinned matrix is due the formation of a Co-rich NiMn precipitate. Since Ni, Mn, and In contain 10, 7, and 3 valence electrons, respectively, the formation of Co-rich NiMn precipitates decreases the electron concentration of the existing martensite.

6.5 Discussion

6.5.1 Effect of precipitation

As the annealing temperature increased, both the martensite and reverse transformation temperatures decreased (see Figure 6.4). Initially, the decrease in transformation temperature was unexpected since grain boundaries are expected to strengthen the parent phase [4]. Therefore, one would expect the martensitic transformation start temperature (M_s) to increase as the grain size increased. The data obtained from the DSC experiments (Figure 6.1), and a plot of MT temperatures as a function of annealing temperature is illustrated in Figure 6.4.

The transformation temperatures were defined as the intersection of the baseline with the tangent corresponding to the steepest slope of the peak corresponding to the latent heat of transformation. We will discuss the mechanisms involved in the reduction of MT temperatures as the annealing temperature is increases from 450 to 700 °C.

The transformation temperature depends on chemical composition, degree of ordering, parent phase grain size, and precipitates. Recently, our group reported the precipitation of a second phase after the crystallization (~ 450 °C @ 20 °C/min) of a high temperature shape memory $Ni_{50}Mn_{38}Co_6In_6$ alloy thin film.

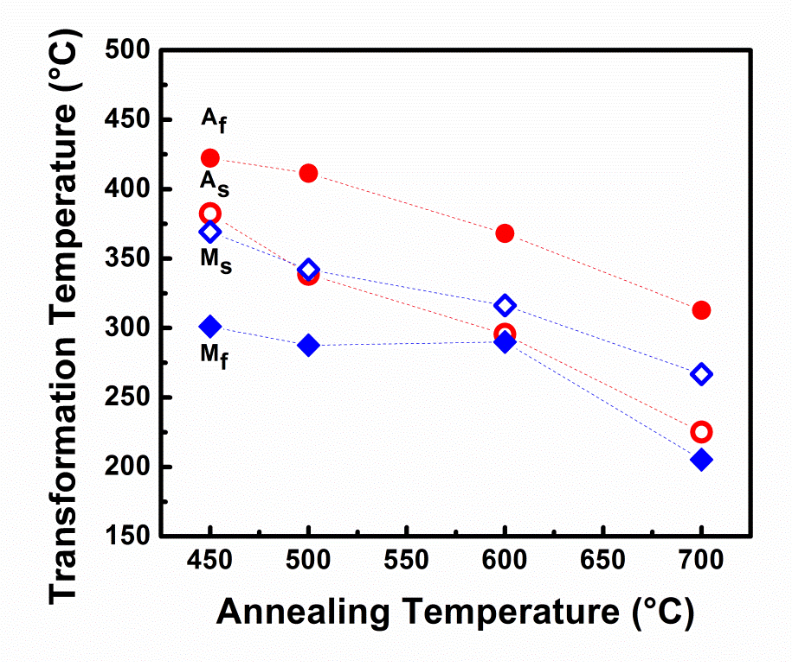

Figure 6.4 Plot of transformation temperatures taken from the DSC measurements in Figure 6.1. Annealing leads to reduction of all characteristic phase transformation temperatures.

According to the calorimeter studies, a second phase precipitated from the twined matrix at 450-500 °C [3]. Figure 6.5 shows two trends for the annealing temperature dependence on the matrix and precipitate grain size. The first trend for the transforming matrix is that as the annealing temperature increases from 450 to 500 °C the grain size initially decreases, but further increase of the annealing temperature results in an increase of the matrix grain size. The second trend, however, shows that the grain size of precipitates increased monotonically with annealing temperature in parallel with the non-monotonic matrix grain growth.

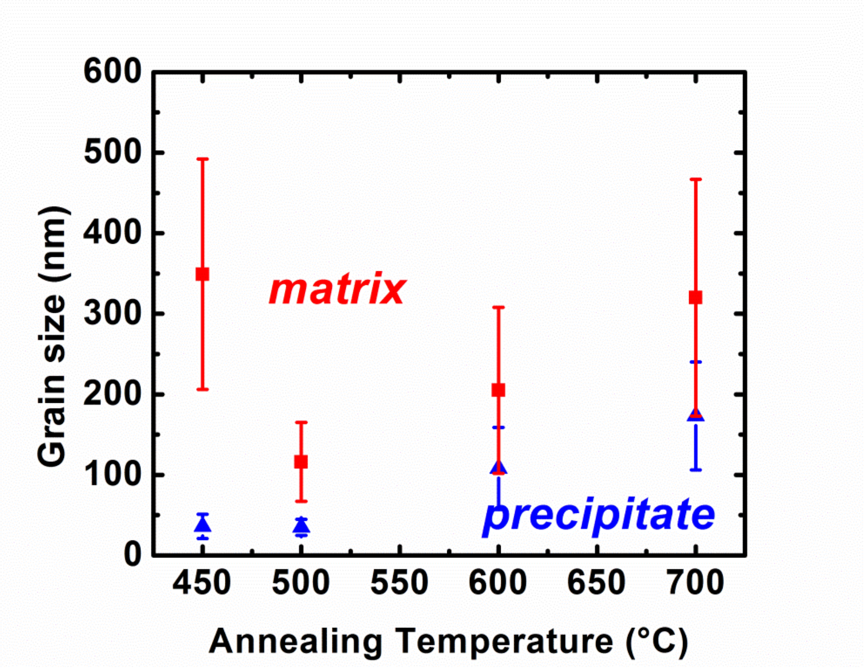

Figure 6.5 The dependence of grain size of precipitate and twinned martensite on annealing temperature for $Ni_{50}Mn_{38}Co_6In_6$ alloy films annealed at different temperatures ranging from 450 to 700 °C.

This suggests that a competition exists between recrystallization of the grain matrix and precipitation grain growth. Additionally, while precipitates have been shown improve ductility, the γ phase does not undergo MT and is therefore detrimental to the reversibility of the shape memory behavior [26].

Figure 6.6 shows the annealing temperature dependence of both the valence electron concentration and martensite start temperature. The valence electron concentration of the matrix for samples annealed at 400, 600, and 700 °C was determined from STEM measurements. The valence electron concentration of the sample annealed at 500 °C was not included in this plot due to the difficulty of distinguishing between the matrix and precipitate grains. According to Figure 6.6, increased annealing temperatures leads to a decrease in *e/a* and the martensite start temperature. The decrease of the matrix *e/a* with increasing annealing temperature corresponds to the increase in precipitate grain size. As the Co-rich NiMn precipitate grain size increases, more Ni, Mn, and Co are consumed compared to In. This mass transfer leads to a matrix with a larger percentage of indium, and hence a lower *e/a* value. Additionally, the decrease of M_s with increased annealing temperature supports the positive correlation between M_s and *e/a* observed in many NiMn-based Heusler-type shape memory alloys [85].

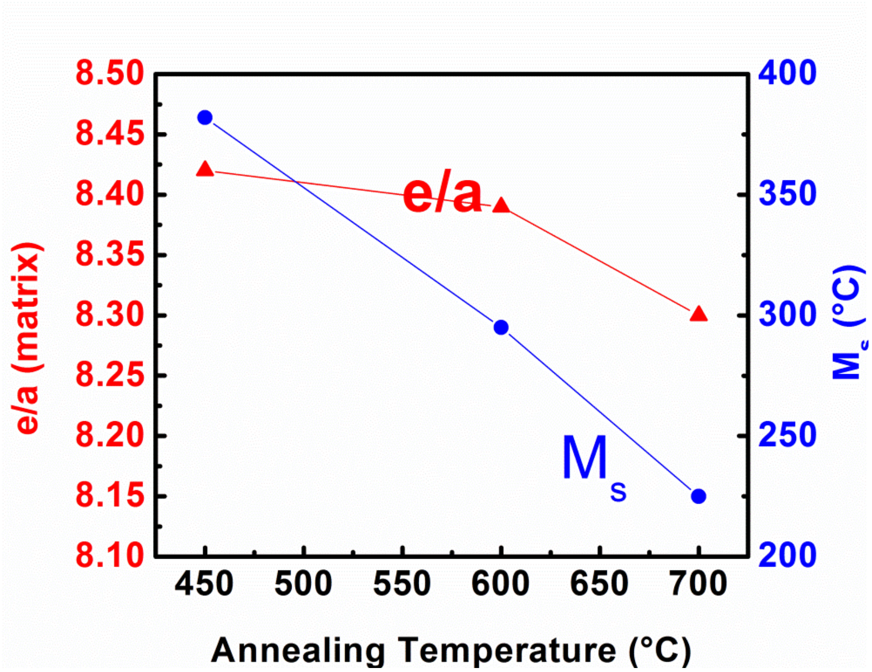

Figure 6.6 Correlation between martensite start temperature and *e/a* for annealed NiCoMnIn films. There appears to be similar trend on the reduction of *e/a* and M_s with annealing temperature.

Figure 6.7 compares the martensite start temperature as a function of the electron concentration for this work with other results found in the literature [29]. Although the slopes are similar, they are offset from one another by ~ 200 °C. Possible reasons may include residual stresses in the film caused by the formation of precipitates, difference in grain size, or difference in crystal structures.

In this study, the formation of the precipitates decreased the chemical composition of the matrix. The introduction of precipitates in the annealed samples create a shape memory alloy composite composed of a transforming matrix and precipitates that do not transform, and due the differences in composition and crystal structure between the precipitates and matrix – the composite will have heterogeneous physical properties that may affect the transformation temperature.

However, it is worthy to note that thermal hysteresis ($T_h = A_f - M_f$) while large, remains relatively constant where $T_h \sim 130$ °C – even for the sample annealed at 450 °C, which has relatively no precipitates. It is interesting that the thermal hysteresis remains relatively constant while the precipitate grain size increases. The lack of a direct correlation between the thermal hysteresis and precipitate grain size suggests that while precipitation has been shown to decrease MT temperatures, it does not fully explain the suppression of the M_s of the films compared to bulk alloys with similar compositions.

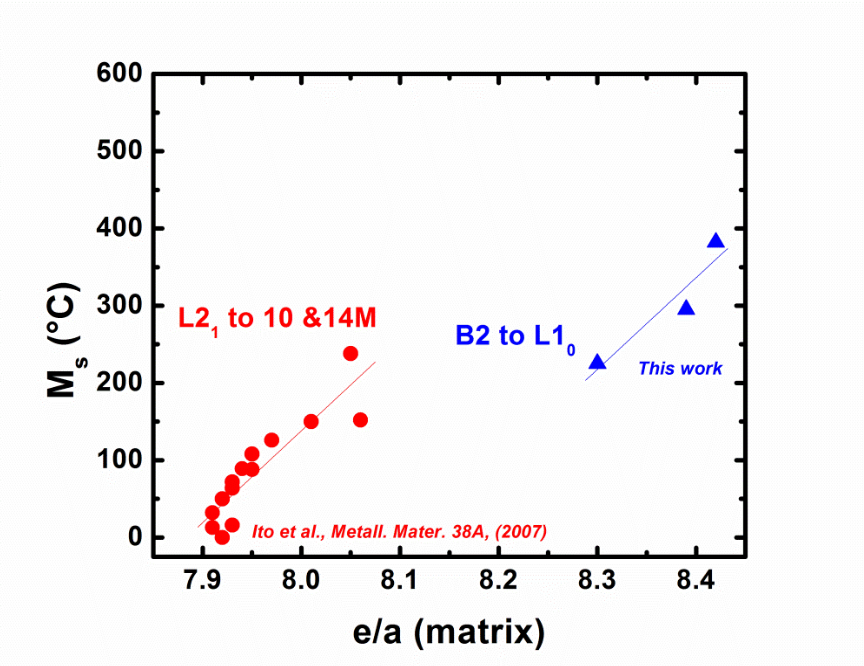

Figure 6.7 Dependence of martensite start temperature on *e/a* for NiCoMnIn bulk (literature) and thin films (this study). Although M_s appears to increases with *e/a* in films, the distribution of data seems to have a large offset in comparison to those of bulk counterparts [29].

Recently, Wang *et al.* demonstrated that the martensite start temperature is inversely proportional to the unit cell volume and suggest that electron density is a more appropriate parameter to describe the martensite start temperature [151] . Additionally, Zarinejad and Liu showed there was a volume effect for NiTi-based shape memory alloys that was successful in resolving discrepancies for NiTi alloys with (*e/a* = 7) [152]. The electron density lends itself to a more fundamental parameter related to the Fermi vector by the following expression for an isotropic electron gas

$$k_F = (3\pi n)^{1/3} \qquad \text{Equation 6.1}$$

Where *n* is the electron density, which is related to the valence electron concentration (*e/a*) by the following expression

$$n = \frac{\left(\frac{e}{a}\right)N}{V_{cell}} \qquad \text{Equation 6.2}$$

While this may be a valid alternative to characterize the transformation temperatures, this does not explain the shift in temperature between the B2 and $L2_1$ phases. The B2 crystal structure has 2 atoms per cubic volume ($V = a^3$), and can be considered as a partially disordered crystal structure, while the $L2_1$ crystal structure is considered perfectly ordered. The B2 phase has an electron density that is proportional to $2/a^3$. The $L2_1$ structure consists of four fcc lattices with a lattice parameter approximately twice as large as the B2 structure. Thus, the $L2_1$ electron density is proportional to $(16/(2a)^3)$ or $2/a^3$. Therefore, neither the valence electron concentration, *e/a,* or electron density, *n*, are able to explain the increased amount of undercooling required for the films in this work to exhibit a MT compared to bulk alloys reported in literature.

6.5.2 Effect of grain size

Studies investigating size effects in SMAs [135] and MSMAs [136-139] have been reported for bulk and thin film alloys. Thermally induced martensitic transformation was suppressed in bulk nanocrystalline NiTi with grain sizes of 60 nm or less [135], while a minimum thickness of 100 nm is required to observe a phase transformation in NiTi thin films [140]. A martensite transformation was not observed for FePd nanoparticles below 25nm. Salzbrenner and Cohen have shown that the elastic strain energy in a polycrystalline

Cu-14Al-2.5Ni SMA will cause a decrease in MT such that T_o is greater than A_s [104]. An obvious size effect exists where decreasing grain size or reducing film thickness results in a shift of the transformation temperature in both bulk and thin film materials.

Thermodynamic considerations can be used to discuss the decrease in transformation temperature as the grain size decreases. The thermoelastic equilibrium condition can be written for the Gibbs free energy per unit of volume of the moving martensite plate [78].

$$\Delta G^{P\rightarrow M} = -\Delta G_{ch}^{P\rightarrow M} + \Delta G_{nch}^{P\rightarrow M} = 0 \qquad \text{Equation 6.3}$$

According to Olson and Cohen, the above thermoelastic balance equation [79] represents the local equilibrium condition at individual austenite and martensite interface, and so ,when the temperature equals M_s, $\Delta G^{P\rightarrow M} = 0$. Thus, at $T = M_s$, we can rewrite Equation 6.3 as the following:

$$\Delta G_{ch}^{P\rightarrow M} = \Delta G_{nch}^{P\rightarrow M} \qquad \text{Equation 6.4}$$

The chemical component of free energy can be approximated as follows when the undercooling is near T_o:

$$\Delta G_{ch}^{P\rightarrow M} = \Delta S_{ch}(T_0 - T) \qquad \text{Equation 6.5}$$

Substituting Equation 6.5 into Equation 6.4 with $T = M_s$ leads to the following expression:

$$\Delta S_{ch}(T_0 - M_s) = \Delta G_{nch}^{P\rightarrow M} \qquad \text{Equation 6.6}$$

The nonchemical free energy terms include elastic, friction, magnetic, and grain size effects, and it is important to note that the nonchemical free energy term is a cumulative term and continues to increase until it reaches a saturation value, which is limited by the latent heat associated with the chemical free energy term. Rearranging Equation 6.6 to solve for the undercooling *($T_0 - M_s$)* leads to the following equation:

$$(T_0 - M_s) = \frac{\Delta G_{nch}^{P \to M}}{\Delta S_{ch}} = \frac{\Delta G_{friction} + \Delta G_{elastic} + \Delta G_{grain\ size} + \Delta g_{nch}}{\Delta S_{ch}} \qquad \text{Equation 6.7}$$

The nonchemical free energy term Δg_{nch} includes additional nonchemical terms related to magnetic energy and applied stresses. In an attempt to simplify Equation 6.7, nonchemical terms associated with elastic and frictional barriers are combined into one term,$\Delta G_{f,e}$.

$$(T_0 - M_s) = \frac{\Delta G_{nch}^{P \to M}}{\Delta S_{ch}} = \frac{\frac{\gamma_{eff}}{r} + \Delta G_{f,e} + \Delta g_{nch}}{\Delta S_{ch}} \qquad \text{Equation 6.8}$$

Additionally, since $\Delta H_{ch} = T_0 \Delta S_{ch}$, Equation 6.8 may be rewritten as:

$$\frac{(T_0 - M_s)}{T_0} = \frac{\left(\frac{\gamma_{eff}}{r} + \Delta G_{f,e} + \Delta g_{nch}\right)}{\Delta H_{ch}} \qquad \text{Equation 6.9}$$

From Equation 6.9, it is obvious that the range of nonchemical free energy terms is bracketed by the following expression where $M_s = T_0$ at one end and $M_s = 0$ K at the other end.

$$0 \le \frac{\gamma_{eff}}{r} + \Delta G_{f,e} + \Delta g_{nc} \le \Delta H_{ch} \qquad \text{Equation 6.10}$$

Both limits represent ideal cases where (1) nonchemical free energy terms do not exist or, (2) the nonchemical terms consume all latent heat of transformation. The first case represents a highly ideal perfect crystal with zero hysteresis, i.e. $M_s = T_0$. The second case is more interesting for a couple of reasons, because it limits the amount of nonchemical free energy terms that can be used to reduce MT temperatures. First, we realize that the lowest observed $M_s > 0$ K. Second, once the maximum undercooling is determined for a given SMA, this value can be used to quantify one of the three nonchemical terms in Equation 6.10 provided the values of the other two are known.

Tong and Wayman, derived a similar expression to describe the effect of chemical ordering on martensite transformation temperatures [96].

$$\frac{(T_0 - T_0')}{T_0} \sim \frac{\Delta G_{nc}^{sat}}{\Delta Q} \qquad \text{Equation 6.11}$$

The ratio of the nonchemical free energy and latent heat of transformation, ΔQ, is proportional the undercooling between the equilibrium temperatures T_0 and T_0' for the unstrained and strained material, respectively.

Due to the small sample mass of thin films, it is difficult to obtain thermodynamic data from calorimetric measurements. Most of the physical properties for SMAs in this work are measured with a magnetometer to determine the characteristic martensite and austenite transformation temperatures. The following derivation utilizes two data points: one is from TEM and magnetometer measurements to determine the critical grain size and corresponding transformation temperature (r_c, M_s^c) below which no MT is observed, and the other data point corresponds to a minimum bulk grain size above which the MT remain relatively unchanged and corresponding temperature (r_{bulk}, M_s^{bulk}), which can be found in literature.

Starting with Equation 6.8, we make the following assumptions: M_s is a function of grain size radius, γ_{eff} is constant, ΔS_{chm} is constant, and the additional terms are combined into a single expression Δg_{nch}. The following equation is obtained:

$$T_0 - M_s(r) = \frac{\frac{\gamma_{eff}}{r} + \Delta g_{nch}}{\Delta S_{ch}} \qquad \text{Equation 6.12}$$

Our objective is to derive an expression for $M_s = M_s(r)$ using data from microscopy and magnetic measurements. Therefore, in order to solve for the unknown constants γ_{eff} and Δg_{nch} we take the limits for grain sizes at large grain size (r_0) and sub-micron were martensite transformations are suppressed (r_c). First, let $r = r_0$, then $M_s(r_0) = M_s^{bulk}$.

$$M_s(r_0) = M_s^{bulk} = T_0 - \frac{\frac{\gamma_{eff}}{r_0} + \Delta g_{nch}}{\Delta S_{ch}} \qquad \text{Equation 6.13}$$

Solving for Δg_{nch} leads to the following equation:

$$\Delta g_{nch} = \Delta S_{ch}(T_0 - M_s^{bulk}) - \frac{\gamma_{eff}}{r_{bulk}} \qquad \text{Equation 6.14}$$

Insert back into Equation 6.13 and solve for γ_{eff} as r goes to a critical grain size below which no MT is observed below the corresponding transformation temperature:

$$\gamma_{eff} = \Delta S_{ch}(M_s^{bulk} - M_s^{c})\left(\frac{r_{bulk} - r_c}{r_c r_{bulk}}\right) \qquad \text{Equation 6.15}$$

Substitute Equations 6.14 and 6.15 into Equation 6.12 yields an expression absent of entropy and includes four terms. Two can be found from literature, and the other two needs to be determined experimentally.

$$M_s(r) = M_S^{bulk} - (M_S^{bulk} - M_S^C)\left(\frac{r_c}{r_{bulk} - r_c}\right)\left(\frac{r_{bulk} - r}{r}\right) \qquad \text{Equation 6.16}$$

Rearrange to obtain a similar expression to Tong and Wayman:

$$\frac{M_S^{bulk} - M_S(r)}{M_S^{bulk}} = \left(1 - \frac{M_S^C}{M_S^{bulk}}\right)\left(\frac{r_c}{r_{bulk} - r_c}\right)\left(\frac{r_{bulk} - r}{r}\right) \qquad \text{Equation 6.17}$$

If we let,

$$\alpha = \left(1 - \frac{M_S^C}{M_S^{bulk}}\right)\left(\frac{r_c}{r_{bulk} - r_c}\right) \qquad \text{Equation 6.18}$$

Then, we can simplify Equation 6.17 into the following dimensionless equation, which is in essence scaled or normalized by ΔS_{chm}.

$$\frac{M_S^{bulk} - M_S(r)}{M_S^{bulk}} = \frac{\Delta M}{M_S^{bulk}} = \alpha\left(\frac{r_{bulk} - r}{r}\right) \qquad \text{Equation 6.19}$$

or equivalently

$$\frac{M_S(r)}{M_S^{bulk}} = 1 - \alpha\left(\frac{r_{bulk} - r}{r}\right) \qquad \text{Equation 6.20}$$

Table 6.1 lists bulk and submicron values of grain sizes and martensite start temperatures from literature. These value were used to determine the value of α.

Table 6.1 Martensite start temperatures for bulk and critical grain sizes observed for several alloys that exhibit a martensite transformation temperature.

Alloy	M_s^{bulk} (K)	M_s^c (K)	r_{bulk} (μm)	r_c (μm)	ΔS^{bulk} (J/m^3 K)	α	Ref
NiCoMnAl	385	200	5*	37.5×10^{-3}		3.63×10^{-3}	[31, 112]
NiTi	325	200	5*	50.0×10^{-3}	5.0×10^{5}	3.89×10^{-3}	[135]
FePd	292	192	133	1.30	2.3×10^{4}	3.38×10^{-3}	[137]
Low-alloy steel	609	565	250*	1.15		3.34×10^{-4}	[153]

Figure 6.8 plots Equation 6.19, which is used to describe the grain size dependence of undercooling normalized to the bulk martensite start temperature for several alloys that exhibit a martensitic transformation. The plot represents the amount of suppression with respect to the bulk value of the martensite start temperature. At large grain sizes, the amount of undercooling from bulk is zero. When the grain size is reduced below the

characteristic bulk value, the amount of undercooling increases until it reaches a critical grain size were the MT is not observed at lower temperatures.

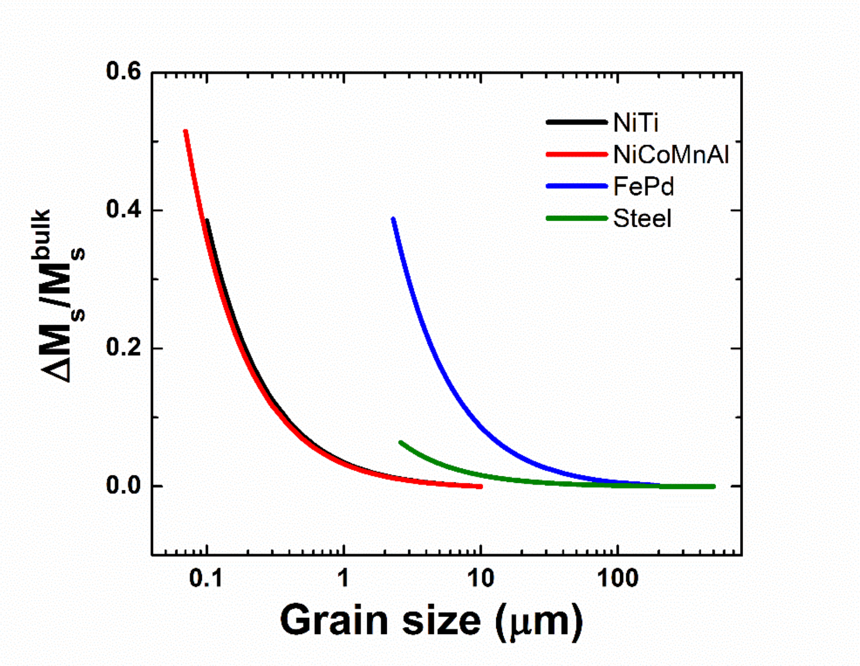

Figure 6.8 Plot of the grain size dependence of the amount of additional undercooling of reduced grain sizes with respect to the bulk martensite start temperature.

Figure 6.9 illustrates line plots of Equation 6.20, for various alloy systems that exhibit a martensitic transformation. Each line plot was constructed from two data points: $(r_c,\ M_s^c)$ and $(r_{bulk},\ M_s^{bulk})$ taken from Table 6.1. The corresponding filled squares are the additional data points found in the same reference as the two data points used to construct the line plot.

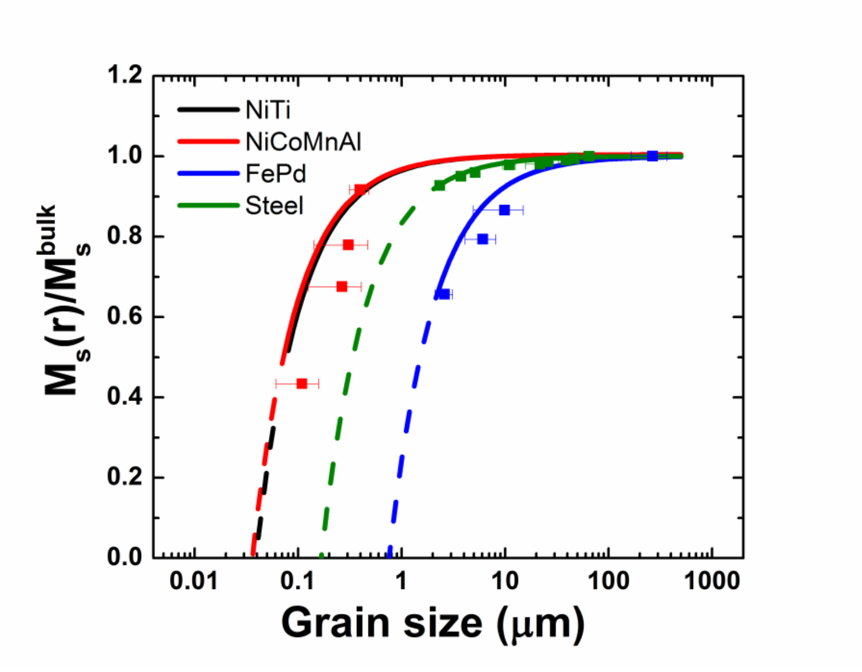

Figure 6.9 Grain size dependence of the martensite transformation temperature normalized by the bulk value.

The majority of the data points follow the plotted lines with the exception of the NiCoMnAl alloy system. This may be related to the fact that the MT temperatures were obtained from magnetic measurements using a small applied magnetic field, $H = 50$ mT. This compromises one our earlier assumptions that ΔS_{chm} is constant. Ito *et al.* showed that ΔS decreases below the Curie temperature [29]. The Curie temperature for this particular NiCoMnAl alloy composition is approximately 300 K. From Table 6.1, we determine the Curie temperature$\sim 0.8 * M_s^{bulk}$. Therefore, this explains why the data points below $0.8 * M_s^{bulk}$ fall under the curve, and why the data point above the Curie temperature is above the curve. From Equation 6.12 the amount of undercooling decreases because ΔS increases, i.e. plotting the line again with a larger ΔS would allow the data point to fall below the curve.

6.6 Summary

In summary, we have determined that the decrease in the martensite start temperature in the high temperature NiCoMnIn films was caused by the formation and growth of precipitates in the matrix. The martensite start temperature as a function of electron density is consistent with literature. Here we define the electron density as the electron concentration, *e/a*, divided by the unit volume of the parent phase. Below a critical size, decreasing grain size lowers the transformation temperature until full suppression of MT when the driving force is insufficient to overcome the energy barrier imposed by the geometrical constraints of parent phase grain size.

7. SUMMARY

First, we have synthesized $Ni_{50}Mn_{38}Co_6In_6$ films by magnetron sputtering. The as-deposited films were amorphous. Thus, we determined the effective crystallization kinetics and phase transformation temperatures in as-deposited amorphous films using differential scanning calorimeter and thermal analysis. The crystallized films show phase transformations and a reversible shape memory effect at high temperatures.

Second, magnetron co-sputtering was used to fabricate $Ni_{45}Co_7Mn_{28}Al_{20}$ films. Co-sputtering was employed to tailor film composition to similar compositions of bulk NiCoMnAl alloys reported in literature. As-deposited films had a mixture of amorphous and nanocrystalline microstructure, and thus, did not exhibit a martensite-to-austenite phase transformation. Films annealed in a differential scanning calorimeter exhibited a magnetic field induced martensitic transformation. The field-induced phase transformation temperature rate exceeds 2 K/T, implying that a large field induced variation of critical stress is likely in such a thin film system. Further experiments to tailor the chemistry of films and explore appropriate heat-treatment procedures may lead to a complete and reversible magnetic field induced phase transformation with narrow hysteresis.

Third, heat treatment of the as-deposited NiCoMnAl films with controlled annealing time results in increased grain size, which leads to ferromagnetic behavior and an increase in MT temperatures. Significant implications of this study include the use of submicron-sized grains to tailor the difference between the Curie temperature and M_s

temperature ($T_c - M_s$), which is inversely proportional to the change in entropy, to cause an increase in dT/dH. These parameters, along with composition, are essential to fabricating systems that reversibly transform in an applied magnetic field.

Fourth, we have determined the decrease in the martensite start temperature in the high temperature NiCoMnIn films was caused by the formation and growth of precipitates in the transforming matrix. The decrease in martensite start temperature as a function as a function of valence electron concentration is consistent with literature. Additionally, we presented a model that uses a thermodynamic framework to explain that below a critical value, grain size suppresses the martensitic transformation. Below a critical grain size, the martensitic transformation ceases when driving force is insufficient to overcome the energy imposed by the geometrical constraints of the parent grain size.

REFERENCES

[1] Tani J, Takagi T, Qiu J, Intelligent Material Systems: Application of Functional Materials, Applied Mechanics Reviews 1998;51:505.

[2] Claeyssen F, Lhermet N, Le Letty R, Bouchilloux P, Actuators, transducers and motors based on giant magnetostrictive materials, Journal of Alloys and Compounds 1997;258:61.

[3] Olabi A-G, Grunwald A, Design and application of magnetostrictive materials, Materials & Design 2008;29:469.

[4] Karaca HE, Karaman I, Basaran B, Lagoudas DC, Chumlyakov YI, Maier HJ, On the stress-assisted magnetic-field-induced phase transformation in Ni_2MnGa ferromagnetic shape memory alloys, Acta Materialia 2007;55:4253.

[5] Quandt E, Seemann K, Fabrication and simulation of magnetostrictive thin-film actuators, Sensors and Actuators A: Physical 1995;50:105.

[6] Grundy P, Lord D, Williams P, Magnetostriction in TbDyFe thin films, Journal of Applied Physics 1994;76:7003.

[7] Farber P, Kronmüller H, Crystallization behaviour and magnetic properties of highly magnetostrictive Fe–Tb–Dy thin films, Journal of Magnetism and Magnetic Materials 2000;214:159.

[8] Yang M, Dai J, Zhou C, Jiang D, Optical fiber magnetic field sensors with TbDyFe magnetostrictive thin films as sensing materials, Optics Express 2009;17:20777.

[9] Quandt E, Multitarget sputtering of high magnetostrictive Tb-Dy-Fe films, Journal of Applied Physics 1994;75:5653.

[10] Sandlund L, Fahlander M, Cedell T, Clark A, Restorff J, Wun-Fogle M, Magnetostriction, elastic moduli, and coupling factors of composite Terfenol-D, Journal of Applied Physics 1994;75:5656.

[11] Amirouche F, Zhou Y, Johnson T, Current micropump technologies and their biomedical applications, Microsystem Technologies 2009;15:647.

[12] Nisar A, Afzulpurkar N, Mahaisavariya B, Tuantranont A, MEMS-based micropumps in drug delivery and biomedical applications, Sensors and Actuators B: Chemical 2008;130:917.

[13] Ullakko K, Magnetically controlled shape memory alloys: A new class of actuator materials, Journal of Materials Engineering and Performance 1996;5:405.

[14] Sozinov A, Likhachev AA, Ullakko K, Magnetic and Magnetomechanical Properties of Ni-Mn-Ga Alloys with easy axis and easy plane of magnetization, Smart Structures and Materials 2001: Active Materials: Behavior and Mechanics 2001;4333:189.

[15] Soderberg O, Aaltio I, Ge Y, Heczko O, Hannula SP, Ni-Mn-Ga multifunctional compounds, Materials Science and Engineering a-Structural Materials Properties Microstructure and Processing 2008;481:80.

[16] Schlüter K, Holz B, Raatz A, Principle Design of Actuators Driven by Magnetic Shape Memory Alloys, Advanced Engineering Materials 2012;14:682.

[17] Wang F, Lu J, Xia L, Study on structure and control strategy of MSMA actuators, 2007;6423:64232I.

[18] Ullakko K, Huang JK, Kantner C, OHandley RC, Kokorin VV, Large magnetic-field-induced strains in Ni2MnGa single crystals, Applied Physics Letters 1996;69:1966.

[19] Karaman I, Karaca HE, Basaran B, Chumlyakov YJ, Maier HJ, Magnetic field and stress induced martensite reorientation in NiMnGa ferromagnetic shape memory alloy single crystals, Acta Materialia 2006;54:233.

[20] Sozinov A, Likhachev A, Lanska N, Ullakko K, Giant magnetic-field-induced strain in NiMnGa seven-layered martensitic phase, Applied Physics Letters 2002;80:1746.

[21] Kanner OY, Shilo D, Sheng J, James RD, Ganor Y, Ferromagnetic shape memory flapper for remotely actuated propulsion systems, Smart Materials and Structures 2013;22.

[22] Chmielus M, Chernenko VA, Knowlton WB, Kostorz G, Mullner P, Training, constraints, and high-cycle magneto-mechanical properties of Ni-Mn-Ga magnetic shape-memory alloys, European Physical Journal-Special Topics 2008;158:79.

[23] Lee KH, Kim YC, Choi EW, Youn SS, Nitinol alloy as a thermoseed in high frequency alternating magnetic field, PRICM 4: Forth Pacific Rim International Conference on Advanced Materials and Processing 2001;I and II:259.

[24] Lagoudas DC, Hartl DJ, Aerospace applications of shape memory alloys, Proceedings of the Institution of Mechanical Engineers, Part G: Journal of Aerospace Engineering 2007;221:535.

[25] Kainuma R, Imano Y, Ito W, Morito H, Sutou Y, Oikawa K, Fujita A, Ishida K, Okamoto S, Kitakami O, Kanomata T, Metamagnetic shape memory effect in a Heusler-type $Ni_{43}Co_7Mn_{39}Sn_{11}$ polycrystalline alloy, Applied Physics Letters 2006;88:192513.

[26] Xu XA, Ito W, Tokunaga M, Umetsu RY, Kainuma R, Ishida K, Kinetic Arrest of Martensitic Transformation in NiCoMnAl Metamagnetic Shape Memory Alloy, Materials Transactions 2010;51:1357.

[27] Xu X, Ito W, Umetsu RY, Kainuma R, Ishida K, Anomaly of critical stress in stress-induced transformation of NiCoMnIn metamagnetic shape memory alloy, Applied Physics Letters 2009;95:181905.

[28] Ito W, Ito K, Umetsu RY, Kainuma R, Koyama K, Watanabe K, Fujita A, Oikawa K, Ishida K, Kanomata T, Kinetic arrest of martensitic transformation in the NiCoMnIn metamagnetic shape memory alloy, Applied Physics Letters 2008;92:021908.

[29] Ito W, Imano Y, Kainuma R, Sutou Y, Oikawa K, Ishida K, Martensitic and magnetic transformation behaviors in Heusler-type NiMnln and NiCoMnln metamagnetic shape memory alloys, Metallurgical and Materials Transactions A 2007;38A:759.

[30] Niemann R, Heczko O, Schultz L, Fahler S, Metamagnetic transitions and magnetocaloric effect in epitaxial Ni-Co-Mn-In films, Applied Physics Letters 2010;97:222507.

[31] Kainuma R, Ito W, Umetsu RY, Oikawa K, Ishida K, Magnetic field-induced reverse transformation in B2-type NiCoMnAl shape memory alloys, Applied Physics Letters 2008;93:091906.

[32] Monroe JA, Karaman I, Basaran B, Ito W, Umetsu RY, Kainuma R, Koyama K, Chumlyakov YI, Direct measurement of large reversible magnetic-field-induced strain in Ni-Co-Mn-In metamagnetic shape memory alloys, Acta Materialia 2012;60:6883.

[33] Karaca HE, Karaman I, Basaran B, Ren Y, Chumlyakov YI, Maier HJ, Magnetic Field-induced Phase Transformation in NiMnColn Magnetic Shape-Memory Alloys-A New Actuation Mechanism with Large Work Output, Advanced Functional Materials 2009;19:983.

[34] Kainuma R, Imano Y, Ito W, Sutou Y, Morito H, Okamoto S, Kitakami O, Oikawa K, Fujita A, Kanomata T, Ishida K, Magnetic-field-induced shape recovery by reverse phase transformation, Nature 2006;439:957.

[35] Ito W, Umetsu RY, Kainuma R, Kakeshita T, Ishida K, Heat-induced and isothermal martensitic transformations from kinetically arrested parent phase in NiCoMnIn metamagnetic shape memory alloy, Scripta Materialia 2010;63:73.

[36] Li ZB, Wang JJ, Zhang YD, He KZ, Zhao XA, Zuo LA, Hofer G, Esling C, Texturation of Ni-Co-Mn-In Ribbons by Melt Spinning, Advanced Engineering Materials 2010;12:1024.

[37] Liu J, Scheerbaum N, Hinz D, Gutfleisch O, Magnetostructural transformation in Ni-Mn-In-Co ribbons, Applied Physics Letters 2008;92:162509.

[38] Liu J, Scheerbaum N, Lyubina J, Gutfleisch O, Reversibility of magnetostructural transition and associated magnetocaloric effect in Ni–Mn–In–Co, Applied Physics Letters 2008;93:102512.

[39] Liu J, Woodcock TG, Scheerbaum N, Gutfleisch O, Influence of annealing on magnetic field-induced structural transformation and magnetocaloric effect in Ni-Mn-In-Co ribbons, Acta Materialia 2009;57:4911.

[40] Miyamoto T, Nagasako M, Kainuma R, Phase equilibria in the Ni–Mn–In alloy system, Journal of Alloys and Compounds 2013;549:57.

[41] Niemann R, Schultz L, Fahler S, Growth of sputter-deposited metamagnetic epitaxial Ni-Co-Mn-In films, Journal of Applied Physics 2012;111:093909.

[42] Rios S, Karaman I, Zhang X, Crystallization and high temperature shape memory behavior of sputter-deposited NiMnCoIn thin films, Applied Physics Letters 2010;96:173102.

[43] Erkartal B, Duppel V, Niemann R, Schultz L, Fähler S, Schürmann U, Kienle L, Structure and Composition of Magnetocaloric Ni–Mn–In–Co Thin Films on the Nanoscale—A TEM Study, Advanced Engineering Materials 2012;14:710.

[44] Pérez-Landazábal JI, Recarte V, Sánchez-Alarcos V, Kustov S, Salas D, Cesari E, Effect of magnetic field on the isothermal transformation of a Ni–Mn–In–Co magnetic shape memory alloy, Intermetallics 2012;28:144.

[45] Pérez-Landazábal JI, Recarte V, Sánchez-Alarcos V, Gómez-Polo C, Cesari E, Magnetic properties of the martensitic phase in Ni-Mn-In-Co metamagnetic shape memory alloys, Applied Physics Letters 2013;102:101908.

[46] Tanaka Y, Oikawa K, Sutou Y, Omori T, Kainuma R, Ishida K, Martensitic transition and superelasticity of Co–Ni–Al ferromagnetic shape memory alloys with $\beta + \gamma$ two-phase structure, Materials Science and Engineering: A 2006;438–440:1054.

[47] Cong DY, Roth S, Schultz L, Magnetic properties and structural transformations in Ni–Co–Mn–Sn multifunctional alloys, Acta Materialia 2012;60:5335.

[48] Song Y, Bhatti KP, Srivastava V, Leighton C, James RD, Thermodynamics of energy conversion via first order phase transformation in low hysteresis magnetic materials, Energy & Environmental Science 2013;6:1315.

[49] Umetsu RY, Endo K, Kondo A, Kindo K, Ito W, Xu X, Kanomata T, Kainuma R, Magnetoresistance and Transformation Hysteresis in the $Ni_{50}Mn_{34.4}In_{15.6}$ Metamagnetic Shape Memory Alloy, Materials Transactions 2013;54:291.

[50] Srivastava V, Chen X, James RD, Hysteresis and unusual magnetic properties in the singular Heusler alloy $Ni_{45}Co_5Mn_{40}Sn_{10}$, Applied Physics Letters 2010;97:014101.

[51] Krenke T, Aksoy S, Duman E, Acet M, Moya X, Mañosa L, Planes A, Hysteresis effects in the magnetic-field-induced reverse martensitic transition in magnetic shape-memory alloys, Journal of Applied Physics 2010;108.

[52] Mitsui Y, Koyama K, Ito W, Umetsu RY, Kainuma R, Watanabe K, Observation of Reverse Transformation in Metamagnetic Shape Memory Alloy $Ni_{40}Co_{10}Mn_{34}Al_{16}$ by High-Field X-Ray Diffraction Measurements, Materials Transactions 2010;51:1648.

[53] Khovaylo V, Lyange M, Skokov K, Gutfleisch O, Chatterjee R, Xu X, Kainuma R, Adiabatic Temperature Change in Metamagnetic Ni (Co)-Mn-Al Heusler Alloys, Materials Science Forum 2013;738:446.

[54] Ito W, Basaran B, Umetsu RY, Karaman I, Kainuma R, Ishida K, Shape Memory Response in $Ni_{40}Co_{10}Mn_{33}Al_{17}$ Polycrystalline Alloy, Materials Transactions 2010;51:525.

[55] Xu X, Ito W, Kanomata T, Kainuma R, Entropy Change during Martensitic Transformation in $Ni_{50-x}Co_xMn_{50-y}Al_y$ Metamagnetic Shape Memory Alloys, Entropy 2014;16:1808.

[56] Rios S, Bufford D, Karaman I, Wang H, Zhang X, Magnetic field induced phase transformation in polycrystalline NiCoMnAl thin films, Applied Physics Letters 2013;103:132404.

[57] Yu SY, Ma L, Liu GD, Liu ZH, Chen JL, Cao ZX, Wu GH, Zhang B, Zhang XX, Magnetic field-induced martensitic transformation and large magnetoresistance in NiCoMnSb alloys, Applied Physics Letters 2007;90:242501.

[58] Nayak AK, Suresh KG, Nigam AK, Coelho AA, Gama S, Pressure induced magnetic and magnetocaloric properties in NiCoMnSb Heusler alloy, Journal of Applied Physics 2009;106:053901.

[59] Sahoo R, Raj Kumar DM, Babu DA, Suresh KG, Raja MM, In-plane and out of plane magnetic properties in Ni46Co4Mn38Sb12 ribbons, Journal of Applied Physics 2013;113:17A940.

[60] Nayak AK, Suresh KG, Nigam AK, Anomalous effects of repeated martensitic transitions on the transport, magnetic and thermal properties in Ni–Co–Mn–Sb Heusler alloy, Acta Materialia 2011;59:3304.

[61] Firstov GS, Van Humbeeck J, Koval YN, High Temperature Shape Memory Alloys Problems and Prospects, Journal of Intelligent Material Systems and Structures 2006;17:1041.

[62] Firstov G, Vanhumbeeck J, Koval Y, High-temperature shape memory alloysSome recent developments, Materials Science and Engineering A 2004;378:2.

[63] Thornton JA, Hoffman DW, Stress-Related Effects in Thin-Films, Thin Solid Films 1989;171:5.

[64] Yang Z, Tirry W, Schryvers D, Analytical TEM investigations on concentration gradients surrounding NiTi precipitates in Ni-Ti shape memory material, Scripta Materialia 2005;52:1129.

[65] Dlouhy A, Bojda O, Somsen C, Eggeler G, Conventional and in-situ transmission electron microscopy investigations into multistage martensitic transformations in Ni-rich NiTi shape memory alloys, Materials Science and Engineering: A 2008;481-482:409.

[66] Recarte V, Pérez-Landazábal JI, Kustov S, Cesari E, Entropy change linked to the magnetic field induced martensitic transformation in a Ni–Mn–In–Co shape memory alloy, Journal of Applied Physics 2010;107:053501.

[67] Bergmair B, Liu J, Huber T, Gutfleisch O, Suess D, Wireless and passive temperature indicator utilizing the large hysteresis of magnetic shape memory alloys, Applied Physics Letters 2012;101.

[68] Nakamura M, Yoshizawa S, Kutsuzawa N, Kambe S, Ishii O, Remote temperature sensor composed of an amorphous magnetic ribbon and a low Curie temperature ferrite tube, Phys. Status Solidi A 2007;204:4137.

[69] Yoo YK, Ohnishi T, Wang G, Duewer F, Xiang X-D, Chu YS, Mancini DC, Li Y-Q, O'Handley RC, Continuous mapping of structure–property relations in $Fe_{1-x}Ni_x$ metallic alloys fabricated by combinatorial synthesis, Intermetallics 2001;9:541.

[70] Takeuchi I, Famodu O, Read J, Aronova M, Chang K-S, Craciunescu C, Lofland S, Wuttig M, Wellstood F, Knauss L, Identification of novel compositions of ferromagnetic shape-memory alloys using composition spreads, Nature Materials 2003;2:180.

[71] Famodu OO, Hattrick-Simpers J, Aronova M, Chang K-S, Murakami M, Wuttig M, Okazaki T, Furuya Y, Knauss LA, Bendersky LA, Combinatorial investigation of ferromagnetic shape-memory alloys in the Ni-Mn-Al ternary system using a composition spread technique, Materials Transactions 2004;45:173.

[72] Zarnetta R, Savan A, Thienhaus S, Ludwig A, Combinatorial study of phase transformation characteristics of a Ti–Ni–Pd shape memory thin film composition spread in view of microactuator applications, Applied Surface Science 2007;254:743.

[73] Löbel R, Thienhaus S, Savan A, Ludwig A, Combinatorial fabrication and high-throughput characterization of a Ti–Ni–Cu shape memory thin film composition spread, Materials Science and Engineering: A 2008;481:151.

[74] Zarnetta R, Takahashi R, Young ML, Savan A, Furuya Y, Thienhaus S, Maaß B, Rahim M, Frenzel J, Brunken H, Identification of Quaternary Shape Memory Alloys with Near-Zero Thermal Hysteresis and Unprecedented Functional Stability, Advanced Functional Materials 2010;20:1917.

[75] Cui J, Chu YS, Famodu OO, Furuya Y, Hattrick-Simpers J, James RD, Ludwig A, Thienhaus S, Wuttig M, Zhang Z, Combinatorial search of thermoelastic shape-memory alloys with extremely small hysteresis width, Nature Mater. 2006;5:286.

[76] Porter DA, Easterling KE. Phase Transformations in Metals and Alloys, (Revised Reprint): CRC press, 1992.

[77] Fischer FD, Sciences ICfM. Mechanics of Solids with Phase Changes: Springer, 1997.

[78] Ortin J, Planes A, Thermodynamics of thermoelastic martensitic transformations, Acta Metallurgica 1989;37:1433.

[79] Olson G, Cohen M, Thermoelastic behavior in martensitic transformations, Scripta Metallurgica 1975;9:1247.

[80] Olson G, Cohen M, Reply to “On the equilibrium temperature in thermoelastic martensitic transformations”, Scripta Metallurgica 1977;11:345.

[81] Pecharsky VK, Gschneidner KA, Some common misconceptions concerning magnetic refrigerant materials, Journal of Applied Physics 2001;90:4614.

[82] Khovailo VV, Oikawa K, Abe T, Takagi T, Entropy change at the martensitic transformation in ferromagnetic shape memory alloys $Ni_{2+x}Mn_{1-x}Ga$, Journal of Applied Physics 2003;93:8483.

[83] Aksoy S, Krenke T, Acet M, Wassermann EF, Moya X, Mañosa L, Planes A, Tailoring magnetic and magnetocaloric properties of martensitic transitions in ferromagnetic Heusler alloys, Applied Physics Letters 2007;91:241916.

[84] Krenke T, Moya X, Aksoy S, Acet M, Entel P, Mañosa L, Planes A, Elerman Y, Yücel A, Wassermann EF, Electronic aspects of the martensitic transition in Ni–Mn based Heusler alloys, Journal of Magnetism and Magnetic Materials 2007;310:2788.

[85] Antoni P, Lluís M, Mehmet A, Magnetocaloric effect and its relation to shape-memory properties in ferromagnetic Heusler alloys, Journal of Physics: Condensed Matter 2009;21:233201.

[86] Webster PJ, Magnetic and chemical order in Heusler alloys containing cobalt and manganese, Journal of Physics and Chemistry of Solids 1971;32:1221.

[87] Graf T, Felser C, Parkin SSP, Simple rules for the understanding of Heusler compounds, Progress in Solid State Chemistry 2011;39:1.

[88] Picozzi S, Continenza A, Freeman AJ, Co_2MnX (X = Si, Ge, Sn) Heusler compounds:An ab initio study of their structural, electronic, and magnetic properties at zero and elevated pressure, Physical Review B 2002;66:094421.

[89] Şaşıoğlu E, Sandratskii LM, Bruno P, Role of conduction electrons in mediating exchange interactions in Mn-based Heusler alloys, Physical Review B 2008;77:064417.

[90] Recarte V, Pérez-Landazábal JI, Sánchez-Alarcos V, Rodríguez-Velamazán JA, Dependence of the martensitic transformation and magnetic transition on the atomic order in Ni–Mn–In metamagnetic shape memory alloys, Acta Materialia 2012;60:1937.

[91] Pathak AK, Dubenko I, Pueblo C, Basnyat P, Stadler S, Ali N, The Effect of Partial Substitution of Ni by Co on the Magnetic and Electrical Properties of $Ni_{50}Mn_{35}In_{15}$ Heusler Alloy, Magnetics, IEEE Transactions on 2010;46:1444.

[92] Recarte V, Pérez-Landazábal JI, Sánchez-Alarcos V, Dependence of the relative stability between austenite and martensite phases on the atomic order in a Ni–Mn–In Metamagnetic Shape Memory Alloy, Journal of Alloys and Compounds 2012;536, Supplement 1:S308.

[93] Wang RL, Xu LS, Xiao HB, Xu LF, Zhang JX, Chen RJ, Guo S, Yang CP, Effect of post-annealing on the phase transitions and magnetocaloric properties in bulk $Ni_{44}Mn_{45}Sn_{11}$ alloy, Journal of Applied Physics 2013;113:17A936.

[94] Seguí C, Cesari E, Effect of ageing on the structural and magnetic transformations and the related entropy change in a Ni–Co–Mn–Ga ferromagnetic shape memory alloy, Intermetallics 2011;19:721.

[95] Ito W, Nagasako M, Umetsu RY, Kainuma R, Kanomata T, Ishida K, Atomic ordering and magnetic properties in the $Ni_{45}Co_5Mn_{36.7}In_{13.3}$ metamagnetic shape memory alloy, Applied Physics Letters 2008;93:232503.

[96] Tong H, Wayman C, Thermodynamics of thermoelastic martensitic transformations, Acta Metallurgica 1975;23:209.

[97] Kockar B, Karaman I, Kim JI, Chumlyakov Y, A method to enhance cyclic reversibility of NiTiHf high temperature shape memory alloys, Scripta Materialia 2006;54:2203.

[98] Karaca HE, Saghaian SM, Ded G, Tobe H, Basaran B, Maier HJ, Noebe RD, Chumlyakov YI, Effects of nanoprecipitation on the shape memory and material properties of an Ni-rich NiTiHf high temperature shape memory alloy, Acta Materialia 2013;61:7422.

[99] Karaca HE, Karaman I, Brewer A, Basaran B, Chumlyakov YI, Maier HJ, Shape memory and pseudoelasticity response of NiMnCoIn magnetic shape memory alloy single crystals, Scripta Materialia 2008;58:815.

[100] Zarinejad M, Liu Y, Tong Y, Transformation temperature changes due to second phase precipitation in NiTi-based shape memory alloys, Intermetallics 2009;17:914.

[101] Patel J, Cohen M, Criterion for the action of applied stress in the martensitic transformation, Acta Metallurgica 1953;1:531.

[102] Doyle S, Chernenko VA, Besseghini S, Gambardella A, Kohl M, Müllner P, Ohtsuka M, Residual stress in Ni-Mn-Ga thin films deposited on different substrates, The European Physical Journal Special Topics 2008;158:99.

[103] Nix WD, Mechanical properties of thin films, Metallurgical Transactions A 1989;20:2217.

[104] Salzbrenner R, Cohen M, On the thermodynamics of thermoelastic martensitic transformations, Acta Metallurgica 1979;27:739.

[105] Freund LB, Suresh S. Thin film materials: stress, defect formation and surface evolution: Cambridge University Press, 2003.

[106] Xu X, Ito W, Katakura I, Tokunaga M, Kainuma R, In situ optical microscopic observation of NiCoMnIn metamagnetic shape memory alloy under pulsed high magnetic field, Scripta Materialia 2011;65:946.

[107] Krenke T, Acet M, Wassermann EF, Moya X, Mañosa L, Planes A, Ferromagnetism in the austenitic and martensitic states of Ni-Mn-In alloys, Physical Review B 2006;73:174413.

[108] Canadinc D, Dadda J, Maier HJ, Karaman I, Karaca HE, Chumlyakov YI, On the role of the cooling rate and crystallographic orientation on the shape memory properties

of CoNiAl single crystals under compression, Smart Materials and Structures 2007;16:1006.

[109] Liu J, Scheerbaum N, Hinz D, Gutfleisch O, Martensitic transformation and magnetic properties in Ni–Fe–Ga–Co magnetic shape memory alloys, Acta Materialia 2008;56:3177.

[110] Atli KC, Karaman I, Noebe RD, Garg A, Chumlyakov YI, Kireeva IV, Improvement in the Shape Memory Response of $Ti_{50.5}Ni_{24.5}Pd_{25}$ High-Temperature Shape Memory Alloy with Scandium Microalloying, Metallurgical and Materials Transactions A 2010;41:2485.

[111] Liu J, Scheerbaum N, Gutfleisch O, Magnetic-Field-Induced Reverse Martensitic Transformation in Ni-Mn-In-Co Ribbons, Actuator 08, Conference Proceedings 2008:721.

[112] Kainuma R, Ishida K, Nakano H, Martensitic transformations in NiMnAl β phase alloys, Metallurgical and Materials Transactions A 1996;27:4153.

[113] Sutou Y, Ohnuma I, Kainuma R, Ishida K, Ordering and martensitic transformations of Ni_2AlMn heusler alloys, Metallurgical and Materials Transactions A 1998;29:2225.

[114] Reading, Reading M, Hourston DJ. Modulated Temperature Differential Scanning Calorimetry: Theoretical and Practical Applications in Polymer Characterisation. Hot Topics in Thermal Analysis and Calorimetry, Volume 6, 2006.

[115] Cooper A, Nutley MA, Wadood A, Differential scanning microcalorimetry, Protein-ligand interactions: Hydrodynamics and calorimetry 2000:287.

[116] Danley RL, Caulfield P.A. DSC Baseline Improvements Obtained by a New Heat Flow Measurement Technique. In: Instruments T, editor. New Castle, DE, n.d.

[117] PPMS Vibrating Sample Magnetometer Note In: Design Q, editor. San Diego, CA, 2009.

[118] Jeong S, Inoue K, Inoue S, Koterazawa K, Taya M, Inoue K, Effect of magnetic field on martensite transformation in a polycrystalline Ni2MnGa, Materials Science and Engineering: A 2003;359:253.

[119] Karaman I, Karaca H, Basaran B, Lagoudas D, Chumlyakov Y, Maier H, Stress-assisted reversible magnetic field-induced phase transformation in Ni_2MnGa magnetic shape memory alloys, Scripta Materialia 2006;55:403.

[120] Otsuka K, Ren X, Recent developments in the research of shape memory alloys, Intermetallics 1999;7:511.

[121] Dadda J, Maier H, Karaman I, Karaca H, Chumlyakov Y, Pseudoelasticity at elevated temperatures in [001] oriented $Co_{49}Ni_{21}Ga_{30}$ single crystals under compression, Scripta Materialia 2006;55:663.

[122] Lee H-J, Ramirez AG, Crystallization and phase transformations in amorphous NiTi thin films for microelectromechanical systems, Applied Physics Letters 2004;85:1146.

[123] Rumpf H, Craciunescu C, Modrow H, Olimov K, Quandt E, Wuttig M, Successive occurrence of ferromagnetic and shape memory properties during crystallization of NiMnGa freestanding films, Journal of Magnetism and Magnetic Materials 2006;302:421.

[124] Seeger C, Ryder P, Kinetics of the crystallization of amorphous Ti-Ni and Ti-Ni-Si alloys, Materials Science and Engineering: A 1994;179:641.

[125] Wu S, Tseng K, Wang J, Crystallization behavior of rf-sputtered near stoichiometric Ni_2MnGa thin films, Thin Solid Films 2002;408:316.

[126] Chen J, Wu S, Crystallization temperature and activation energy of rf-sputtered near-equiatomic TiNi and $Ti_{50}Ni_{40}Cu_{10}$ thin films, Journal of Non-Crystalline Solids 2001;288:159.

[127] Wuttig M, Craciunescu C, Li J, Phase transformations in ferromagnetic NiMnGa shape memory films, Materials Transactions Jim 2000;41:933.

[128] Rumpf H, Craciunescu C, Feydt J, Gilles A, Wuttig M, Quandt E, Fabrication and characterization of freestanding NiMnGa films, Materials and Devices for Smart Systems 2004;785:195.

[129] Rumpf H, Feydt J, Lewandowski D, Ludwig A, Winzek B, Quandt E, Zhao P, Wuttig M, Shape memory effect and magnetostriction of sputtered NiMnGa thin films, Smart Structures and Materials 2003: Active Materials: Behavior and Mechanics 2003;5053:191.

[130] Mahnke GJ, Seibt M, Mayr SG, Microstructure and twinning in epitaxial NiMnGa films, Physical Review B 2008;78:012101.

[131] Zhang Y, Hughes RA, Britten JF, Gong W, Preston JS, Botton GA, Niewczas M, Epitaxial Ni-Mn-Ga films derived through high temperature in situ depositions, Smart Materials & Structures 2009;18:025019.

[132] Kainuma R, Oikawa K, Ito W, Sutou Y, Kanomata T, Ishida K, Metamagnetic shape memory effect in NiMn-based Heusler-type alloys, Journal of Materials Chemistry 2008;18:1837.

[133] Kustov S, Corró ML, Pons J, Cesari E, Entropy change and effect of magnetic field on martensitic transformation in a metamagnetic Ni–Co–Mn–In shape memory alloy, Applied Physics Letters 2009;94:191901.

[134] Ito K, Ito W, Umetsu RY, Tajima S, Kawaura H, Kainuma R, Ishida K, Metamagnetic shape memory effect in polycrystalline NiCoMnSn alloy fabricated by spark plasma sintering, Scripta Materialia 2009;61:504.

[135] Waitz T, Antretter T, Fischer FD, Simha NK, Karnthaler HP, Size effects on the martensitic phase transformation of NiTi nanograins, Journal of the Mechanics and Physics of Solids 2007;55:419.

[136] Ozdemir N, Karaman I, Mara NA, Chumlyakov YI, Karaca HE, Size effects in the superelastic response of $Ni_{54}Fe_{19}Ga_{27}$ shape memory alloy pillars with a two stage martensitic transformation, Acta Materialia 2012;60:5670.

[137] Seki K, Kura H, Sato T, Taniyama T, Size dependence of martensite transformation temperature in ferromagnetic shape memory alloy FePd, Journal of Applied Physics 2008;103:063910.

[138] Dunand DC, Mullner P, Size Effects on Magnetic Actuation in Ni-Mn-Ga Shape-Memory Alloys, Advanced Materials 2011;23:216.

[139] Liu Y, Karaman I, Wang H, Zhang X, Two Types of Martensitic Phase Transformations in Magnetic Shape Memory Alloys by In-Situ Nanoindentation Studies, Advanced Materials 2014;26:3893.

[140] Fu YQ, Zhang S, Wu MJ, Huang WM, Du HJ, Luo JK, Flewitt AJ, Milne WI, On the lower thickness boundary of sputtered TiNi films for shape memory application, Thin Solid Films 2006;515:80.

[141] Jetta N, Ozdemir N, Rios S, Bufford D, Karaman I, Zhang X, Phase transformations in sputtered Ni–Mn–Ga magnetic shape memory alloy thin films, Thin Solid Films 2012;520:3433.

[142] Miyamoto T, Ito W, Umetsu RY, Kanomata T, Ishida K, Kainuma R, Influence of Annealing Conditions on Magnetic Properties of $Ni_{50}Mn_{50-x}In_x$ Heusler-Type Alloys, Materials Transactions 2011;52:1836.

[143] Chikazumi S. Physics of Ferromagnetism 2e: Oxford University Press, 2009.

[144] Susan D, Researchers Create New 'Memory' Metals That Could Improve Safety, All Things Considered 2014.

[145] Duerig T, Pelton A, Trepanier C, PART I Mechanisms and Behavior, 2011.

[146] Enami K, Nenno S, Shimizu K, Crystal structure and internal twins of the Ni-36.8 at% Al martensite, Trans. Jpn. Inst. Met 1973;14:161.

[147] Rusović N, Warlimont H, The elastic behaviour of β2-NiAl alloys, Physica status solidi (a) 1977;44:609.

[148] Adachi K, Wayman C, Transformation behavior of nearly stoichiometric Ni-Mn alloys, Metallurgical Transactions A 1985;16:1567.

[149] Adachi K, Wayman CM, Electron microscopic study ofθ-phase martensite in Ni-Mn alloys, Metallurgical Transactions A 1985;16:1581.

[150] Van Humbeeck J, High Temperature Shape Memory Alloys, Journal of Engineering Materials and Technology 1999;121:98.

[151] Wang RL, Yan JB, Xiao HB, Xu LS, Marchenkov VV, Xu LF, Yang CP, Effect of electron density on the martensitic transition in Ni–Mn–Sn alloys, Journal of Alloys and Compounds 2011;509:6834.

[152] Zarinejad M, Liu Y, Dependence of Transformation Temperatures of NiTi-based Shape-Memory Alloys on the Number and Concentration of Valence Electrons, Advanced Functional Materials 2008;18:2789.

[153] Yang H-S, Bhadeshia H, Austenite grain size and the martensite-start temperature, Scripta Materialia 2009;60:493.